

THE WAVE NORMAL AND POYNTING FLUX OF
MAGNETOSPHERIC PLASMA WAVES

by

Michael Joseph LeDocq

An Abstract

Of a thesis submitted in partial fulfillment
of the requirements for the Doctor of
Philosophy degree in Physics
in the Graduate College of
The University of Iowa

July 1998

Thesis supervisor: Professor Donald A. Gurnett

ABSTRACT

Wave normal and Poynting vector measurements from the Plasma Wave Instrument on the Polar spacecraft are used to locate the source region of magnetospheric whistler mode chorus and to confirm the quasi-electrostatic theory for the propagation of auroral hiss. The wave normal vector, which determines the direction of wave propagation, is calculated from the imaginary part of the wave magnetic field cross-spectral matrix, and the Poynting vector, which determines the direction of energy flow of a wave, is calculated directly using electric and magnetic field waveform measurements. Almost without exception, chorus is observed to propagate away from the magnetic equator, indicating that the source of these emissions is very close to the magnetic equator. No evidence of chorus reflected from the ionosphere or high-altitude magnetosphere has been observed. The absence of a reflected component indicates that chorus is absorbed, probably by Landau damping, before the wave can return to the magnetic equator. Generation mechanisms that require multiple passes through the source region cannot explain chorus generation. Auroral hiss usually has an extremely weak, and often non-detectable, magnetic component. When the magnetic component is detectable, auroral hiss is found to be propagating with wave normal angles near the resonance cone. The Poynting vector for this quasi-electrostatic mode of

propagation is at a large angle to the wave normal, in good agreement with theory. Measured magnetic to electric field ratios also agree well with the magnetic to electric field ratios calculated from the measured wave normal angle using whistler mode theory. These comparisons show that the auroral hiss propagates in a mode that has wave normal angles very close to the resonance cone.

Abstract approved: David A. Smith
Thesis supervisor
Prof., Physics and Astronomy
Title and department
July 21, 1998
Date

WAVE NORMAL AND POYNTING FLUX DIRECTIONS OF
MAGNETOSPHERIC PLASMA WAVES

by

Michael Joseph LeDocq

A thesis submitted in partial fulfillment
of the requirements for the Doctor of
Philosophy degree in Physics
in the Graduate College of
The University of Iowa

July 1998

Thesis supervisor: Professor Donald A. Gurnett

Graduate College
The University of Iowa
Iowa City, Iowa

CERTIFICATE OF APPROVAL

PH.D. THESIS

This is to certify that the Ph.D. thesis of

Michael Joseph LeDocq

has been approved by the Examining Committee
for the thesis requirement for the Doctor of
Philosophy degree in Physics at the July 1998
graduation.

Thesis committee

Doel A. Humelt
Thesis supervisor

P. Barry Butler
Member

Steven N. Spangler
Member

Jim Buty
Member

Craig Kelly
Member

To
Valentine and Catherina Borgra,
loving and devoted grandparents

ACKNOWLEDGMENTS

Completion of an endeavor as large as this dissertation has been possible only through the help and support of many people. I would first like to thank my advisor, Professor Donald Gurnett who first envisioned this study and has guided its development. His insight into the physics behind this analysis provided a more complete understanding of the method and its interpretation. Secondly, I would like to thank Kathy Kurth who spent many long hours helping to type and format this thesis, and generally kept things running smoothly. Her help has been of inestimable value. I would also like to thank Jolene Pickett, the Polar PWI Science Data Manager, Ann Persoon, the Polar PWI Operations Manager, and George Hospodarsky who built the PWI search coil magnetometer. Their knowledge of the Polar Plasma Wave Instrument, other Polar studies and investigators, and their help in calibrating and searching through the data were extremely helpful. They have also been wonderful traveling companions to various meetings. I am also grateful to Doug Menietti. Our discussions of plasma physics always provided insight, and his spiritual support was always greatly appreciated.

I would also like to extend special thanks to several other UI staff members. The plasma wave group programmers provided vital programming and data processing assistance. I am most indebted to Julie Dowell who developed many data

processing and graphics programs, and spent much time helping to debug software. My thanks also go to Joyce Chrisinger who drafted several of the illustrations, and to Jean Hospodarsky who has kindly assisted with many miscellaneous tasks.

Many discussions about direction finding methods and VLF wave propagation were provided by Umran Inan and Dave Lauben of Stanford University. Owen Storey of Cucuron, France also spent many hours sharing his vast knowledge of direction finding methods with me. All of these correspondences were greatly appreciated.

My family and friends have been incredibly supportive during my many years as a graduate student. My fellow graduate students David Dunn, Stacy Palen, and Paul Foth were always willing to share experiences, and helped me to retain my perspective. My friends at the Newman Catholic Student Center, especially the Bobs, provided unwavering emotional and spiritual support. My family has always had incredible confidence in my abilities. My grandmother, Catherina Borgra, my parents, Mary and Wilford LeDocq, my brother and sister-in-law, Greg and Pam Bump, and my sister and brother-in-law Cherie and Greg Fields have provided constant support and encouragement. Most importantly, I thank my wife Becky. Her patience and caring during my many long weeks of absence are precious beyond words and have been the greatest help in bringing this work to fruition.

This research was supported by NASA through contract NAS5-30371 from Goddard Space Flight Center and funds from the University of Iowa Graduate College.

ABSTRACT

Wave normal and Poynting vector measurements from the Plasma Wave Instrument on the Polar spacecraft are used to locate the source region of magnetospheric whistler mode chorus and to confirm the quasi-electrostatic theory for the propagation of auroral hiss. The wave normal vector, which determines the direction of wave propagation, is calculated from the imaginary part of the wave magnetic field cross-spectral matrix, and the Poynting vector, which determines the direction of energy flow of a wave, is calculated directly using electric and magnetic field waveform measurements. Almost without exception, chorus is observed to propagate away from the magnetic equator, indicating that the source of these emissions is very close to the magnetic equator. No evidence of chorus reflected from the ionosphere or high-altitude magnetosphere has been observed. The absence of a reflected component indicates that chorus is absorbed, probably by Landau damping, before the wave can return to the magnetic equator. Generation mechanisms that require multiple passes through the source region cannot explain chorus generation. Auroral hiss usually has an extremely weak, and often non-detectable, magnetic component. When the magnetic component is detectable, auroral hiss is found to be propagating with wave normal angles near the resonance cone. The Poynting vector for this quasi-electrostatic mode of propagation is at a

large angle to the wave normal, in good agreement with theory. Measured magnetic to electric field ratios also agree well with the magnetic to electric field ratios calculated from the measured wave normal angle using whistler mode theory. These comparisons show that the auroral hiss propagates in a mode that has wave normal angles very close to the resonance cone.

TABLE OF CONTENTS

	Page
LIST OF TABLES	x
LIST OF FIGURES	xi
 CHAPTER	
I. INTRODUCTION	1
1.1 Scientific Studies	2
1.2 Technical Contributions	3
1.3 Thesis Organization	5
II. POLAR PLASMA WAVE INSTRUMENT AND DATA PROCESSING	8
2.1 Polar Spacecraft and Plasma Wave Instrument	8
2.2 Data Preparation	11
2.3 Sensor Calibrations	13
2.3.1 Search Coil Calibrations	14
2.3.2 Electric Antenna Calibrations	15
III. THE WHISTLER-MODE AND WAVE NORMAL ANALYSIS METHODS	17
3.1 Whistler-Mode Dispersion Relation	17
3.2 Wave Normal Vector Determination	25
3.2.1 Minimum Variance Method	27
3.2.2 Means' Method	29
3.2.3 Eigenvector Method	30
3.2.4 Wave Distribution Function Method	31
3.2.5 Maximum Likelihood Method	34
3.2.6 Spin Modulation Method	34
3.2.7 Amplitude Method	35
3.3 Poynting Vector Determination	36

IV.	WAVE NORMAL AND POYNTING VECTOR CALCULATION	39
4.1	Wave Normal Calculation (Means' Method)	39
4.2	Eigenvalue Ratio Test for Planar Waves	43
4.3	Poynting Vector Calculation	45
V.	VECTOR DIRECTION VERIFICATION AND ERROR ANALYSIS	49
5.1	Spectral Analysis	49
5.2	Confidence Limits of the Power Spectra	51
5.3	Prelaunch Search Coil Calibration and k-Vector Tests	54
5.3.1	UV-Sine and UV-Square Tests	55
5.3.2	Z-Sine and Z-Square Tests	56
5.4	Verification of Poynting Vector Direction Using Prelaunch Test Data	58
5.5	Inflight Verification of Propagation Directions	60
5.5.1	Whistlers	61
5.5.2	Omega Signals	64
5.5.3	Comparison with Ray Tracing Results	67
5.6	Estimation of Errors	69
5.6.1	Random Error	69
5.6.2	Systematic Error	72
VI.	MAGNETOSPHERIC CHORUS SOURCE REGION	76
6.1	Previous Studies of Chorus Wave Normal Angle	76
6.2	Poynting Vector Direction of Magnetospheric Chorus	81
6.3	Discussion of Chorus Propagation Characteristics	85
VII.	AURORAL HISS PROPAGATION CHARACTERISTICS	88
VIII.	CONCLUSIONS	101
APPENDIX		
A.	COORDINATE SYSTEMS	160
B.	CALIBRATION TABLES	163
C.	VECTOR DIRECTION VERIFICATION AND ERROR ANALYSIS TABLES	165

REFERENCES	169
----------------------	-----

LIST OF TABLES

		Page
1.	Search Coil Phase Shifts	164
2.	Electric Sensor Gains	165
3.	Electric Sensor Phase Shifts	165
4.	Comparison of Wave Normal Angles Using GSFC Magsite Test Data	167
5.	Geographic Position of Polar Magnetic Field Endpoint	167
6.	Cloud-to-Ground Lightning Observed by National Lightning Detection Network	167
7.	Analysis Results Using Computer-Generated Data With Random Noise	168
8.	Test Results Using Computer-Generated Signals With Gain and Phase Adjustments	168
9.	Simulation of Calibration Effects at 1 kHz and 8 kHz	168

LIST OF FIGURES

		Page
1.	The major regions of Earth's magnetosphere with a representative Polar orbit.	104
2.	A sketch of the Polar spacecraft showing PWI sensor locations and orientations.	106
3.	Top view of the Polar spacecraft showing PWI sensor orientations.	108
4.	A spectrogram of PWI/HFWR 6-channel mode data on September 11, 1996, from 09:11:56 UT to 09:12:42 UT. The spacecraft is at $L = 2.6$, $R = 2.6 R_E$, $MLT = 02.42$, $\lambda_m = 2.1^\circ$	110
5.	Whistler-mode index of refraction curve for frequencies greater than the lower hybrid frequency and less than the electron cyclotron frequency. The index of refraction vector is parallel to the wave vector. The wave normal angle is θ . The angle between the Poynting vector \vec{S} and \vec{B}_0 is θ_s	112
6.	Diagram showing the local geomagnetic field-aligned coordinate system. (a) The orientation of the wave normal vector in the local geomagnetic field-aligned coordinate system. (b) The orientation of the Poynting vector in the same coordinate system.	114
7.	Electric power spectrum, magnetic power spectrum, wave normal angle, azimuthal angle of the wave normal vector, coherence, and polarization of emissions from 09:11:56 UT to 09:12:42 UT on September 11, 1996.	116
8.	Poynting flux, polar angle of Poynting vector, azimuthal angle of Poynting vector, eigenvalue ratio of spectral matrix, coherence, and direction of S_z for emissions from 09:11:56 UT to 09:12:42 UT on September 11, 1996.	118

9.	Wave normal vector orientation angles for the 13.1 kHz Omega signal at 09:12:42.492 UT to 09:12:42.942 UT. The top panel contains wave normal angle. The bottom panel contains azimuth angle of the wave normal vector.	120
10.	Poynting vector orientation angles for the 13.1 kHz Omega signal at 09:12:42.492 UT to 09:12:42.942 UT. The top panel contains the polar angle of the Poynting vector. The bottom panel contains the azimuth angle of the Poynting vector.	122
11.	Cross-power spectral density at 09:12:42.224 UT on September 11, 1996.	124
12.	Sketch of GSFC Magnetic Field Test Facility PWI search coil tests for waves propagating in the search coil U-V plane. (a) Top view. (b) Side view.	126
13.	Sketch of GSFC Magnetic Field Test Facility PWI search coil tests for waves with wave normal parallel to Z search coil. (a) Top view. (b) Side view.	128
14.	Path of the endpoint of the geomagnetic field that intersects the Polar orbit from 09:00 UT to 09:15 UT on September 11, 1996.	130
15.	Location of cloud-to-ground lightning flashes observed in the United States by the U.S. National Lightning Detection Network from 09:00 UT to 09:15 UT on September 11, 1996.	132
16.	Ray path of a 15.5-kHz signal launched from 45° magnetic latitude. The wave normal angle increases as the wave propagates. Dipole magnetic field lines are shown as dashed lines.	134
17.	Diagram of the suggested chorus generation region at the magnetic equator.	136
18.	Electric power spectrum, magnetic power spectrum, wave normal angle, azimuthal angle of the wave normal vector, coherence, and polarization of chorus from 00:23:07 UT to 00:23:53 UT on November 25, 1996.	138

19.	Poynting flux, polar angle of Poynting vector, azimuthal angle of Poynting vector, eigenvalue ratio of spectral matrix, coherence, and direction of S_z for chorus from 00:23:07 UT to 00:23:53 UT on November 25, 1996.	140
20.	Spectrograms of chorus observed both north and south of the geomagnetic equator on December 14, 1996. The top panel is from the Sweep Frequency Receiver (SFR). Note the logarithmic frequency scale. The bottom panel is from the High Frequency Waveform Receiver (HFWR). and shows the sign of $S_z = \bar{S} \cdot \hat{B}_0$	142
21.	A magnetic meridian plane plot showing the direction of propagation of chorus with respect to the magnetic field. Events with $\bar{S} \cdot \hat{B}_0 \geq 0$ (red) are propagating northward, and events with $\bar{S} \cdot \hat{B}_0 \leq 0$ (green) are propagating southward. As can be seen, chorus essentially always propagating away from the magnetic equator, which means that the source is located very close to the magnetic equator.	144
22.	Index of refraction surfaces and geometric representation of ray paths that are characteristic of quasi-electrostatic auroral hiss. Observations of the radiation along the satellite path produces a funnel-shaped spectrum on a frequency-time spectrogram.	146
23.	Spectrogram of auroral hiss funnel from the Polar SFR on February 28, 1997 from 09:00 UT to 11:00 UT. The top panel is the electric power spectral density and the bottom panel is the magnetic power spectral density. An auroral hiss funnel is seen in the top panel from 09:25 UT to 10:10 UT. Electromagnetic bursts are seen in the bottom panel at 09:33 UT and 09:59 UT.	148
24.	Electric power spectrum, magnetic power spectrum, wave normal angle, azimuthal angle of the wave normal vector, coherence, and polarization of auroral hiss electromagnetic burst from 09:33:25 UT to 09:34:12 UT on February 28, 1997.	150

25.	Poynting flux, polar angle of Poynting vector, azimuthal angle of Poynting vector, eigenvalue ratio of spectral matrix, coherence, and direction of S_z for auroral hiss electromagnetic burst from 09:33:25 UT to 09:34:12 UT on February 28, 1997. . . .	152
26.	Wave normal angle as a function of frequency for the auroral hiss observed from 09:33:34.2 UT to 09:33:34.65 UT on February 28, 1997.	154
27.	Poynting vector angle as a function of frequency for the auroral hiss observed from 09:33:34.2 UT to 09:33:34.65 UT on February 28, 1997.	156
28.	Ratio of magnetic field intensity to electric field intensity as a function of frequency for auroral hiss observed from 09:33:34.2 UT to 09:33:34.65 UT on February 28, 1997. $c B / E $ calculated using observed wave normal angles are plotted as filled circles. $c B / E $ calculated from measured electric and magnetic fields are plotted as open circles. The second set is plotted at slightly shifted frequencies for clarity.	158

CHAPTER I. INTRODUCTION

The objective of this thesis is to study the wave normal and Poynting vectors of two magnetospheric whistler-mode plasma waves, chorus and auroral hiss. The wave normal vector determines the direction of propagation of a wave, and is also important for determining the polarization, the mode, and the source region of the wave. It can also be used to calculate the dispersion relation, to determine Landau and cyclotron resonances, to estimate the local plasma index of refraction, and to examine wave-particle interactions. The Poynting flux determines the direction of propagation of wave energy and can also be used to identify wave mode and study the wave generation region.

The wave normal and Poynting vectors examined in this thesis are obtained from three-axis electric and magnetic waveforms measured by the Polar Plasma Wave Instrument. Wave normal and Poynting vector orientations are displayed as frequency-time spectrograms, thereby expanding previous studies that have generally been limited to a single frequency channel or to isolated time periods. These spectrograms are then used to survey large data sets for identification of coherent emissions, and to perform detailed studies of their propagation characteristics. The present study incorporates technical improvements over previous wave normal investigations and produces direct calculations of Poynting flux. Both are used to

further the understanding of magnetospheric very-low-frequency (VLF) chorus and auroral hiss.

1.1 Scientific Studies

The first and primary use of the Polar wave normal and Poynting vector measurements is to definitively identify the generation region of VLF chorus. Chorus is one of the most common and intense whistler-mode emissions observed in the Earth's magnetosphere. It is characterized by fine structure such as rising tones, falling tones, and impulsive bursts. The Poynting flux directions of a large number of VLF chorus events observed by the Polar spacecraft are used to locate the source region within a few degrees of the geomagnetic equator. No evidence of a reflected component is observed. This indicates that generation mechanisms requiring multiple passes of the wave through the source region are not applicable. The details of this study are contained in Chapter 6.

The second use of the Polar wave normal and Poynting vector measurements is to verify the theoretical frequency trends of the wave normal and the Poynting vector directions of quasi-electrostatic auroral hiss. Auroral hiss is a broadband whistler-mode emission often observed in the Earth's auroral regions. Downward propagating auroral hiss has been observed by many low altitude satellites. Upward propagating auroral hiss is observed mainly by high altitude satellites including Polar. Upward propagating auroral hiss has a funnel shape on frequency-time spectrograms when observed from above the source location. The wave normal and

Poynting flux angles are compared during one auroral hiss event that contains some electromagnetic components. The results are shown to be consistent with propagation in a nearly electrostatic mode with wave normal angles close to the resonance cone.

1.2 Technical Contributions

Almost all previous studies of the wave normal directions have been limited to a single frequency channel at relatively low-time resolution or to wave normal direction spectra at single observation times. The data from the Polar Plasma Wave Instrument allow not only wave normal directions but also Poynting vector directions and polarizations to be measured and displayed on a frequency-time spectrogram with a frequency range of 0 to 25 kHz and a time resolution of approximately 0.01 seconds. The evolution of wave normal and Poynting flux directions can be easily studied in both time and frequency -- a significant advance over almost all previous studies.

Measurements of three-component wave electric fields are obtained simultaneously with measurements of three-component wave magnetic fields. No previous wave instrument flown in the Earth's outer magnetosphere has been capable of measuring the full six-component wave field. This capability allows the wave normal direction to be calculated without ambiguity (discussed in Chapter 2). The Poynting vector can also be calculated with high time and frequency resolution from direct measurements. Only a few previous studies have attempted to calculate

Poynting vectors, usually by constructing the third, unmeasured, electric field component using Maxwell's equations and models of the magnetoplasma characteristics.

The high-time-resolution spectra of both wave normal and Poynting vectors can be averaged to produce lower temporal resolution survey mode spectrograms. These can be used to examine the propagation characteristics of waves observed over time periods of up to two hours in length. This capability can be used to examine large amounts of data in order to identify interesting phenomena for more detailed study, or to conduct statistical studies of many occurrences of a single type of wave emission.

The Polar Plasma Wave Instrument (PWI) is well-suited for the study of whistler-mode waves in the Earth's magnetosphere for several reasons. The Polar satellite has an elliptical orbit with inclination near 86° that allows the spacecraft to sample high-altitude auroral and polar regions, the mid-latitude magnetosphere, the plasmasphere, and low-altitude auroral and polar regions. These regions contain many different electrostatic and electromagnetic emissions that are observed using the Polar PWI. The High Frequency Waveform Receiver (HFWR) produces high-time-resolution snapshots of three orthogonal components of the wave electric field and three orthogonal components of the wave magnetic field. This instrument is the first to measure all six wave components simultaneously, providing a unique opportunity to make direct measurements of Poynting vector orientations, as well as

measurements of wave normal directions, with high-time resolution over a wide range of frequencies.

1.3 Thesis Organization

A description of the Polar orbit, the Plasma Wave Instrument, and the High Frequency Waveform Receiver data characteristics are included in Chapter 2. The data processing and calibration adjustments for the gain and phase shifts of the sensors and corresponding amplifiers are also described.

Chapter 3 provides a brief description of whistler-mode waves in a plasma and an overview of several of the best known methods for calculating wave normal directions. Included are the basic equations for these approaches as well as the details of several of their applications.

Chapter 4 contains a detailed description of the Means' method for calculating the wave normal direction for a single plane wave, and its application in this study. A brief description of the calculation of parameters to determine the applicability of this method and the straightforward calculation of the Poynting vector are then given.

Error analysis and verification of the wave normal and Poynting vector calculations are described in Chapter 5. First the characteristics of the spectral analysis are described. Then the wave normal and Poynting vector calculations are verified, and direction calculation errors estimated, using prelaunch test data collected by the PWI engineering staff prior to the start of this current study. The

vector orientations of whistlers and Omega transmitter signals are examined next. These are emissions that propagate from identifiable source locations, and their direction of propagation is used as a standard to verify the overall direction of our vector calculations. A discussion of the sources of error due to calibration and processing of the data is also included in Chapter 5. An estimation of the error of the calculated wave normal angles is computed using simulated data to which relative amplitude and phase changes are added.

Chapters 6 and 7 are devoted to the study of two types of whistler-mode emissions, chorus and auroral hiss. In Chapter 6, the direction of propagation of the wave energy is determined from Poynting flux directions for a large number of VLF chorus events. Early studies of chorus and the search for its generation region are described briefly. It is shown that chorus in the outer magnetosphere consistently propagates away from the magnetic equator. This result directly shows that the source region of chorus is near the magnetic equator. No evidence of chorus reflected from the high latitude magnetosphere is observed.

A brief study of auroral hiss propagation characteristics is conducted in Chapter 7. Auroral hiss is believed to propagate in a quasi-electrostatic mode with wave normal angle near the resonance cone angle. For quasi-electrostatic propagation, it can be shown that the Poynting vector of auroral hiss should be nearly perpendicular to the wave normal angle. This very unusual situation arises because the wave is propagating at wave normal angles very close to the resonance cone. The measured wave normal angle and Poynting vector angle are shown to

follow the frequency trends predicted by the quasi-electrostatic propagation theory for one auroral hiss event.

The applications and results of this study are presented in Chapter 8, as well as possible extensions of the current analysis methods.

CHAPTER II. POLAR PLASMA WAVE INSTRUMENT AND DATA PROCESSING

The Polar Plasma Wave Instrument (PWI) contains a set of five radio receivers that allow measurements of plasma waves in a wider range of magnetospheric regions and with greater time and frequency resolutions than any spacecraft previously flown in a polar orbit. The Polar spacecraft and orbit, the Plasma Wave Instrument, and preprocessing of the High Frequency Waveform Receiver (HFWR) data for use in this project are now described.

2.1 Polar Spacecraft and Plasma Wave Instrument

The Polar Plasma Wave Instrument (PWI) is ideally suited to measure magnetospheric plasma wave emissions. The Polar orbit has an apogee of $9 R_E$, a perigee of $1.8 R_E$ and an inclination of approximately 90° [Acuña et al., 1995] so that the spacecraft passes through the plasmasphere, the cusp/cleft region, the low-altitude auroral and polar regions, and the high-altitude auroral and polar regions. A sketch of the Earth's magnetosphere, including the Polar orbit [after Parks, 1991; Acuña et al., 1995], is shown in Figure 1. The Plasma Wave Instrument consists of five receiver systems that measure electric and magnetic wave emissions from 0.1 Hz to 800 kHz: a wideband receiver, a High Frequency Waveform Receiver

(HFWR), a Low Frequency Waveform Receiver (LFWR), two multichannel analyzers, and a pair of sweep frequency receivers (SFR) [Gurnett et al., 1995]. Electric fields are measured using three orthogonal electric dipole antennas: two in the spin plane of the spacecraft with effective lengths of 129.4 and 101.2 meters, and one along the spin axis of the spacecraft with an effective length of 14.0 meters. Magnetic fields are measured by a magnetic loop antenna and a triaxial magnetic search coil antenna. The geometry of the electric and magnetic sensors on the Polar spacecraft is shown in Figure 2. The top view that more clearly shows the orientation of the electric antennas and search coils in the spin plane of the spacecraft is shown in Figure 3. The E_u antenna is oriented 45° from the boom that contains the Magnetic Fields Experiment (MFE), and defines the UVZ spacecraft-centered coordinate system. The magnetometer boom defines the x-axis of the spacecraft-centered XYZ coordinate system, called the rotating payload (RP) coordinate system. These and other coordinate systems used in this study are described in Appendix A. The High Frequency Waveform Receiver (HFWR) measures electric and magnetic signals from 20 Hz to 25 kHz in two modes, a low-telemetry-rate mode and a high-telemetry-rate mode. Waveforms of wave electric fields are measured using the three orthogonal dipole antennas, while waveforms of the magnetic fields are measured using the triaxial search coil magnetometers. In the low-telemetry-rate mode, the HFWR produces six simultaneous waveform snapshots once every 129 seconds using either a 2-kHz or a 16-kHz filter. In the high-telemetry-rate mode, 0.45-second waveforms of signals up to 25 kHz are

produced once every 9.2 seconds. The waveforms are split into subintervals and fast Fourier transforms are performed in each subinterval to calculate the power spectra of the waves measured by each sensor. Figure 4 shows the power spectra of the six-channel output from the HFWR high-rate mode on September 11, 1996, from 09:11:56 UT to 09:12:42 UT, $R = 2.5 R_E$, $L = 2.6$, magnetic latitude (MLAT) = 2.1° to 3.2° . The top three panels contain the power spectra of the wave electric fields measured along the u-, v-, and z-axes in the spacecraft rotating payload coordinate system and are labeled E_u , E_v , and E_z respectively. The fourth, fifth, and sixth panels display the power spectra of the wave magnetic fields measured along the same axes and are labeled B_u , B_v , and B_z . The horizontal axis of each panel shows a modified time scale. Each panel contains six snapshots of data, where each snapshot is the spectrum produced from one 0.45-second waveform. The black stripes that separate the snapshots represent the 8.75-second gaps between the data snapshots. The vertical scale ranges from 0 to 30 kHz. The intensity of the emissions (in relative dB) is denoted by the color bar to the right of each panel. Approximately 55 seconds of data are shown. The narrowband emissions that appear as horizontal lines in snapshots 1, 3, 5, and 6 at 11 and 13 kHz, are produced by a ground transmitter. These are called Omega signals. The curved signals in snapshots 3 and 4 are whistlers [Storey, 1953]. Whistlers are generated by lightning. Both of these signals will be described in Chapter 5. A narrowband electrostatic signal with gradually descending frequency is observed on the E_v antenna in snapshots 4, 5, and 6. This signal is unidentified and will not be

studied because no magnetic component (necessary for wave normal vector calculation) are observed. HFWR six-channel spectrograms are produced using software developed by the PWI data analyst/programmer team.

Once some processing has been performed, data from the HFWR in high-rate mode is used to produce spectrograms showing the orientation of the wave normal and Poynting vector of a variety of magnetospheric electromagnetic plasma waves.

2.2 Data Preparation

When in the high-telemetry-rate, six-channel mode, the HFWR produces six simultaneous time-series of data, three from the three electric and three from the triaxial search coil magnetometer. Each time series produced by the HFWR in this mode contains 31,816 data points with a sample spacing of 0.014 msec and sampling rate of 71.43 kHz. The wave normal and Poynting vectors are calculated in a coordinate system aligned with the static geomagnetic field, but the wave signals are measured in the spinning reference frame of the spacecraft. The voltage signals measured by the electric antennas are converted to electric field units (V/m) while still in the coordinate system of the spinning spacecraft so that the correct antenna lengths are used. Conversion of the signals measured by the magnetometers to magnetic field units (nanoTesla), as well as corrections for gain and phase shifts due to sensor and preamplifier characteristics, which are frequency-dependent, are performed after the time series has been Fourier transformed.

The sensor gain and phase corrections could be applied in several ways. The signals could be Fourier transformed while still in RP coordinates, calibrated, then inverse Fourier transformed. This produces a calibrated time series in RP coordinates that is then transformed to FP coordinates. This method has the disadvantage of requiring both a forward and an inverse Fourier transform for each signal, and would increase the computer processing time significantly.

An alternative processing method would be to apply the frequency dependent calibrations in the time domain before despinning. This is a difficult process and the additional computing time required to perform this time domain processing was not justified for this study. In a third calibration method, the signals measured in the RP coordinate system are Fourier transformed, then calibrated. The calibrated signals can then be used to find wave normal and Poynting vectors. The third method mixes the signals measured along the u and v directions in the spin plane of the spacecraft. The third method was chosen because it requires the least computer processing. The errors introduced by this method are acceptably small. The gain and phase corrections, and the small error introduced by the correction method, are discussed in sections 2.3.1 and 2.3.2.

Once the signals measured by the electric fields have been converted to electric field units, the signals in all six channels are transformed into a non-rotating, spacecraft-centered reference frame called the Fixed-Payload (FP) coordinate system described in Appendix A. In the FP system, the positive z -axis is parallel to the spin axis of the spacecraft, the x -axis is perpendicular to the z -axis

and is in the meridian plane containing the radius vector to the Sun and is positive toward the Sun. The y-axis completes the right-hand system. The wave normal and Poynting vectors are computed in FP coordinates, and are then rotated into a coordinate system aligned along the static geomagnetic field called the local magnetic field-aligned coordinate (FAC) system. The spin phase of the spacecraft relative to the spacecraft-Sun line is required to transform from UVZ coordinates to FP coordinates. The transformation from FP to FAC coordinates uses the geomagnetic field vector, \vec{B}_0 , in Geocentric Solar Ecliptic (GSE) coordinates, and the matrix for transformation from FP to GSE coordinates. The \vec{B}_0 and transformation matrix data are provided once per snapshot. The geomagnetic field data are provided by the Magnetic Field Experiment (MFE) on Polar [Russell et al., 1995]. The transformation matrices are determined using software available from the International Solar-Terrestrial Physics (ISTP) Central Data Handling Facility (CDHF). The despun data, geomagnetic field vector, and coordinate transformation matrices are provided by software written by PWI data analyst/programmer team and then used for the present study.

2.3 Sensor Calibrations

The electric and magnetic sensors and the differential amplifiers in the PWI have frequency-dependent gain and phase characteristics that cause the signals measured by these sensors to have different amplitudes and phases than the true signals. Because the phase characteristics of each of the sensors are slightly

different, the relative phases that are important in the calculation of the wave normal vector could be incorrect. Although not used in the present study, the correct magnitude of the Poynting flux depends on use of the correct magnetic and electric field strengths. For these reasons it is necessary to correct for the gain and phase characteristics of each of the sensors.

2.3.1 Search Coil Calibrations

The search coil magnetometers and the PWI differential amplifiers for these sensors introduce a frequency-dependent phase shift into the measured signals. The total phase lags for each search coil differential amplifiers set was measured at several frequencies and are listed in Table 1 in Appendix B. The conversion from volts to nT is also frequency dependent and so both the correction for the phase shift of the sensors as well as conversion to nT is performed after the time series data has been Fourier transformed. The phase correction and volts-to-nT conversion factors are calculated at the desired frequency using linear interpolation between the values given in the tables. The phase corrections are applied to the real and imaginary components of each Fourier coefficient using the following relationships:

$$B_r' = B_r \cos\theta + B_i \sin\theta \quad (1)$$

$$B_i' = -B_r \sin\theta + B_i \cos\theta \quad (2)$$

where θ is the phase lag computed for the given Fourier frequency, B_r and B_i are the real and imaginary Fourier coefficients (at each Fourier frequency), respectively, of the measured signal, and B_r' and B_i' are the real and imaginary Fourier coefficients corrected for the sensor phase lag.

Because the phase corrections are frequency-dependent, they must be applied to the signals after Fourier transformation. However, the spin modulation of the signals measured along the two sensor axes in the spin plane of the spacecraft must be removed by transformation to fixed-payload (FP) coordinates before the FFT can be applied to the signals measured along these directions. The signals in the x and y directions in FP coordinates are therefore mixtures of the signals measured along the u and v directions in the rotating payload coordinate system of the spinning spacecraft. The phase corrections for the individual search coil cannot therefore be applied to the signal measured by that search coil. The phase calibration values for the B_u search coil were chosen to calibrate the magnetic signals measured in the x and y directions of the FP coordinate system. As can be seen from Table 1 there is little difference between the phase shifts of the B_u and B_v search coils. The phase calibration values for the B_z search coil were used to calibrate the magnetic signals measured in the z direction.

2.3.2 Electric Antenna Calibrations

The PWI electric antennas and the associated differential amplifiers introduce a gain and a phase shift to the measured signals [Harvey et al., 1995]. The gains

and phase shifts were determined by driving the preamplifiers with a series resistance of 10 MOhms in parallel with a 10 pFarad capacitance to simulate a plasma. The gains of each of the three electric sensors are given in Table 2. The phase shifts of each of the electric sensors are given in Table 3. The gain and phase corrections are applied to the electric signals with the following relationships:

$$E_r' = G(E_r \cos\theta + E_i \sin\theta) \quad (3)$$

where θ is the phase lag computed for the given Fourier frequency, G is a gain

$$E_i' = G(-E_r \sin\theta + E_i \cos\theta) \quad (4)$$

factor to convert from measured V/m to true V/m, E_r and E_i are the real and imaginary Fourier coefficients (at each Fourier frequency), respectively, of the measured signal, and E_r' and E_i' are the real and imaginary Fourier coefficients corrected for the sensor phase lag and gain. For the same reason stated above, one set of gain and phase values was chosen to calibrate the signals in the x- and y-directions of the FP system. The E_u gain and phase calibrations were chosen because the phase shift at 10 Hz was 0 degrees, the expected value for these pre-amps. The relative phase shifts between the E_u and E_v pre-amps is generally very small, within a few tenths of a degree, except near 1 kHz when the difference in phase shift is 0.9 degrees.

CHAPTER III. THE WHISTLER-MODE AND WAVE NORMAL ANALYSIS METHODS

Magnetospheric chorus and auroral hiss propagate with frequencies below the local electron cyclotron and electron plasma frequency, but above local ion cyclotron frequencies. In this frequency range, the only electromagnetic mode of propagation is the whistler mode. Therefore, this chapter will begin with an introduction to the whistler mode. Methods for calculating wave normal directions and their application to the study of whistler-mode waves are then described. The last section of the chapter describes previous studies of the Poynting flux of whistler-mode waves.

3.1 Whistler-Mode Dispersion Relation

The dispersion relation $D(\vec{k}, \omega) = 0$ relates the angular frequency $\omega = 2\pi f$ and the wave vector \vec{k} of a plasma wave. The frequency is given by f and the magnitude of the wave vector is $k = 2\pi/\lambda$ where λ is the wavelength. The whistler-mode dispersion relation is found by considering waves in a cold magnetized plasma. The electric and magnetic fields, \vec{E} and \vec{B} , are taken to be the sum of a zero-order term plus a small amplitude first-order term of the form $\exp(i(\vec{k} \cdot \vec{r} - \omega t))$. This discussion of the whistler-mode dispersion relation follows that of Stix [1993].

Maxwell's equations are used to find the dispersion relation. Eliminating \vec{B} between the Fourier transformed Faraday's law and Ampere's law results in a homogeneous equation for the electric field:

$$\vec{k} \times (\vec{k} \times \vec{E}) + \frac{\omega^2}{c^2} \vec{K} \cdot \vec{E} = 0 \quad (5)$$

where \vec{K} is the dielectric tensor. This equation can be found in terms of the index of refraction by using the relationship

$$\vec{n} = \frac{c\vec{k}}{\omega} \quad (6)$$

The homogeneous equation then becomes

$$\vec{n} \times (\vec{n} \times \vec{E}) + \vec{K} \cdot \vec{E} = 0 \quad (7)$$

This equation can be written in matrix form as $\vec{D} \cdot \vec{E} = 0$. There is a non-trivial solution to this equation if and only if the determinant of \vec{D} is zero. This determinant gives the dispersion relation

$$D(\vec{k}, \omega) = \text{Det}(\vec{D}) = 0 \quad (8)$$

For waves in a cold plasma with a magnetic field, Stix [1993] shows that the dielectric tensor has the form

$$\vec{K} = \begin{bmatrix} S & -iD & 0 \\ iD & S & 0 \\ 0 & 0 & P \end{bmatrix} \quad (9)$$

where

$$S \equiv 1 - \sum_s \frac{\omega_{ps}^2}{\omega^2 - \omega_{cs}^2} \quad (10a)$$

$$D \equiv \sum_s \frac{\omega_{cs} \omega_{ps}^2}{\omega(\omega^2 - \omega_{cs}^2)} \quad (10b)$$

$$P \equiv 1 - \sum_s \frac{\omega_{ps}^2}{\omega^2}, \quad (10c)$$

and the cyclotron frequency and plasma frequency are defined by

$$\omega_{ps} = \sqrt{\frac{n_{s0} e_s^2}{\epsilon_0 m_s}} \quad (11)$$

and

$$\omega_{cs} = \frac{e_s B_0}{m_s} . \quad (12)$$

The equations for S and D and can be written in terms of a sum and a difference as follows

$$S = \frac{1}{2} (R + L) \quad (13a)$$

$$D = \frac{1}{2} (R - L) \quad (13b)$$

where

$$R \equiv 1 - \sum_s \frac{\omega_{ps}^2}{\omega(\omega + \omega_{cs})} \quad (14a)$$

and

$$L \equiv 1 - \sum_s \frac{\omega_{ps}^2}{\omega(\omega - \omega_{cs})} . \quad (14b)$$

The terms R and L are associated with right-hand and left-hand polarized modes, respectively. The terminology R (for right), L (for left), S (for sum), and D (for

difference) are defined in Stix [1993]. It is important to note that the cyclotron frequency depends on the sign of the charge for the species being considered. Thus, the electron cyclotron frequency will be negative but the cyclotron frequency for positively charged ions will be positive.

To find the matrix version of the homogeneous equation, the index of refraction vector can be rotated into the x-z plane so that $\vec{n} = (n \sin \theta, 0, n \cos \theta)$. This simplifies the calculation without loss of generality. From equations (7) and (9), the homogeneous equation becomes:

$$\begin{bmatrix} S - n^2 \cos 2\theta & -iD & n^2 \sin \theta \\ iD & S - n^2 & 0 \\ n^2 \sin \theta \cos \theta & 0 & P - n^2 \sin^2 \theta \end{bmatrix} \begin{bmatrix} E_x \\ E_y \\ E_z \end{bmatrix} = 0 \quad (15)$$

The homogeneous equation has a nonzero solution if the determinant of the matrix is zero. The determinant of the matrix gives the dispersion relation

$$D(\vec{n}, \omega) = A n^4 - B n^2 + RLP = 0, \quad (16)$$

where

$$A = S \sin^2 \theta + P \cos^2 \theta \quad (17a)$$

$$B = RL \sin^2 \theta + PS(1 + \cos^2 \theta) \quad (17b)$$

Equation (16) is the dispersion relation for waves in a cold magnetized plasma. The wave normal angle θ is the angle between the static magnetic field and the index of refraction vector \vec{n} (which is parallel to the wave vector \vec{k}). Solving for n^2 gives

$$n^2 = \frac{B \pm F}{2A} \quad (18)$$

By using the identity $S^2 - D^2 = RL$, one can show that

$$F^2 = (RL - PS)^2 \sin^4 \theta + 4 P^2 D^2 \cos^2 \theta \quad (19)$$

Another form of this dispersion relation is

$$\tan^2 \theta = \frac{-P(n^2 - R)(n^2 - L)}{(S n^2 - RL)(n^2 - P)} \quad (20)$$

By considering propagation parallel to the magnetic field, $\theta = 0$, it can be shown that there are three roots to equation (20). The roots are $n^2 = R$, $n^2 = L$, $P = 0$. The $n^2 = R$ root corresponds to a right-hand polarized wave and is given by

$$n^2 = 1 - \sum_s \frac{\omega_{ps}^2}{\omega(\omega + \omega_{cs})} \quad (21)$$

This is the whistler-dispersion relation for $\theta = 0$. Recalling that $\omega_{ce} < 0$, it is seen that n^2 becomes infinite (i.e., n has a resonance) at the electron cyclotron frequency, $\omega = |\omega_{ce}|$. Therefore the whistler-mode dispersion relation applies to waves with frequencies less than the electron cyclotron frequency.

Conditions often exist in the magnetosphere that yield $n \gg 1$. In this case the one in the index of refraction equation can be discarded. It is also usually possible to ignore ion contributions. The dispersion relation then becomes

$$n^2 = \frac{\omega_{ps}^2}{\omega(\omega_c - \omega)} \quad (22)$$

where ω_p stands for ω_{pe} , and ω_c stands for $|\omega_{ce}|$. It can also be shown that the group velocity (energy propagation speed), for parallel propagation $v_g = \partial\omega/\partial k$, is

$$v_g = 2c \frac{\omega^{1/2}(\omega_c - \omega)^{3/2}}{(\omega_c - \omega_p)} \quad (23)$$

To find the index of refraction for the whistler mode with oblique wave normal angles some simplifying assumptions must be made. First, the ion terms are neglected. This assumption is valid for frequencies down to approximately the ion cyclotron frequency. Second, the wave frequency and the electron cyclotron frequency are assumed to be much less than the plasma frequency, $\omega^2 \ll \omega_p^2$ and

$\omega_c^2 < \omega_p^2$. This is called the high density approximation because ω_p^2 is proportional to the electron density. The index of refraction is then

$$n^2 = \frac{\omega_p^2}{\omega(\omega_c \cos \theta - \omega)} \quad (24)$$

The index of refraction becomes infinite at the resonance cone angle, θ_{Res} , given by

$$\cos \theta_{\text{Res}} = \frac{\omega}{\omega_c} \quad (25)$$

A polar plot of the index of refraction $n(\theta)$ for this frequency range is shown in Figure 5. The dashed lines indicate the resonance cone angle and \vec{B} is the direction of the magnetic field. The Poynting vector \vec{S} , which is in the same direction as the group velocity, is perpendicular to the index of refraction surface. The index of refraction vector \vec{n} and the Poynting vector are shown for one value of the wave normal angle θ . The angle between the magnetic field and \vec{S} is labeled as θ_s .

A further simplification of the index of refraction equation is found by making the low-frequency approximation, $\omega \ll \omega_c$. The index of refraction then becomes

$$n^2 = \frac{\omega_p^2}{\omega \omega_c \cos \theta} \quad (26)$$

and the resonance cone angle becomes $\theta_{\text{Res}} \approx \pi/2$.

In this limit the group velocity is nearly parallel to the magnetic field at all frequencies. It has been shown by Storey [1953] that the angle ψ between the group velocity and the magnetic field has a maximum of $\psi_{\max} = \tan^{-1} 1/\sqrt{8} = 19^\circ 28'$. This means that whistler-mode waves are guided by the magnetic field, even for oblique wave normal angles.

3.2 Wave Normal Vector Determination

A plane wave can be represented by the expression $\tilde{B}(\vec{r}, t) = \tilde{B}_0 \exp[i(\vec{k} \cdot \vec{r} - \omega t)]$ where $\tilde{}$ denotes a complex quantity. \tilde{B}_0 is the amplitude of the wave, ω is the wave frequency, \vec{r} is a radial position vector, t is time, and $\hat{k} = \vec{k} / k$ is the wave vector. The magnitude of the wave normal vector is the wave number, $k = 2\pi/\lambda$, where λ is the wavelength. The wave normal vector, \vec{k} , is perpendicular to the plane of rotation of the magnetic field. It is often useful to represent a plane wave in terms of a Fourier transform. In one dimension, a function can be represented as

$$f(x) = \frac{1}{\sqrt{2\pi}} \int_{-\infty}^{\infty} \tilde{f}(k) e^{-ikx} dk, \quad (27)$$

where $\tilde{f}(k)$ is the Fourier transform. This can be extended to four dimensions as

$$f(\vec{r}, t) = \frac{1}{(2\pi)^2} \iiint \tilde{f}(\vec{k}, \omega) e^{i(\vec{k} \cdot \vec{r} - \omega t)} d^3k d\omega, \quad (28)$$

where $d^3k = dk_x dk_y dk_z$. It can then be shown for a plane wave that $\vec{\nabla} \tilde{f}(\vec{r}, t) = i \vec{k} f(\vec{k}, \omega)$. The relationship of \vec{k} to the wave magnetic field is found by examining one of Maxwell's equations, $\vec{\nabla} \cdot \vec{B} = 0$. By letting $\vec{B} = \vec{B}_0 e^{i[\vec{k} \cdot \vec{r} - \omega t]}$ and taking the Fourier transform, $\vec{\nabla} \cdot \vec{B} = 0$ becomes $\vec{k} \cdot \vec{B} = 0$. Hence, the wave normal vector is perpendicular to the plane of rotation of the magnetic wave field. It is important to note that by considering only the magnetic wave field, \vec{k} can be determined only to within 180° . This ambiguity can be resolved only by using measurements of the electric wave field.

Wave normal vector orientations of ionospheric and magnetospheric electromagnetic wave emissions have been determined from satellite measurements of wave electric and magnetic fields using several different methods. Most of these methods begin by calculating the coherence or covariance matrix. The components of this matrix are the self- and cross-products of the orthogonal magnetic wave field signals [Born and Wolf, 1970; Fowler et al., 1967; Means, 1972]. The covariance matrix is given by $J_{\alpha\beta} = \langle B_\alpha(t) B_\beta^*(t) \rangle$, where the brackets denote time averages and the * denotes the complex conjugate. When the covariance matrix is constructed using the frequency domain representation of the wave signals it is called the cross-spectral (or spectral) matrix. The spectral matrix has the form $J_{\alpha\beta} = \{ B_\alpha(f) B_\beta^*(f) \}$. The braces represent averages over frequency and * represents the complex conjugate. The terms $\{ B_\alpha(f) B_\beta^*(f) \}$ are the auto- and cross-power spectra of signals measured along α - and β -axes. The auto- and cross-power spectra contain information about the relative phase between the signals used in their

construction. In the case of a plane polarized wave, the relative phase between signals measured in a plane perpendicular to the propagation direction remain nearly constant. The relative phase between uncorrelated signals is randomly distributed. Therefore, the covariance or spectral matrix is useful in determining the wave normal direction of plane waves and in determining the coherence between signals measured along different axes of the matrix coordinate system. The characteristics of the covariance matrix are discussed in detail in section 4.1. The principal axis system is one in which the wave normal vector is parallel to the z-axis, and the wave magnetic field lies in the x-y plane. The covariance matrix in the principal axis system can then be used in a two-dimensional polarization analysis such as that described by Fowler et al. [1967]. This method was used to calculate polarization characteristics of geomagnetic micropulsations [Rankin and Kurtz, 1970]. Several methods for computing the wave normal angle are now described.

3.2.1 Minimum Variance Method

One of the earliest methods used to find the wave normal vector is the minimum variance method, which uses the covariance matrix. The covariance matrix is constructed using the real waveforms of three orthogonal magnetic field measurements. The eigenvector corresponding to the smallest eigenvalue is the direction of minimum variance of the wave vector, i.e. the wave normal direction [Sonnerup and Cahill, 1967; McPherron et al., 1972, Smith and Tsurutani, 1976]. This method was first developed and used to calculate the normal to the

magnetopause [Sonnerup and Cahill, 1967]. Using many measurements of the magnetic induction taken near the magnetopause, the normal vector \hat{n} is found by minimizing the standard deviation of the individual products, $\vec{B}^i \cdot \hat{n}$, from the average value, $\langle \vec{B} \rangle \cdot \hat{n}$. B^i is an individual field measurement, $\langle \vec{B} \rangle$ is the average over N measurements and \hat{n} is the normal vector. The normal vector is determined by minimizing

$$\sigma^2 = \frac{1}{N} \sum_{i=1}^N \left[\vec{B}^i \cdot \hat{n} - \langle \vec{B} \rangle \cdot \hat{n} \right]^2 . \quad (29)$$

Sonnerup and Cahill also state that minimization of equation (29) is equivalent to finding the eigenvector corresponding to the smallest eigenvalue of the "covariant" matrix

$$M_{\alpha\beta} = (\langle B_{\alpha} B_{\beta} \rangle - \langle B_{\alpha} \rangle \langle B_{\beta} \rangle) \quad \alpha, \beta = 1, 2, 3 \quad (30)$$

where B_{α} and B_{β} are the components of the measured field vectors, and the brackets denote the average over the measurements used in the calculation. The normal vector is then the eigenvector corresponding to the smallest eigenvalue of $M_{\alpha\beta}$. The covariant matrix is constructed from the auto- and cross-power spectral densities calculated using the root-mean-square deviation of the geomagnetic field measurements and is a real matrix. It is analogous to the covariance matrix, $J_{\alpha\beta} = \langle B_{\alpha}(t) B_{\beta}^*(t) \rangle$, which is composed of the auto- and cross-power spectral densities of wave magnetic fields. By using measurements of wave magnetic fields

in place of the geomagnetic field data used to locate the magnetopause this method was subsequently used to study polarization and wave normal orientations of plasmaspheric hiss [Thorne et al., 1973], and of magnetosheath lion roar emissions [Smith and Tsurutani, 1976]. An analytic representation of the magnetic time series can be obtained, for example, by taking the Fourier transform of the data. The spectral matrix computed using the analytic expressions is then complex. A method analogous to that of Sonnerup and Cahill [1967] calculates the eigenvectors of the real symmetric part of the spectral matrix by diagonalization. The eigenvectors define the principal axis system, and the eigenvector corresponding to the smallest eigenvalue is parallel to the wave normal vector [McPherron et al., 1972; Chan et al., 1972]. Because only magnetic field components are used, the wave normal vector is determined with a 180° ambiguity. Chan et al. [1972] found the polarization and wave normal direction of ionospheric proton whistlers observed by OGO 6 at 0.01 second time resolution with a single frequency band between 10 and 1000 Hz using this method.

3.2.2 Means' Method

A related method for calculation of the wave normal vector determines the components of the wave normal vector from the imaginary part of the covariance matrix [Means, 1972]. This method has the advantages that fewer computational steps are necessary than in the eigenvector analysis, and the wave signals that enter the imaginary part of the matrix are less susceptible to incoherent background noise

signals. This method was subsequently applied to a statistical study of wave normal orientations of chorus emissions observed by OGO 5 [Burton and Holzer, 1974]. The wave normal orientations were determined for a single frequency band from 10 Hz to 2.5 kHz. The imaginary part of the covariance matrix is used to determine the wave normal vectors for the current study, and a detailed description of its implementation will be discussed in Chapter 4.

3.2.3 Eigenvector Method

Wave normal directions can be determined directly from the spectral matrix in one more way. If there are not more than two non-zero eigenvalues, the number of non-zero eigenvalues corresponds to the number of waves present. The eigenvectors, \bar{u} , of the spectral matrix, \bar{S} , are given by the eigenvector equation

$$\bar{S} \bar{u} = \lambda \bar{u} \quad (31)$$

where λ is the eigenvalue corresponding to the complex eigenvector $\bar{u} = \bar{r}_1 + i\bar{r}_2$. The vectors, \bar{r}_1 and \bar{r}_2 , are in the plane of rotation of the magnetic field. The wave normal vector corresponding to each eigenvalue is parallel to the vector product of the real and imaginary part of the corresponding eigenvector, i.e.,

$$\hat{k} \parallel (\bar{r}_1 \times \bar{r}_2) \quad (32)$$

[Samson, 1977; Samson and Olson, 1980]. If there are three non-zero eigenvalues, three or more waves are present and the wave normal directions cannot be determined. This method has been applied as part of a statistical study of extremely-low-frequency (ELF) ion cyclotron waves near the equator observed by the EXOS-D (Akebono) satellite [Kasahara et al., 1992; Kasahara, 1995].

3.2.4 Wave Distribution Function Method

Wave propagation characteristics can also be determined through construction of a function that describes the distribution of wave energy as a function of frequency and wave normal direction. This function is called the wave distribution function (WDF). The wave field is assumed to be the sum of the fields due to many plane waves propagating in different directions with no mutual coherence [Storey, 1971; Storey and Lefeuvre, 1974, 1979, 1980]. This method uses the electric as well as the magnetic wave field components to form the spectral matrix. The components of the wave electric field, E_x , E_y , E_z , and the wave magnetic field, H_x , H_y , H_z , are first used to define a six-component generalized field vector \mathcal{E} :

$$\mathcal{E}_{1,2,3} = E_{x,y,z} ; \quad \mathcal{E}_{4,5,6} = Z_0 H_{x,y,z} \quad (33)$$

where Z_0 is the wave impedance of free space. The resulting spectral matrix is a 6×6 matrix whose elements, $S_{ij}(\omega) = \mathcal{E}_i(\omega) \mathcal{E}_j^*(\omega)$, are either the auto-power spectrum of \mathcal{E}_i (if $i = j$) or the cross-power spectrum of \mathcal{E}_i and \mathcal{E}_j (if $i \neq j$).

Storey and Lefeuvre [1979] show that for a given frequency ω , the WDF is related to the spectral matrix by

$$S_{ij}(\omega) = \frac{\pi}{2} \int_0^{2\pi} \int_0^{\pi} a_{ij}(\omega, \theta, \phi) F(\omega, \theta, \phi) \sin\theta \, d\theta \, d\phi \quad (34)$$

where θ is the wave normal angle and ϕ is an azimuthal angle of the wave normal direction measured from the meridian plane containing the point of measurement. $F(\omega, \theta, \phi)$ is the wave distribution function to be found using the integration kernels, $a_{ij}(\omega, \theta, \phi)$, whose form depends on plasma conditions and the wave mode being analyzed. The general form of the integration kernels is given by Storey and Lefeuvre [1980]. The integration is performed over a unit sphere. Using the measured spectral matrix and integration kernels that adequately model the magnetoplasma, the wave distribution function is estimated by solving equations (34). Buchalet and Lefeuvre [1981] modeled the WDF for single or multiple directions of propagation as

$$F(\omega, \theta, \phi) = \sum_k \rho_k \delta(\cos\theta - \cos\theta_k) \delta(\phi - \phi_k) \quad (35)$$

where δ is the Dirac delta function, and ρ_k is the energy density. θ_k and ϕ_k define the direction of propagation of each wave, indexed by k . Kasahara et al. [1994] and Kasahara [1995] used two models for the WDF. One model is the maximum

entropy method (MEM) [Lefeuvre and Delannoy, 1979; Lefeuvre et al., 1981] in which the entropy of the WDF is given as:

$$H(F) = \int_0^{2\pi} \int_0^{\pi} F \log \frac{1}{F} d\theta d\phi \quad . \quad (36)$$

When $H(F)$ is a maximum under equation (34), F has the form

$$F(\theta, \phi) = \exp \left[-1 + \sum_{i=1}^N \mu_i q_i(\theta, \phi) \right] \quad (37)$$

where μ_i are Lagrange multipliers and the q_i are the integration kernels, i.e., $q_1 = a_{11}$, $q_2 = a_{12}$, . . . , $q_{36} = a_{66}$. Solving for the Lagrange multipliers then determines F . The second method used by Kasahara et al. [1994] is the Phillips-Tikhonov regularization method [Yamaguchi et al., 1992] in which $F(\omega, \theta, \phi)$ is determined by minimizing the function:

$$R(F) = \iint |\nabla^2 F(\theta, \phi)|^2 \sin \theta d\theta d\phi \quad . \quad (38)$$

WDF methods have been used to find the direction of propagation of one-half cyclotron frequency emissions observed by the GEOS 1 S-300 experiment [Muto et al., 1987] and to study plasmaspheric hiss observed by ISEE 1 [Storey et al., 1991]. This method was also used to study ion cyclotron waves and multiband structured

emissions near the magnetic equator, auroral hiss, and saucers observed by the Akebono satellite [Kasahara et al., 1994; Kasahara, 1995].

3.2.5 Maximum Likelihood Method

In the maximum likelihood method, an expression for the theoretical spectral matrix is used to construct a likelihood function. This function is based on the WDF and the probability that the measured data are reproduced by the theoretical expression using a given set of plasma parameters. The most likely values of the parameters are those that maximize the likelihood function. This method has the advantage over single-plane wave methods that a one- or two-direction model can be used, allowing determination of the direction of propagation for one or two waves that may be present in a given measurement [Buchalet and Lefeuvre, 1981]. This method was applied to an Omega signal and to a few 70-ms segments of chorus emission (at a single frequency) using data provided by the GEOS 1 S-300 instrument [Buchalet and Lefeuvre, 1981]. This method was also used to determine wave normal directions of impulsive and rising-tone chorus as a function of the frequency of the emission in a more extensive study utilizing GEOS 2 S-300 data [Hayakawa et al., 1984].

3.2.6 Spin Modulation Method

Examination of the modulation of the electric wave signal due to the rotation of a dipole antenna on a spin-stabilized spacecraft can also be used to find wave

normal directions. This method was first used to find the direction of propagation of type III solar radio bursts in the spin plane of the IMP 6 spacecraft by Fainberg et al. [1972]. Spin modulation was subsequently used to find the direction of propagation of auroral kilometric radiation [Kurth et al., 1975; Gurnett, 1974] and other emissions. This method has been expanded by including a magnetic wave field measurement. Spin fading and Doppler shifts of waves arriving at the spacecraft from different directions create an envelope pattern in the signal. Multiple wave normal directions in three dimensions can then be determined [Sonwalker et al., 1984; Sonwalker and Inan, 1986]. This method is somewhat less general than previous methods since the waves must obey the whistler-mode dispersion relation. Spin fading has been used to observe the wave normal direction of artificially generated VLF whistler-mode signals observed by ISEE 1 [Sonwalker et al., 1984] and by DE 1 [Sonwalker and Inan, 1986], and was extended to produce a field distribution function (FDF) to determine wave normal directions of whistler-mode hiss observed by DE 1 [Sonwalker and Inan, 1988].

3.2.7 Amplitude Method

A more recent method that can be used when the relative phases of the magnetic signals are not known, calculates the wave normal direction by using only the amplitudes of three orthogonal magnetic signals and two orthogonal electric signals. This method also assumes whistler-mode propagation, and produces wave normal directions to within a 180° ambiguity which cannot be resolved [Sakamoto et

al., 1995]. The results produced are consistent with results from Means' method when applied to Omega signals observed by the Akebono Poynting Flux analyzers [Sakamoto et al., 1995].

3.3 Poynting Vector Determination

As an electromagnetic wave propagates, it carries energy along with it. The electromagnetic energy flux density, or energy per unit time per unit area, transported by the wave fields is given by the Poynting vector,

$$\vec{S} = \frac{1}{\mu_0} (\vec{E} \times \vec{B}) \quad , \quad (39)$$

[see Griffiths, 1989]. The Poynting vector gives the direction of energy flow of the wave. This defines the path that the wave follows, called the ray path. The ray path is calculated in the ray tracing simulations to predict the propagation of modeled waves. The Poynting vector is also parallel to the direction of the group velocity of the wave, $\vec{v}_g = \vec{\nabla}_k \omega$. This can be seen for the case of waves propagating in the same direction with a distribution of frequencies that differ by a small amount from a given frequency ω . The resulting waveform consists of a plane wave that propagates at the phase velocity $\vec{v}_p = \omega/\vec{k}$, modulated by an outer envelope (the wave packet) that propagates at the group velocity. Because the energy is carried by the wave packet, the direction and speed of energy propagation are given by the group velocity. For a detailed description of the relationship between the Poynting vector and the group velocity, see Stix [1993].

Poynting vector calculation is a somewhat more difficult task than wave normal calculation because a complete determination requires three orthogonal measurements of the wave electric field as well as the three measurements of the wave magnetic field. While it is common to obtain all three components of the magnetic vector, only one or two components of the electric vector have been measured by most satellites in the past (usually in the spin plane of a spin-stabilized satellite). Early studies calculated the component of the Poynting vector along the static geomagnetic field by using one electric component and one magnetic component that are orthogonal to each other and to the local static magnetic field [Gurnett et al., 1969; Mosier and Gurnett, 1971]. This method can determine only whether the average Poynting vector has a component that is parallel or antiparallel to the local geomagnetic field. A variety of low-altitude emissions observed by the Injun 5 satellite including proton whistlers, ELF hiss, VLF hiss, chorus and saucers [Gurnett et al., 1969; Mosier and Gurnett, 1969] were studied using this technique. Color spectrograms of these emissions were produced where color represented the direction of the Poynting flux, either up or down the geomagnetic field [Gurnett et al., 1971].

The total field-aligned component of the quasi-dc Poynting flux was calculated from the electric and magnetic wave fields measured in the plane perpendicular to the local geomagnetic field by the HILAT satellite [Kelley et al., 1991]. The Poynting flux was also calculated using higher resolution electric and magnetic field measurements observed by the sounding rocket Main as it flew

through an auroral arc. The Poynting flux along the magnetic field was combined with the electron energy flux to study the total downward energy flow from the auroral arc [Kletzing et al., 1996]. These methods were used to estimate energy flow into the atmosphere in the polar cap, but do not provide the azimuthal orientation of the Poynting vector.

The Poynting flux has also been estimated using measurements obtained by the Poynting Flux analyzer (PFX) on board Akebono. This instrument provides three orthogonal magnetic wave field measurements and two electric wave field measurements. The Poynting flux is calculated in the principle axis system determined by the wave normal direction, using the five wave field measurements and an expression for the index of refraction. The index of refraction is calculated from the wave normal vector, the plasma and cyclotron frequencies, and the impedance of free space. This method, like the amplitude method for calculating wave normal direction, works for circularly polarized whistler-mode waves, but only components of the Poynting vector in the plane defined by the wave normal vector and the geomagnetic field are produced [Sakamoto et al., 1995]. No Poynting vector orientations were presented.

CHAPTER IV. WAVE NORMAL AND POYNTING VECTOR CALCULATION

4.1 Wave Normal Calculation (Means' Method)

In this method wave normal vectors are calculated using the imaginary part of the cross-spectral matrix [Means, 1972]. This method works for signals of quasi-monochromatic, plane-wave signals with the form

$$B_j(t) = a_j(t) \exp \{ i [\omega t + \phi_j(t)] \} \quad . \quad (40)$$

The three magnetic waveforms are split into overlapping subintervals and an FFT is applied to the signals in each subinterval. The cross-spectral matrix, \bar{J} , is constructed from the auto-power and cross-power spectral density estimates of the resulting frequency spectra of the waveform subintervals:

$$\bar{J} = \begin{bmatrix} \langle B_x(f) B_x^*(f) \rangle & \langle B_x(f) B_y^*(f) \rangle & \langle B_x(f) B_z^*(f) \rangle \\ \langle B_y(f) B_x^*(f) \rangle & \langle B_y(f) B_y^*(f) \rangle & \langle B_y(f) B_z^*(f) \rangle \\ \langle B_z(f) B_x^*(f) \rangle & \langle B_z(f) B_y^*(f) \rangle & \langle B_z(f) B_z^*(f) \rangle \end{bmatrix} \quad (41)$$

The brackets represent averages over frequency. Averaging over a number of adjacent frequency bins, or smoothing of the spectrum, is necessary to increase the level of confidence of individual spectral estimates and to determine the coherence

of the wave signals being measured. If no averaging is performed, the variance of individual auto-power and cross-power spectral estimates is on the order of the estimates [Bendat and Piersol, 1986; Brigham, 1988]. If the analysis is performed at the $\Delta f \Delta t = 1$ limit of the Fourier analysis then the coherence of a signal measured at a given frequency will always be equal to unity. Smoothing is performed to reduce the variance of the estimates, and to allow the coherence to be calculated. The coherence is then used as a test condition for applying the analysis to the data. The details of the spectral smoothing and resulting temporal and frequency resolutions will be described in a later section.

The coherence between two signals measured along the i and j axes is given in terms of the spectral matrix elements as

$$C_{ij} = \frac{|J_{ij}|}{(J_{ii} J_{jj})^{1/2}} \quad (42)$$

The coherence will be unity for completely polarized waves and zero for signals with no correlation, i.e. uncorrelated noise in the three sensors.

The way in which different signals enter the spectral matrix can be seen by examination of the x - y element, $\{B_x(f) B_y(f)^*\}$. No *a priori* knowledge of the relationship between the two signals is assumed. For a given frequency, the signals can be represented by the Fourier transform coefficients as:

$$B_x(f) = A_f \cos\theta_f + i A_f \sin\theta_f \quad (43)$$

$$B_y(f) = B_f \cos\phi_f + i B_f \sin\phi_f \quad (44)$$

where θ_f and ϕ_f are the signal phases defined from the same arbitrary zero position.

The matrix element is

$$B_x(f)B_y(f)^* = A_f B_f \{ [\cos\theta_f \cos\phi_f + \sin\theta_f \sin\phi_f] + i [\sin\theta_f \cos\phi_f - \cos\theta_f \sin\phi_f] \} \quad (45)$$

which simplifies to

$$B_x(f)B_y(f)^* = A_f B_f \cos(\theta_f - \phi_f) + i A_f B_f \sin(\theta_f - \phi_f) \quad (46)$$

The diagonal elements will be real and positive since there is no phase difference between a signal and its conjugate. If the off-diagonal terms are non-zero, then the signals are at least partially coherent. The off-diagonal terms are imaginary when $(\theta_f - \phi_f) = \pm \pi/2$, i.e. coherent signals in quadrature to one another. For any other type of signal (in-phase coherent, out-of-phase coherent and uncorrelated noise) the off-diagonal elements will be real. By using the imaginary part of the spectral

matrix, only the waves of interest (i.e., coherent whistler-mode waves) will be considered and the effects of noise will not be included.

The cross-spectral matrix is a Hermitian matrix. The time resolution is determined by the number of subintervals that the waveform has been split into. The number of Fourier components that are used to perform the frequency averaging determines the frequency resolution. Means [1972] shows that a rotation of the spectral matrix about the wave normal direction leaves the imaginary part of the spectral matrix unchanged. Means draws an analogy between the imaginary part of the spectral matrix and the matrix of an infinitesimal rotation [Goldstein, 1980]. This analogy allows the components of the unit wave normal vector to be calculated from the elements of the imaginary part of \tilde{J} as:

$$k_x = J_{yz} / (J_{xy}^2 + J_{xz}^2 + J_{yz}^2) \quad (47a)$$

$$k_y = -J_{xz} / (J_{xy}^2 + J_{xz}^2 + J_{yz}^2) \quad (47b)$$

$$k_z = J_{xy} / (J_{xy}^2 + J_{xz}^2 + J_{yz}^2) \quad (47c)$$

Once the unit wave normal vector is determined, the cross-spectral matrix is transformed into a coordinate system in which the z-axis contains the wave normal vector. In this principal axis system a single plane wave will be contained entirely

in the x-y plane. To test for the presence of a coherent wave, the coherence C_{xy} is calculated:

$$C_{xy} = \frac{|J_{xy}|}{(J_{xx} J_{yy})^{1/2}} \quad (48)$$

A coherence of 1 denotes a completely coherent wave and a coherence of 0 indicates uncorrelated noise in the x and y directions.

It is also useful to calculate the signal to noise ratio of observed emissions.

$$\text{snr} = (J_{xx} + J_{yy})/J_{zz} \quad (49)$$

In the principal axis system of a wave, the signal to noise ratio is given by

In this coordinate system, the rotating wave field will be contained in the x-y plane.

The only signal measured along the z-axis will be due to incoherent noise.

4.2 Eigenvalue Ratio Test for Planar Waves

This method is applicable only to single plane waves. Therefore, some test of the planarity of the signal must be applied. One method to test for the presence of a single plane wave uses the eigenvalues of the complex spectral matrix [Storey et al., 1991]. The eigenvalues of the spectral matrix are found and the ratio of the largest eigenvalue, λ_1 , to the sum of the eigenvalues is calculated,

$$R_{\lambda} = \lambda_1 / (\lambda_1 + \lambda_2 + \lambda_3) \quad . \quad (50)$$

When one eigenvalue is much larger than the other two, R_{λ} approaches 1 and indicates the presence of a single plane wave. If all three eigenvalues are of the same order R_{λ} approaches 1/3 indicating the presence of two or more plane waves or a noise signal [Storey et al., 1991]. Because the method employed here to calculate the wave normal vector works only for single plane waves, and we are only interested in analyzing coherent plane wave signals, the coherence and the eigenvalue ratio are used to determine when to plot the results. The coherence and eigenvalue ratio limits were chosen by examining whistlers and Omega signals such as those shown in Figure 4. These emissions are coherent and should therefore satisfy the C_{xy} and R_{λ} criteria. Other signals present at the same time that do not satisfy the C_{xy} and R_{λ} criteria and should not be plotted. The vector orientation angles calculated for the uncorrelated signals are randomly distributed over the range of possible angles. When the results for the uncorrelated signals are plotted, they randomly sample the color bar and create a background of randomly colored pixels. When this occurs it is difficult or impossible to distinguish the coherent, planar emissions from the uncorrelated signals. When the criteria were set too high, the whistlers and Omega signals, which are known to be coherent, single-plane waves, were not be plotted. Coherences less than 0.85 allowed too much incoherent signal to be plotted while eigenvalue ratios greater than 0.9 removed too many sufficiently planar emissions. Therefore, coherent signals are assumed to be present when C_{xy}

≥ 0.85 and a single plane wave is assumed to be present when $R_\lambda \geq 0.9$ because these values work well for the whistlers and Omega signals that are known to be coherent, planar waves. These criteria are valid when 8 frequency bins are averaged in the spectral analysis. Wave normal orientation is plotted when these criteria are satisfied.

4.3 Poynting Vector Calculation

As discussed in Chapter 3, if only the wave magnetic field signals are used to determine the wave normal vector, the orientation has an ambiguity of 180° . If two electric field components are measured, the third component can be estimated using Maxwell's equations and models of the local plasma properties. This procedure is limited by how well the plasma properties (such as electron density) are estimated. In the present analysis, the Poynting vector is calculated to resolve this ambiguity. Because the HFWF measures simultaneous waveforms of three orthogonal components of the electric field, the Poynting vector can be calculated directly. No assumptions are required to determine the full wave electric vector. The average Poynting vector is calculated using

$$\langle \vec{S} \rangle = \frac{1}{2\mu_0} \text{Re} \{ \vec{E} \times \vec{B}^* \} \quad (51)$$

at the same frequency and time resolution at which the wave normal vector is calculated. For whistler-mode waves $\hat{k} \cdot \vec{S} > 0$ or, alternatively, the components

of \hat{k} and \vec{S} that are parallel to the local static magnetic field should have the same sign. If $\hat{k} \cdot \vec{S} < 0$, the calculated \hat{k} is rotated by 180° , i.e., $\hat{k} \Rightarrow -\hat{k}$.

The wave normal and Poynting vector are then transformed to a spacecraft-centered coordinate system in which the z axis is parallel to the local static geomagnetic field, \vec{B}_0 . The x-axis is chosen such that the position vector \vec{R} from the Earth to the spacecraft is contained in the x-z plane. The y-axis completes the right-handed system and points eastward. The x- and z-axes are contained in the north-south plane. The orientations of \hat{k} and \vec{S} in this coordinate system are shown in Figure 6. The angle between \hat{k} and \vec{B}_0 , θ , is the wave normal angle. The azimuthal angle ϕ is measured counterclockwise from the x-axis in the x-y plane. The angle between \vec{S} and \vec{B}_0 is denoted by θ_s , while the azimuthal angle of the Poynting vector, ϕ_s , is defined in the same way as ϕ .

Results of the wave normal calculations are shown in Figure 7. The top panel, labeled E', contains the sum of the electric power spectra measured in the fixed (despun) payload coordinate system. The second panel contains the sum of the magnetic power spectra in the same coordinate system and is labeled B'. The wave normal angle θ is plotted in the third panel. The color bar denotes angular values ranging from 0° to 180° . The fourth panel contains the spectrograms of the azimuth angle θ of the wave normal vector. Angular values ranging from 0° to 360° are indicated by the color bar. Spectrograms of the coherence C_{xy} of the wave magnetic signal in the principal axis system of the wave are plotted in the fifth panel. The color bar indicates the magnitude of C_{xy} that ranges from approximately

0.3 to 1.0. The sixth panel shows the polarization of the wave. Right-hand-polarized (RHP) waves are shown in red, while left-hand-polarized (LHP) waves are shown in green. The frequency and time scales used in these plots are the same as in Figure 4. Figure 8 shows the results of the Poynting vector calculations. The top panel, labeled $|S|$, contains spectrograms of the magnitude of the Poynting vector in $\text{W m}^{-2} \text{Hz}^{-1}$. The second panel shows calculated values of the polar angle of the Poynting vector, θ_s , which ranges from 0° to 180° , indicated by color. The azimuthal angle of the Poynting vector, ϕ_s , is plotted in the third panel and ranges from 0° to 360° . The eigenvalue ratio, R_λ , which ranges from 0.3 to 1.0, is plotted in the fourth panel, and the fifth panel contains the magnetic wave coherence, as described for the wave normal plot. The behavior of the wave coherence and the eigenvalue ratio are similar, which implies that they are compatible for use as criteria for plotting the vector orientations. The sixth panel contains the direction of the component of the Poynting vector along the geomagnetic field, $S_z = \vec{S} \cdot \hat{B}_0$. $\vec{S} \cdot \hat{B}_0 > 0$ is plotted as red. $\vec{S} \cdot \hat{B}_0 < 0$ is plotted as green. The wave normal vector and Poynting vector orientations, polarizations, and direction of S_z are plotted only when $C_{xy} \geq 0.85$ and $R_\lambda \geq 0.9$.

It is sometimes difficult to see the detailed variation in the vector orientations plotted using color bars. The wave normal and Poynting vector orientations for one Omega signal are plotted in order to illustrate the detailed behavior of the angles. Figure 9 shows the wave normal angle and wave normal azimuth angle for the Omega signal at 13.1 kHz observed in snapshot 6 of Figure 7. The top panel is the

wave normal angle and the bottom panel shows the azimuth angle of the wave normal vector. The time scale is in seconds from the start of the snapshot. The start time of the sixth snapshot is 09:12:42.492 UT. The wave normal angles range from 125° to 140° while the azimuth angles remain within 20° of the meridian plane. The orientation of the Poynting vector for the same time is shown in Figure 10. The angle between the Poynting vector and the geomagnetic field is shown in the top panel and the azimuth angle is shown in the bottom panel. The angle between the Poynting vector and the geomagnetic field ranges from 160° to 180° . The azimuth angle usually remains between approximately 330° and 360° . The azimuth angle deviates significantly from the meridian plane twice, once at 0.186 seconds after the start of the snapshot and again at 0.358 seconds after the start of the snapshot. These deviations are caused by the affect of the broadband, incoherent wave called plasmaspheric hiss. The electric component of the hiss is observed at frequencies as high as 13 kHz at the times when the Poynting vector azimuth angle deviates from the meridian plane. The accuracy of the calculated vector orientations of a coherent signal is reduced when an uncorrelated signal is also present. This effect is described in section 5.6.1.

CHAPTER V. VECTOR DIRECTION VERIFICATION AND ERROR ANALYSIS

When calculating auto- and cross-power spectra, some care must be taken in order to minimize the bias and variance of the calculated spectral estimates [Brigham, 1988]. Time series data tapering and smoothing of spectral components are used to reduce these effects. Once the data has been transformed into the frequency domain, corrections due to the phase and amplitude characteristics of the sensors and receiver electronics must also be applied to the data to insure correct calculation of the wave normal and Poynting vectors. This chapter begins with a description of the spectral analysis of the study and the frequency-dependent calibrations. The overall direction of the vector calculations are verified using pre-launch test data, then by using magnetospheric VLF emissions with known propagation characteristics. The calculated vector directions are shown to be consistent with a ray tracing simulation of a VLF wave generated in the northern hemisphere.

5.1 Spectral Analysis

As previously stated, the HFWR in high-rate mode produces waveform snapshots of 31,816 samples with sample spacing of $14 \mu\text{s}$. This analysis divides

the data into subintervals of 2048 points with a 50% overlap of the subintervals to give a time resolution of 0.014 seconds. Using subintervals of the data allows the evolution of the spectra to be observed, but also increases the likelihood that the time series being Fourier analyzed is stationary, a condition for meaningful spectral analysis. For a stationary data set, the power spectrum remains constant in time. During periods of rapid wave growth, the time series may become nonstationary. In this case, the spectral analysis will not give an accurate frequency domain representation of the time series. Before performing the fast Fourier transform on the data in each subinterval, the mean value of the signal during the subinterval is subtracted from the time series. This effectively removes the zero-frequency (or DC) term from the power spectrum and reduces the leakage of low-frequency signal power to higher frequencies. Power spectra are defined for infinitely long data sets, but the data set being analyzed is, of course, finite. A rectangular data window causes real spectral features to have side lobes. To reduce power leakage into side lobes, the time series is multiplied by a window function that gradually tapers the data set to zero at the beginning and end. There are many choices of data windows [Brigham, 1988], including the Hanning window and 10% cosine edge weighting, both of which were tried for the present analysis. The Hanning window produced greater variance in the calculated wave normal angles than did the 10% cosine edge weighting. For that reason the cosine edge weighting is used. The edge weighting can also help reduce aliasing of the power spectrum due to signals outside the FFT frequency range, although high-pass filtering would be more effective. No digital

filtering is performed here because the emissions analyzed generally occur at frequencies higher than the low frequencies that suffer from aliasing. The HFWR has high-frequency roll-off filters above approximately 25 kHz that remove signals above that frequency. Once the data has been tapered, an FFT is performed on the time series from each of the six sensors during a given subinterval. Once the signals have been transformed to the frequency domain, the frequency dependent amplitude and phase corrections are applied. These are described in section 2.3. The three magnetic component frequency series are used to calculate the spectral matrix $J_{ij}(\omega) = \{B_i(\omega) B_j^*(\omega)\}$ and the three electric frequency series are used along with the three magnetic frequency series to calculate the Poynting vector, using equation (51). All of the components of these quantities are either auto- or cross-power spectra of the signals measured by the different sensors. It is well known that the variance of each "raw" spectral estimate is on the order of the magnitude of the estimate itself [Bendat and Piersol, 1986; Brigham, 1988]. Therefore, the spectra should be averaged in order to increase the statistical reliability of each estimate. The spectral averaging used in this analysis is performed in the frequency domain by averaging over several spectral estimates with adjacent frequencies. The frequency-averaging windows are overlapped by 50%.

5.2 Confidence Limits of the Power Spectra

Power spectra can be calculated exactly only for infinitely long data sets. Experimental data sets are finite, and the spectral estimates computed from these

data cannot be known with absolute certainty. The statistical variance of the spectral estimates can be given by a confidence interval. For an 80% confidence interval, a spectral estimate will fall within the range of that interval with a probability of 0.8. The confidence interval of an estimate is computed using equivalent degrees of freedom which are determined from the number of raw estimates contained in the averaged spectral estimates. The confidence factor f_c is the ratio between the upper and lower bounds of the confidence limit and can be approximated by the expression

$$f_c \approx \exp\left[\frac{2.3 b}{10\sqrt{k-1}}\right] \quad (52)$$

where k is the equivalent degrees of freedom, and b is a factor that depends on the desired level of confidence:

	50%	80%	90%	96%	98%
b	8	16	20	25	29

[Sentman, 1973]. This approximation is valid for $k \geq 4$. The confidence factor can be used to provide error bars in frequency space for the spectral estimates. This is done by positioning the limits such that the data value lies at the geometric mean of the upper and lower limit. In other words, the upper limit is the spectral estimate multiplied by the square root of the confidence factor and the lower limit is the estimate divided by the square root of the confidence factor. The limits will be centered on the spectral estimate if plotted on a logarithmic scale.

The equivalent degrees of freedom are determined by the number of untapered data points and the number of raw estimates included the averaging process to produce one averaged estimate. The equivalent degrees of freedom are given by :

$$k = 2 p \left(\frac{N - N_T}{N} \right) \quad (53)$$

where N is the number of data points in a subinterval, N_T is the number of tapered points, and p is the number of raw estimates used to calculate the averaged estimate [Sentman, 1974; Priestley, 1981].

The 80% confidence level was chosen as it produces a reasonable measure of the error in the spectral estimates. To calculate the 80% confidence factor $b = 16$ is used. The 10% cosine edge weighting gives $\left(\frac{N - N_T}{N} \right) = 0.8$. Eight FFT estimates in adjacent frequency bins are included in the averaging to determine the elements of the cross-spectral matrix, producing spectral estimates with a bandwidth of 279 Hz. A 50% overlap of these bands gives an analysis frequency resolution of 139.5 Hz. The orientation of the wave normal and Poynting vectors are therefore presented as spectrograms from 156 Hz to 30 kHz with a time resolution of 0.014 seconds and a frequency resolution of 140 Hz. One cross-power spectrum is presented in Figure 11. This spectrum is calculated from the subinterval that starts at 09:12:42.224 UT on September 9, 1996. The peak at 13.1 kHz is the Omega signal that is evident in the sixth snapshot in Figures 4, 7, and 8. The 80%

confidence limit for these estimates is shown, and the Omega signal peak is clearly significant, indicating that the chosen averaging bandwidth is adequate to resolve features of interest. The parameters that determine the temporal and spectral resolutions, subinterval length, subinterval overlap, smoothing width, and smoothing overlap, can all be adjusted to give coarser resolutions to survey the data or to give finer resolutions for detailed study of emissions identified during a survey. The resolutions of this study are adequate to resolve some fine structure, but also work well when using the output to survey the data. However, averaging over fewer frequency bins to increase the resolution is expected to increase the errors in the calculated vector orientations.

5.3 Prelaunch Search Coil Calibration and k-Vector Tests

A series of calibrations of the search coils, magnetometers, and PWI instrument were conducted at the Goddard Space Flight Center Magnetic Test Facility on April 28-29, 1993, by the PWI engineering team. These tests consisted of generating a rotating magnetic field at specified frequencies and recording the signals received by the search coils. The rotating magnetic field was generated using two perpendicular transmitting loops with radii of 9 inches, each containing 10 turns of wire. These are the same transmitting loops used to calibrate the IMP 8 E. M. Fields Experiment [Gurnett and Baumbach, 1973] and a more complete description of the loops can be found there. The transmitting loops were mounted 45 inches away from the search coils. Two different arrangements of the

transmitting loops were used. In the first arrangement, the axis of intersection of the transmitting loops points toward the search coils. This arrangement is shown in Figure 12. In the second arrangement, the axis of intersection is perpendicular to the search coil-transmitting loop line and is parallel to the z search coil. The second arrangement is shown in Figure 13. Four test setups were used. Two used input sine waves to produce a rotating magnetic field with wave normal vector either parallel or perpendicular to the z search coil. The second two arrangements used square wave inputs to generate the rotating magnetic field with wave normal vector either parallel or perpendicular to the z search coil. The alignment accuracies of these test configurations were determined to be $\pm 1^\circ$. The data was received by the HFWR using the 25 kHz analog filter. The data was captured in blocks of 2048 samples with a sampling frequency of 71.43 kHz (14 μ s sample spacing).

5.3.1 UV-Sine and UV-Square Tests

The first experimental setup is shown in Figure 12. For the purposes of this test, a UVZ coordinate system is used. The u-axis points in the direction of the positive B_u search coil. The positive v-axis points in the direction of positive side of the B_v search coil. The positive z-axis points along the positive side of the B_z search coil. The transmitting loops are situated 45 inches from the center of the intersection of the B_u and B_v search coils. The B_u and B_v search coils were aligned to make a 45° angle with the search coils and transmitting loops. This orientation was determined to be accurate to within $\pm 1^\circ$. In one set of tests, Loop A is driven

by a sine wave of a known frequency while loop B is driven by the same signal with a phase lag of 90° . In a second set of tests, the loops are driven by square waves with the same relative phases as described above for the sine wave input signals. The directions of the resulting currents in the loops are labeled as I_A and I_B in Figure 12. This produces a rotating magnetic field at the search coils with a wave normal vector (labeled as \vec{P}) that is predicted to have the orientation $(0.707, -0.707, 0)$ in the coordinate system defined by the search coil axes.

5.3.2 Z-Sine and Z-Square Tests

The second experimental setup is shown in Figure 13. The transmitting loops are again situated 45 inches from the center of the intersection of the search coils. The UVZ coordinate system described in section 5.3.1 is also used in this test. The intersection axis of the loops is now perpendicular to the search coil-transmitting loop line, situated such that the plane containing the B loop is parallel to the B_z search coil and makes a 45° angle with the B_u and B_v search coils. The orientation of the loops with respect to the search coils was determined to be accurate to within $\pm 1^\circ$. As with the UV tests, both sine waves and square waves of known frequencies were used to drive the loops. The signal used to drive loop B again has the same frequency but a 90° phase lag with respect to the signal driving loop A, producing a right-hand polarized wave with polarization vector that points in the $+z$ direction, i.e., a direction of $(0, 0, 1)$ in the coordinate system defined by the search coil axes.

Sine- and square-wave input signals at many frequencies in the receiving range of the HFWR were used to test the search coils in both experimental configurations. The data collected at the test was input into the present version of the Means method using no frequency averaging and using the first 2048 data samples collected in each case. The resulting wave normal angles measured with respect to the u-axis are compared to those calculated at the time of the tests. These results are shown in Table 4.

Sine and square wave inputs at many frequencies from 100 Hz to 30 kHz were used to test the search coils in both experimental configurations. Four of the UV-sine tests were chosen to estimate the error in wave normal angle determination of the present analysis. The wave normal was predicted to have an orientation $(0.707, -0.707, 0)$. The wave normal vector is then expected to be oriented -45° from the positive u-axis. A 2048-sample block of test data are input into the present analysis. No frequency averaging was used for these tests. The resulting angles θ between the wave normal vector and the u-axis at the Fourier frequency nearest the driver frequency are shown in Table 4. The difference between the expected angle, -45° , and the computed angle, $\Delta\theta = (-45^\circ - \theta)$ is also listed. The magnitude of the largest deviation from the expected angle is approximately 2° . Because the alignment of the search coils is accurate to only $\pm 1^\circ$, a reasonable estimate of the error in calculation of the wave normal angle (derived from these tests) would be $\pm 4^\circ$.

5.4 Verification of Poynting Vector Direction Using Prelaunch Test Data

During the GSFC Magnetic Field Test Facility tests described above, the HFWR $E_u +$ and $E_v +$ inputs were driven using the same generated signal used to drive the A transmitting loop. By using the rotating magnetic field measurements made by the three search coils and one of the electric signals, one component of $\vec{S} = \vec{E} \times \vec{H}$ can be computed. The direction of this component is checked against the expected direction in order to verify the correct operation of the analysis program. There was a problem with the test setup that affected the phase measurements of the electric signals, especially at higher frequencies, so a data set with input signal frequency less than 500 Hz was chosen for this test. This phase measurement problem was due to the test setup and is not present in measurements taken in flight.

To test that $\vec{E} \times \vec{H}$ is being correctly calculated by the analysis code, we use the signals measured by the three search coils and the signal input into the $E_u +$ channel. No signal was connected to the E_z input. The signal input into the $E_v +$ channel was the same signal input to the $E_u +$ channel. This does not correspond to the electric signal of a real polarized wave so the signal input to $E_v +$ will be ignored. Therefore $E_v = 0$ and $E_z = 0$ for this test. The S_z component will be calculated using B_u , B_v , B_z , and E_u . The signal generator produces a sinusoidal voltage to drive the E_u input, but the electric field is given by as $\vec{E} = -\vec{\nabla}V$. Because the electric antennas were not connected to the waveform receiver during

these tests, an effective antennal length, L_{eff} , of 1 meter is used. Therefore the electric field will be approximated as $E_u = -V_A / L_{\text{eff}}$, where V_A is the input voltage fed to the E_u input and $L_{\text{eff}} = 1$ m. This imposes no restriction because the purpose of the test is to verify only the direction of S_z . The test case selected was a Z-sine test (described in the previous section), so the signal measured by the B_z search coil should also be zero except for background noise.

The components of $\vec{S} = \vec{E} \times \vec{H} \propto \vec{E} \times \vec{B}$ are then

$$S_u \propto (E_v B_z - E_z B_v) = 0 \cdot 0 - 0 \cdot B_v = 0 \quad (54a)$$

$$S_v \propto (E_z B_u - E_u B_z) = 0 \cdot B_u - 0 \cdot 0 = 0 \quad (54b)$$

$$S_z \propto (E_u B_v - E_v B_u) = (E_u B_v - 0 \cdot B_u) = E_u B_v \quad (54c)$$

If the analysis program is calculating the vector product correctly, the S_z component should be positive. Test results from one Z-sine test conducted with an input signal frequency of 200 Hz were chosen to test the analysis program. This data set contained 6916 samples so 5 subintervals of 2048 points with a 50% overlap could be used. The Poynting vector was calculated in these five subintervals first using no spectral smoothing, then by averaging over four adjacent frequency bins.

In all cases, the z-component of \vec{S} is positive. Thus, it is concluded that the analysis code calculates $\vec{S} = \vec{E} \times \vec{H}$ with the correct sign (in S_z).

5.5 Inflight Verification of Propagation Directions

The ground test data has shown, for some special cases of sinusoidal waves, that the wave normal vector is calculated correctly and gives results that are very close to the expected propagation directions. Since there are many processing steps in the overall signal path from the spacecraft to the displayed results, it is desirable and necessary to test the calculations using data measured by the instrument while in flight. Consistent calculation of \hat{k} and \vec{S} also verifies correct orientation of the sensors on the spacecraft and the calibration of the sensors. Wave propagation vector orientations can be checked using lightning-induced VLF whistlers and signals generated by the ground-based Omega transmitting network. Whistlers are identified by their distinctive curved shape. Higher frequency signals reach the spacecraft first, and the frequency decreases with time. The Omega signals are the narrowband emissions at 11 and 13 kHz. Because their frequency is constant, they appear as horizontal lines on the spectrograms. Both of these types of signals are observed in the September 11, 1996 period shown in the spectrogram of Figure 4. Finally, the propagation characteristics observed during this period are compared to the results of a ray tracing simulation of a nonducted VLF emission to provide further support of the \hat{k} and \vec{S} computations.

5.5.1 Whistlers

Whistlers are observed in the second through the fifth snapshots in Figures 4, 7, and 8 with the strongest whistlers appearing in the fourth snapshot. The strongest whistlers meet the criteria for coherent, single plane waves. The wave normal angles of the whistlers are between 130° to 140° and the azimuthal angles are between about 0° to 20° . The polar angle of the Poynting vector is between 160° and 180° while the azimuthal angle of the Poynting vector is more variable but generally has values greater than 300° . The wave normal angle and polar angle of the Poynting vector indicate that these whistlers are propagating with field-aligned components of \hat{k} and \vec{S} antiparallel to \vec{B}_0 , i.e., the whistlers are propagating southward. This southward propagation is consistent with generation of the whistlers by lightning in the northern hemisphere. Furthermore, the Poynting vectors of these whistlers stay within 19° of the geomagnetic field line as expected for propagation of whistler-mode emissions with frequencies much less than f_{ce} [Storey, 1953; Helliwell et al., 1965; Carpenter and Orville, 1989].

Because the whistlers observed at the spacecraft are consistent with a source in the northern hemisphere, we attempt to find lightning in the northern hemisphere near the location of the endpoint of the magnetic field line that intersects the spacecraft. Because the Poynting flux remains within 19° of the static geomagnetic field line, the wave propagation path stays close to the magnetic field line. It is therefore assumed that the wave emerges from the ionosphere near the location (at the base of the ionosphere) of the "footprint" of the geomagnetic field line that

intersects the spacecraft at the time of wave observation. The location at the base of the ionosphere of the northern hemisphere footprint of the magnetic field line that intersects the Polar position from 09:00 UT to 09:15 UT on September 11, 1996, has been found using the Spacecraft Situation Center software available through a World Wide Web interface. This tool is provided and maintained by the NASA Goddard Space Flight Center Space Physics Data Facility (SPDF) and the National Space Science Data Center (NSSDC). The trace of the field line footprint is shown in Figure 14 on a map of North America. The footprint is observed to move northwest over the Midwest region of the United States of America. The location of the footprint is given at 3-minute intervals in UT in Table 5. We then need to determine if lightning that could generate the observed whistlers occurred in North America.

The U.S. National Lightning Detection Network (NLDN), operated by Global Atmospheric, Inc. (GAI), observes and records cloud-to-ground lightning strike data, which is available through the Marshall Space Flight Center's Global Hydrology Research Center (GHRC) and associated website. This network can detect up to 80% - 90% of cloud-to-ground lightning occurring in the United States with location accuracy up to 500 m. Figure 15 displays NLDN-observed lightning strokes in the continental U.S. from 09:00 UTC (Coordinated Universal Time) to 09:15 UTC. Lightning occurs off the coast of Florida and up the eastern seacoast, in the Southwest (Arizona), and over Nebraska and South Dakota. The lightning observed in Nebraska seems almost certain to be the source of the observed

whistlers, since the field line footprint trace passes almost directly through this region at the same time. To make a better comparison of the lightning stroke location with field line footprint location, the time and location of the NLDN data from 09:12:15 UTC to 09:12:36 UTC on September 11, 1996, are listed in Table 6. The location of lightning strokes are given in geographic latitude and longitude, like the field line footprint locations in Table 5. Signal strength (in kiloamperes) and lightning strike multiplicity (i.e., the number of individual lightning strokes resolved at a particular location during the same second) are also included. At least three or four distinct whistlers can be seen in the fourth snapshot in Figures 4, 7, and 8. These data were recorded from 09:12:24.092 UT to 09:12:24.542 UT. Four lightning strokes were observed by NLDN during the one-second period from 09:12:24 UTC - 09:12:25 UTC in Arizona at 31.97°N , 106.83°W . The footprint of the field line that intersects the Polar orbit at 09:12 UT is located at 40.31°N , 98.59°W . These two locations are separated by about 1300 km. This by no means rules out these lightning strokes as the source of the observed whistlers, as it has been shown that lightning can excite ducted whistler paths whose ionospheric endpoints are as much as 2500 km from the lightning source location [Carpenter and Orville, 1989]. Because the Earth and the base of the ionosphere are conducting surfaces for VLF waves, they form a waveguide for these signals. VLF signals generated by lightning can propagate thousands of kilometers in the Earth-ionosphere waveguide [Burgess, 1993]. The signal produced by the lightning in Arizona could very likely propagate to the location of the footprint and enter the ionosphere there.

It is also likely that intra-cloud lightning at a location closer to the magnetic field endpoint location could be the source of the observed whistlers. Intra-cloud lightning is not detected by the NLDN but occurs more frequently than cloud-to-ground lightning [U. Inan, personal communication, 1998]. It is not possible to directly correlate each whistler with an individual lightning stroke since the whistlers are separated by a few tenths of a second while the lightning data have a resolution of one second. The observation of lightning in the U.S. at the same time that whistlers are observed by Polar provides strong evidence that the whistlers are generated by this lightning in the northern hemisphere. Additionally, the southern footprint of the magnetic field line that intersects the Polar orbit at 09:12:00 UT is located at the geographic coordinates 58.24°S , 124.15°W . This location is over the South Pacific Ocean during spring in the southern hemisphere, and lightning-producing storms are not expected at such high latitudes and over the ocean [Golde, 1977].

5.5.2 Omega Signals

Another signal that can be used to verify the calculated wave propagation characteristics are the narrowband emissions at approximately 11 kHz and 13 kHz. These signals are generated by a ground-based Omega transmitter. Omega signals are easily observed in the first, third, fifth and sixth snapshots in the magnetic spectra in Figure 4. The Omega signals are narrowband emissions and appear as horizontal lines on the spectrogram. The Omega network used VLF radio signals

between 10 and 14 kHz for both commercial and military maritime and aeronautical navigation [Swanson, 1983].

The Omega signal at 13.1 kHz in the fifth and sixth snapshots shows a high coherence and eigenvalue ratio so it is assumed to be a single, coherent plane wave for which the vector orientations are plotted. The wave normal angles range from 125° to 140° and azimuths of \hat{k} are nearly 0° . The wave normal angles and azimuth angles of \hat{k} for the 13.1 kHz Omega signal in the sixth snapshot are shown in Figure 9 as a function of time. The angle between the Poynting vector and the magnetic field ranges from about 160° to 180° , while the azimuth of the Poynting vector is more variable than the azimuth of \hat{k} , often ranging from 330° to 360° . The Poynting vector orientation as a function of time for the 13.1 kHz Omega signal in the sixth snapshot is shown in Figure 10. The azimuth angle of the Poynting vector occasionally reaches angles that are almost perpendicular to the meridian plane. The Poynting vector azimuth is approximately 166° at 0.186 seconds after the start of the sixth snapshot, for example (see Figure 10). The increased variability of these angles is due to the effect of the incoherent plasmaspheric hiss that appears on the electric spectrogram of Figure 7 below 13 kHz. The addition of the incoherent hiss signal with the coherent Omega signal reduces the signal to noise ratio and reduces the accuracy of the calculated angles. This effect is described in section 5.6.1. The polar angle of \vec{S} is seen to remain mostly within 19° of the local geomagnetic field. This is consistent for wave propagation in the whistler mode for frequencies much less than the local electron cyclotron frequency. The wave normal

angles are consistent with propagation of a signal generated by a station located in the northern hemisphere that propagates along a geomagnetic field line after propagating through the ionosphere.

As with the whistlers, we want to locate the source region. The Omega network was comprised of eight transmitters located worldwide. In addition to transmitting pulses at 10.2 kHz, 11.05 kHz, 11.33 kHz, and 13.6 kHz, each site transmits a pulse at a unique frequency, allowing identification of a transmitter by that frequency. The Omega signals observed in the fifth and sixth snapshots occur at 13.1 kHz. This is the unique frequency for the Omega transmitter located in North Dakota, U.S.A. This Omega transmitter is located at geographic coordinates 46.35°N , 98.48°W . It is perhaps better to use the Omega signal than the whistler signals to verify the wave propagation vector directions since the source location of these signals is clearly identified. The location of the Omega transmitter in North Dakota is not at the location of the field line footprint. However, as stated in the previous section it is not unusual for a VLF emission to travel hundreds or thousands of kilometers before propagating upward out of the ionosphere and into the magnetosphere.

It is also desirable to use the Omega signals to check the calculated direction of propagation because these signals are narrowband emissions. The propagation vector calculations at the frequency of the emission will contain minimal contributions from signals at nearby frequencies due to side-lobe leakage of the Fourier analysis or mixing due to the spectral smoothing. The calculated wave

normal and Poynting angles do have significant variability, however. This could be caused by changes in the propagation characteristics of the ionosphere or possibly due to the influence of the natural incoherent emission, called plasmaspheric hiss, observed at frequencies near the Omega signal, especially at 10 kHz in the first snapshot. The variability of the orientations may be caused by a beating effect due to interaction of the primary wave with a wave which has been reflected off the ionosphere and Doppler shifted due to the motion of the spacecraft [D. Lauben, personal communication, 1997]. It is also possible that the plasmaspheric hiss, seen at slightly lower frequencies during the Omega signals, may be strong enough at the frequency of the Omega signal, to influence the calculation of the direction of propagation of the wave while being weak enough to not violate the single plane wave criteria.

The wave normal and Poynting vectors of these emissions are then consistent with propagation from lightning strikes in North America or the Omega transmitter in North Dakota and propagation along the magnetic field line to the spacecraft location.

5.5.3 Comparison with Ray Tracing Results

It seems almost certain that both the whistlers and the Omega signals shown in Figures 4, 7, and 8 have their sources in the northern hemisphere near the location of the magnetic field line footprint. As a further check of the validity of wave normal and Poynting vector angle calculations, the calculated wave normal

directions are compared to the results of a ray tracing analysis. This analysis will verify the evolution of the wave normal angle of \hat{k} as a VLF wave propagates from the ionosphere to the location of the spacecraft. The data show that at the spacecraft position the wave normal angle is rather oblique, $\theta \sim 130^\circ - 140^\circ$, the Poynting vector angle remains within 19° of \vec{B}_0 and both the azimuthal angles of \hat{k} and \vec{S} remain within $\sim 20^\circ$ of the meridian plane and are oriented outward from Earth. The results of a ray tracing simulation of a 15 kHz wave launched from 45° magnetic latitude is shown in Figure 16 [after Helliwell, 1969]. The ray path, shown by the solid line, is typical for a non-ducted whistler-mode emission, similar to the whistlers and Omega signals being observed here. The wave normal direction is shown by arrows along the ray path, and dipole magnetic field lines are shown as dashed lines. The wave normal is nearly vertical when the wave is launched in the ionosphere. The wave normal angle becomes larger as the wave propagates, reaching approximately 130° near the magnetic equator.

If a wave generated near the Earth, like an Omega signal or lightning-generated whistler, propagates through the ionosphere it will emerge from the ionosphere perpendicular to the ionospheric surface. This can be shown using Snell's law with the index of refraction in the ionosphere much larger than the index of refraction in the atmosphere where the wave is generated. As a result, the wave normal angle will be small. The ray path of a wave launched from the vicinity of the whistler and Omega source locations remains near the geomagnetic field line, while the wave normal angle increases as the wave propagates away from the

source. The measured wave normal and Poynting vector orientations are consistent with these predictions.

5.6 Estimation of Errors

For the results of any experiment to be useful and meaningful some measure of the precision and accuracy of the results must be included with those results. This is done by providing the estimated error of the results. Errors can be either systematic or random. Random errors are always present in experiments and are due, for example, to varying environmental conditions or inconsistent measurement practices. As the definition states, these errors are caused by random effects and are usually found by repeating the experiment many times. Systematic errors arise due to characteristics of the experimental apparatus or to the measurement procedure and do not become apparent by making repeated measurements. Both types of errors are estimated for the present analysis by using computer-generated time series with known changes in amplitudes, relative phases and level of noise.

5.6.1 Random Error

One measure of a source of random error has already been presented earlier in this chapter as the confidence limits of the cross-power spectral estimates. The 80% confidence limit was shown for one cross-power spectrum to indicate that the smoothing being used is sufficient to resolve real spectral features from the background statistical noise of the spectral analysis. Similarly to calculating this

confidence limit, the variances of the cross-spectral estimates and the covariances between cross-spectral estimates could be estimated [Bendat and Piersol, 1986; Priestley, 1981] and then used in an error propagation exercise. As this method can be prone to mistakes when deriving analytical expressions for complicated derivatives. The error propagation calculation was tried, but was too complicated and prone to errors to justify its use in this study. Instead, computer-generated signals are used to estimate the errors in the calculated angles. This provides a measure of the sensitivity of the vector directions to the measurement errors of the electric and magnetic signals. Knowing the errors in measurement of the wave electric and magnetic signals then allows calculation of the errors in the vector directions.

The major contribution to the random error of the wave vector calculations is expected to come from signals produced by natural incoherent plasma waves other than the type of wave being studied. A good example would be plasmaspheric hiss, which often occurs at the same time and in the same frequency range as whistlers and Omega signals. Such incoherent signals should appear as isotropic noise signals in the frequency range where they are observed. To simulate background noise, a sinusoidal wave was generated at 13.13 kHz with a wave normal vector $(0, 0, 1)$ to which random data with adjustable amplitude was added using a random number generator. The level of noise is quantified by the signal to noise ratio, snr , defined in equation (49). In this case the wave perturbation vector is entirely in the x-y plane, and the only signal measured along the z-direction is the noise signal.

The Omega signals and whistlers studied previously are used to provide signal to noise ratios that might be expected. Signals with similar snr will then be simulated. The Omega signals studied previously have high signal to noise ratios since the wave power is concentrated in a narrow frequency band. The signal to noise ratio of these emissions are usually about 200 and greater. The whistlers have much lower signal to noise ratios, usually between 20 and 50. Emissions with lower snr generally do not meet the coherence or planarity criteria. The simulated data verify that signals with signal to noise ratios of approximately 20 are at the limit of the coherence and eigenvalue ratio criteria. The results of several runs are presented in Table 7. It can be seen that as the signal to noise ratio decreases, the wave normal angle and Poynting vector angles vary from the real angles, and the coherence and eigenvalue ratio decrease. This is observed in the data when a coherent emission such as a whistler or Omega signal are present with a background of hiss. If the hiss is not too strong, the coherent signal is effectively separated from the incoherent background emission, although the error in the calculated vector directions are expected to be higher than without the presence of the background signal. A likely example of this situation occurs for the Omega signal observed in the first snapshot of Figures 4, 7, and 8 where the intensity of the plasmaspheric hiss is almost as strong as that of the Omega signal.

5.6.2 Systematic Error

An expected source of systematic error is introduced by gain and phase calibration errors for the various sensors. It is assumed that phase and gain corrections applied to signals measured along the z-axis are correct since these measurements are not affected by the satellite rotation. As described in the calibration section, the calibrations of the signals measured in the spin-plane of the spacecraft, i.e. along the spacecraft u- and v-axes, are adjusted approximately since the despun signals being calibrated are mixtures of the signals measured along the u- and v-axes. Applying the calibrations of a sensor in the u-v coordinate system to a mixed signal measured in the FP coordinate system will correct for the overall characteristics of the sensor, but will also introduce an error in phase related to the phase difference in the calibrations between the u and v sensors. Similarly, the gain corrections will introduce an error related to the ratio of the gain correction factors of the u and v sensors.

To investigate the errors produced in the final vector orientation angles, signals with phase shifts or amplitude changes similar to the measurement errors will be simulated. The amplitudes measured by the triaxial search coil magnetometer are accurate to within 5.9% of the measured values [G. Hospodarsky, personal communication, 1998]. The error in the phase of the signals measured by the search coils is determined to be 5° . The wave normal vector components depend on the relative phases between signals measured along different axes. For this reason, relative phase shifts between different signals is expected to produce the largest error

in the vector orientations. Simulated data was created with wave normal and Poynting vectors parallel to $(0, 0, 1)$ and $(.707, .707, 1)$. To change the amplitude of a signal, the original sine wave amplitude of the signal along the x-axis was multiplied by a factor δE_{x0} for the electric signal, or δB_{x0} for the magnetic signal. To introduce a phase shift between the x- and y-axes the phase of the electric or magnetic signal measured along the x-axis were changed by an amount $\delta\phi_{EU}$ or $\delta\phi_{BU}$, respectively. The results of these tests are described below. Finally, a combination of the relative phase differences on the electric and magnetic fields and the relative amplitude error between the electric signals were performed for waves at the frequencies where each of these relative errors was a maximum. The results of these tests will be used to provide an estimate of the errors in the calculated vector orientations.

It was found for the signal with wave normal and Poynting vector orientation parallel to the z-axis that any changes in phase or amplitude of the signals along the x- or y-axis produced no change in the wave normal or Poynting vector orientations. Therefore, when the plane of polarization of the wave (the plane perpendicular to the wave normal) is contained in the x-y plane of the spacecraft, the amplitude and phase errors in the calibrations will have no effect on the determination of the wave normal angle. In general the wave normal and Poynting vectors are not parallel, and the calibrations will introduce an error into whichever vector is not perpendicular to the spin plane of the spacecraft.

In the next test phase and amplitude changes were introduced to signals with wave normal and Poynting vector orientations parallel to $(.707, .707, 0)$, i.e. $\theta = \theta_s = 45^\circ$, $\phi = \phi_s = 0^\circ$, where θ and θ_s are measured in the x-y plane and ϕ and ϕ_s are angles measured from y-axis in the y-z plane. This simulated data produces signals analogous to the prelaunch search coil tests using signals with wave normal vector in the u-v plane of the sensors. The results of this test are shown in Table 8.

It is seen that a phase shift of 5° in one electric measurement introduces an error of 0.041° to the Poynting vector angle calculated in the x-y plane and an error of 1.768° to the Poynting vector angle perpendicular to the x-y plane. The relative phase shift in the electric measurements does not affect the wave normal orientation since only magnetic signals are used in that calculation. A 5° relative shift between the magnetic signals produces errors in the calculated orientations of both the wave normal and Poynting vector. The error in θ is 0.055° , while the error in ϕ is 3.454° . The errors introduced to θ_s and ϕ_s are the same as for the 5° relative phase shift between the electric signals.

The amplitude of one magnetic and one electric signal was increased by 10% to investigate the errors introduced by an error in gain correction. The 10% increase in one magnetic signal produced an error of 2.726° in θ , an error of 1.397° in θ_s , and had no effect on the calculation of ϕ and ϕ_s . The 10% amplitude increase in electric signal produced the same error in θ_s but produced no effect on θ . This increase is somewhat larger than the amplitude measurement error of 5.9%. The

error in angle calculation from this test will be slightly larger than expected for a 5.9% measurement error.

By inspection of the calibration tables for the u and v sensors, the largest relative phase calibration error in magnetic phases is 0.9° at 1 kHz. The largest relative phase calibration error between the u and v electric antennas occurs at 8 kHz. The relative gain and phase errors at these two frequencies were applied to sinusoidal signals to approximate the maximum errors that might be expected due to calibration. The results are shown in Table 9. At 1 kHz the errors are 0.002° in θ , 0.707° in ϕ , 0.328° in θ_s , and 0.657° in ϕ_s . At 8 kHz the errors are 0.107° in θ , 4.962° in ϕ , 0.085° in θ_s , and 0.509° in ϕ_s .

From these results, the largest error found in the angle determinations of these tests occurred for the simulation of the combined calibration errors at 8 kHz. The wave normal azimuth angle was approximately 5° from the expected value. It seems reasonable to conclude that this is the largest error encountered in the orientation calculations. Therefore, the wave normal and Poynting vector angles can be calculated to within $\pm 5^\circ$.

CHAPTER VI. MAGNETOSPHERIC CHORUS SOURCE REGION

Previous studies have used indirect evidence to argue that whistler-mode chorus emissions are generated near the magnetic equator. In this thesis a spatial survey of the Poynting vector computed from three component electric and magnetic field measurements is used to show that chorus is generated very close to the magnetic equator. One surprising result is that there are almost no chorus emissions propagating toward the magnetic equator, such as might be expected from high-latitude magnetospheric reflections. The absence of a reflected component indicates that the chorus is reabsorbed, probably by Landau damping, before returning to the magnetic equatorial plane.

6.1 Previous Studies of Chorus Wave Normal Angle

Whistler-mode chorus is one of the most common very-low-frequency (VLF) emissions observed in the Earth's magnetosphere [Storey, 1953; Allcock, 1957; Helliwell, 1965]. For many years it has been widely believed that chorus is generated near the magnetic equatorial plane [Helliwell, 1969]. However, there are no direct measurements of the source location. In this study, three-component electric and magnetic field measurements from the Plasma Wave Instrument (PWI)

on the Polar spacecraft are used to show that chorus is generated within a few degrees of the magnetic equator.

Chorus usually occurs in the frequency range from a few hundred Hz to a few kHz and is characterized by fine structure that usually consists of rising or falling tones, and sometimes short impulsive bursts [Burtis and Helliwell, 1969; Dunkel and Helliwell, 1969; Burton and Holzer, 1974; Cornilleau-Wehrlin et al., 1978; Hayakawa et al., 1990; Lauben et al., 1998, and references therein]. Near the magnetic equator chorus often occurs in two bands separated by a gap at one-half the electron cyclotron frequency ($f_c = 28B$ Hz, where B is the magnetic field in nT [Burtis and Helliwell, 1976; Goldstein and Tsurutani, 1984]). Away from the magnetic equator the chorus emission frequency is closely correlated with the equatorial cyclotron frequency, f_{co} , of the magnetic field line passing through the observing point, and is nearly independent of the local electron cyclotron frequency [Dunkel and Helliwell, 1969; Burtis and Helliwell, 1969]. The correlation with the equatorial cyclotron frequency provides indirect evidence that chorus is generated near the magnetic equator. Tsurutani and Smith [1977] have also shown that chorus is most intense near the magnetic equator, which further supports the view that chorus is generated near the magnetic equator.

Chorus is believed to be generated by a combination of mechanisms. Whistler-mode waves have been shown to grow unstable in the presence of anisotropic electron pitch angle distributions [Kennel and Petschek, 1966]. This is a linear theory of wave growth where the free energy source is provided by the pitch

angle anisotropy. Waves will grow when the anisotropy of the resonant electrons exceeds a critical value given by

$$A_c = \frac{1}{(\omega_c / \omega - 1)} \quad (55)$$

Anisotropic electron pitch angle distributions of energetic electrons (10 - 100 keV) have been observed simultaneously with chorus emissions near the geomagnetic equator by the OGO 5 satellite [Burton, 1976] and the SCATHA satellite [Isenberg et al., 1982]. Waves generated by this anisotropy then interact with energetic electrons through a Doppler-shifted cyclotron resonance. The resonant electrons are phase bunched by the whistler-mode waves. The phase bunched electrons then emit more waves that can cause bunching of more electrons [Helliwell, 1969]. This is a nonlinear process of wave production.

The magnetic equator is shown to be a likely source region by considering the resonance energy for whistler-mode waves propagating parallel to the magnetic field. Using the high density approximation, the resonance energy is given by

$$W_{\text{Res}} = W_c \left(\frac{\omega_c}{\omega} \right) \left(1 - \frac{\omega}{\omega_c} \right)^3 \quad (56)$$

where

$$W_c = \frac{B^2}{2 \mu_0 n_e} \quad (57)$$

is the characteristic energy of the resonant electrons. B is the magnetic field strength, μ_0 is the permeability of free space, and n_e is the electron number density. The largest number of electrons will be in resonance with the wave when the characteristic energy is a minimum, since most electrons in a plasma are found at low energies. The minimum characteristic energy occurs at the geomagnetic equator where B has its minimum value. Hence, the geomagnetic equator is the most likely location for chorus generation. Also, because the magnetic field changes most slowly at the magnetic equator, electrons at resonant velocities $v_{\parallel} = \omega / k_{\parallel}$ remain in resonance for the longest time when near the equator. A diagram used by Helliwell [1969] to show the wave generation region is shown in Figure 17. The magnetosphere in the geomagnetic meridian plane is shown. The generation region is represented as a sheet close to the geomagnetic equator. Several types of waves are shown. Inside the plasmasphere (the shaded region near the Earth), magnetospherically reflected (MR) whistlers are shown. These waves are generated by lightning in the atmosphere and may pass through the equatorial region several times. Waves are also shown that propagate in ducts of enhanced plasma density in the plasmasphere and at the plasmapause. The wave normal vectors of these waves remain very near the magnetic field direction, allowing the wave to propagate into the ionosphere and be observed on the ground. Outside the plasmasphere, nonducted waves such as chorus are shown. These waves are absorbed due to Landau damping before propagation back to the generation region is possible. Inside the plasmasphere, the plasma temperature is cold (~ 1 eV), and there will be

few particles with energies corresponding to the resonance velocity, $v_{\parallel} = \omega / k_{\parallel}$, where Landau damping will occur. The plasma temperature outside the plasmasphere is hotter ($\sim 0.1 - 1$ keV), so there are more particles at the resonance energy. Waves outside the plasmasphere, like chorus, are more likely to be Landau damped before reflection and propagation back to the equator is possible.

Several previous investigators have studied the wave normal distributions of chorus. Using three-axis magnetic field measurements, Burton and Holzer [1974] showed that the wave normal angle, θ , measured relative to the magnetic field, is symmetrically distributed around $\theta = 0^\circ$ for magnetic latitudes, λ_m , near the equator ($0^\circ < \lambda_m < 2.5^\circ$), but is shifted toward larger values of θ at higher latitudes. This latitudinal dependence is consistent with generation near the magnetic equator. However, since only magnetic measurements were used the wave normal direction had a 180° ambiguity [Means, 1972]. Therefore, Burton and Holzer had to assume that the wave was propagating away from the magnetic equator. More recently, Nagano et al. [1996] used five-component wave field measurements (three magnetic and two electric fields) from the Geotail spacecraft to calculate the wave normal direction of chorus. The electric field measurements eliminate the ambiguity in the wave normal direction. For a case studied near the magnetopause, the wave normal directions were shown to be consistent with generation near the magnetic equator, although a few emissions were observed to be propagating toward the equator.

Chorus with frequencies above one-half of the electron cyclotron frequency is found to have wave normal angles closely related to the resonance cone angle, θ_{Res} ,

[Hayakawa et al., 1984]. Muto et al. [1987] and Muto and Hayakawa [1987] have shown that the wave normal angles are very close to θ_{res} near the magnetic equator ($\lambda_m \approx 17^\circ$), but are 15° to 20° less than θ_{res} at higher latitudes ($\lambda_m \approx 26^\circ$). Again, the wave normal determination had a 180° ambiguity because only magnetic measurements were used. Muto and Hayakawa have interpreted this wave normal dependence as indicating that the upper chorus band is generated near the magnetic equator with wave normal angles near the resonance angle.

In this study three-component measurements of electric and magnetic wave fields from the Plasma Wave Instrument (PWI) on the Polar spacecraft are used to compute the wave normal and Poynting vectors of chorus. Since simultaneous three-axis electric and magnetic field measurements are used, the 180° ambiguity in the wave normal direction is eliminated.

6.2 Poynting Vector Direction of Magnetospheric Chorus

A series of frequency-time spectrograms illustrating a chorus event observed on November 25, 1996, is shown in Figure 18. The spectrograms include data from 00:23.06.839 UT to 00:23.53.289 UT ($L \approx 4.5$, $\lambda_m \approx 10^\circ$, and MLT ≈ 09.11 hr). The frequency range of each spectrogram is 0 to 10 kHz. The top two panels show the electric and magnetic power spectra. Intensity is indicated by the color bar to the right of each panel. The wave normal angle, θ , and the azimuth angle, ϕ , of the wave normal vector are shown in the third and fourth panels, respectively. Angles are indicated by the color bars to the right. The fifth panel contains the

wave coherence and the sixth panel shows the polarization. Right-hand polarized waves are red and left-hand polarized waves are green. The Poynting vector orientations for this same time are shown in Figure 19 with the same frequency and time scales. The magnitude of the Poynting vector is shown in the top panel. The second panel shows the polar angle of the Poynting vector, θ_s , and the third panel shows the azimuth angle of Poynting vector. The fourth and fifth panels show the wave coherence and eigenvalue ratio, respectively. The values of these quantities are indicated by the color bars to the right of each panel. The sixth panel shows the sign of the z-component of the Poynting vector ($S_z = \vec{S} \cdot \hat{B}_0$, where \hat{B}_0 is a unit vector parallel to the magnetic field). When S_z is positive the Poynting vector has a component in the $+\hat{B}_0$ direction (i.e., northward at the equator). These emissions are plotted as red. When S_z is negative the Poynting vector has a component in the $-\hat{B}_0$ direction (i.e., southward at the equator). These emissions are plotted as green. This period shows many characteristic features of chorus including a two-banded structure with a gap near $0.5 f_c$ (which is approximately 5 kHz at this time), as well as rising tones. The wave normal angles range from about 40° to 70° for much of the lower frequency ($f < 0.5 f_c$) structured chorus. The wave normal angles for higher frequency ($f > 0.5 f_c$) chorus range from 0° to 40° and are very often less than 20° . For the lower band chorus, the azimuth angles of \hat{k} remain within about 40° of the magnetic meridian plane ($\phi = 0^\circ$). The azimuth angles of the higher frequency chorus show a wide range of values. These wave normal directions are in good agreement with the results of previous wave normal studies

such as [Burton and Holzer, 1974; Goldstein and Tsurutani, 1984]. The angle, θ_s , between the Poynting vector and the magnetic field have values between 0° and 40° for both the upper and the lower band chorus. The values of θ_s are often about 20° or less. Higher values occur most often at about $0.5 f_c$ where mixing of the chorus in the upper and lower bands might affect the orientation. For the lower frequency chorus, the azimuth angle of \vec{S} is between about 180° and 220° , near the meridian plane. At frequencies above $0.5 f_c$, the azimuth of \vec{S} is quite variable. As can be seen, all the chorus emissions in this example are propagating northward (i. e., $\vec{S} \cdot \hat{B}_0 \geq 0$). Since the spacecraft is in the northern hemisphere ($\lambda_m \approx 10^\circ$) the chorus is propagating away from the magnetic equator.

Chorus events lasting from a few minutes to more than an hour are frequently observed in the Polar HFWR data. A SFR spectrogram of a relatively long-lasting chorus event is illustrated in the top panel of Figure 20, which shows the electric field spectral density measured from 1915 UT to 2115 UT on December 14, 1996. The white line is the electron cyclotron frequency. A band of chorus can be seen rising slowly in frequency from about 1918 UT to 2025 UT in the northern hemisphere ($\lambda_m \approx 31^\circ$ to $\lambda_m \approx 3.4^\circ$), and a similar band of shorter duration can be seen decreasing slowly in frequency from about 2045 UT to 2100 UT in the southern hemisphere ($\lambda_m \approx -13^\circ$ to $\lambda_m \approx -23.8^\circ$). The bottom panel of Figure 20 shows the sign of the S_z component of the Poynting vector. These measurements are obtained by averaging S_z over each 0.45-second snapshot, thereby giving a time resolution of 9.2 seconds. The frequency resolution is 140-Hz. The chorus in the

northern hemisphere is seen to be propagating northward ($\vec{S} \cdot \hat{B}_0 \geq 0$), away from the magnetic equator. There is no indication of equatorward propagation. The chorus in the southern hemisphere is seen to be propagating southward ($\vec{S} \cdot \hat{B}_0 \leq 0$), again away from the magnetic equator. Only one brief period occurs where an equatorward propagating emission is observed. This exception occurs at approximately 2026 UT ($\lambda_m \approx 3^\circ$), where a brief narrowband emission is observed shortly after the spacecraft has entered the plasmasphere (the entry into the plasmapause is indicated by the steep rise in the upper hybrid resonance frequency, hence plasma density, at approximately 2020 UT). Although the narrowband emission is observed in the northern hemisphere, it is propagating southward, toward the equator.

In order to see if the results shown in Figure 20 can be generalized, we have examined all of the available Polar PWI data to determine the direction of propagation of chorus. Data from a total of 394 orbits over a time interval from March 28, 1996 to September 16, 1997, were examined. The HFWR operated in the six-channel high-telemetry rate mode for 889.7 hours during that time. During those 889.7 hours 61 chorus events that passed the coherence and plane wave tests were observed and analyzed. The observations were grouped into one-minute time bins and then separated into two categories, northward-propagating ($\vec{S} \cdot \hat{B}_0 > 0$), and southward-propagating ($\vec{S} \cdot \hat{B}_0 < 0$). The orbital paths for these two categories were then plotted in a magnetic meridian plane plot (radial distance versus magnetic latitude). The results are shown in Figure 21. As can be seen in the northern

hemisphere almost all of the chorus emissions are observed to be propagating northward ($\vec{S} \cdot \hat{B}_0 \geq 0$), and in the southern hemisphere almost all of the chorus emissions are observed to be propagating southward ($\vec{S} \cdot \hat{B}_0 \leq 0$). Thus, almost without exception, chorus is observed to be propagating away from the magnetic equator.

6.3 Discussion of Chorus Propagation Characteristics

We have shown that almost without exception chorus observed in the northern magnetic hemisphere propagates northward away from the magnetic equator, and chorus observed in the southern magnetic hemisphere propagates southward away from the magnetic equator. These results provide conclusive evidence that chorus is generated very close to the geomagnetic equator. The transition from northward to southward propagation at the magnetic equator is very abrupt, and there is almost no overlap of the regions of northward and southward propagation. The observations also show that there is essentially no evidence of high-latitude magnetospheric reflections, such as often occurs for lightning-generated whistlers [Smith and Angerami, 1968]. One possible explanation for this was discussed in section 6.1.

The very rapid transition from southward to northward propagation, within just a few degrees of the magnetic equator, implies that the chorus source region is extremely small, probably not more than a few thousand kilometers in north-south extent. The absence of an equatorward-propagating component in the source region

implies that the wave does not start growing to significant amplitudes until after it has crossed the magnetic equator. Since the wave reaches saturation amplitudes within about 3° of the magnetic equator, the growth rates must be very high. The group velocity can be estimated using equation (23). The parameters necessary for this calculation can be found by examination of the SFR spectrogram in Figure 20 at a time when Polar is near the magnetic equator. Chorus is observed near the magnetic equator at about 20:14 UT just before the spacecraft enters the plasmasphere. At this time, Polar is located at a radial distance $R \approx 4 R_E$. The group velocity will be estimated for chorus observed at this location. At this time the electron cyclotron frequency, calculated from MFE data, is $f_c \approx 13.73$ kHz. The upper hybrid frequency, $f_{UH} = (f_p^2 + f_c^2)^{1/2} = f_p$ when $f_p \ll f_c$. Emission at f_{UH} is clearly shown in Figure 20. At 20:14 UT this emission occurs at about 30 kHz. This value is used for f_p . The chorus observed at 20:14 UT has a frequency $f \approx 6$ kHz. Using these values, the group velocity of the chorus is $v_g \approx 7.64 \times 10^4$ km/s. Polar is located at $R \approx 4 R_E$ at this time. The chorus travels approximately 3° before reaching saturation (estimated from Figure 21). At $4 R_E$, 3° corresponds to a distance of approximately 1333.5 km. Chorus propagating at the calculated group velocity will travel this distance in $\Delta t \approx 1.745 \times 10^{-2}$ seconds. It is estimated that the chorus reaches saturation amplitudes after 10 e-foldings, $e^{10} = e^{\gamma \Delta t}$. Solving for γ gives an approximate growth rate of $\gamma \approx 5 \times 10^2 \text{ s}^{-1}$. A range of the value of γ would be different for a different choice of parameters. If, for example, a slightly later time is chosen when the plasma frequency is higher, the

group velocity will be smaller. This leads to a smaller growth rate. It is then estimated that growth rates on the order of 10^2 s^{-1} or higher are required. The almost complete absence of a reflected component indicates that the chorus emissions must eventually encounter strong damping as they propagate to high latitudes. Evidence of strong Landau damping at high latitudes has been given previously by Burton and Holzer [1974] and Goldstein and Tsurutani [1984]. They showed that chorus observed at higher magnetic latitudes has larger wave normal angles than near the equator. The distribution of wave normal angles expected for reflected waves was not observed. They suggested that Landau damping dissipates the wave energy before the wave is reflected back to the magnetic equator. Because there is no evidence of reflection, our observations appear to rule out steady-state generation mechanisms that require multiple passes through the magnetic equatorial plane, such as the mechanism of Kennel and Petschek [1966].

CHAPTER VII. AURORAL HISS PROPAGATION CHARACTERISTICS

Auroral hiss is a broadband whistler-mode emission often seen in low ($R < 1 R_E$) and high altitude auroral regions. Auroral hiss has a funnel-shaped appearance on a frequency-time spectrogram [Gurnett, 1966; Jorgensen, 1968; Gurnett and Frank, 1972; Gurnett et al., 1983] and is observed between a few hundred Hz to several tens of kHz. Both upward and downward propagating auroral hiss is observed. Upward propagating auroral hiss is generated by low energy (100 eV - 10 keV) electrons traveling upward along auroral field lines, and downward propagating auroral hiss is generated by electrons of similar energy traveling downward along the auroral field lines. It is believed that auroral hiss propagates with wave normal angles very near the resonance cone angle where the whistler mode is quasi-electrostatic [Mosier and Gurnett, 1969; Gurnett and Frank, 1972; James, 1976].

Auroral hiss has been observed at low altitudes by many satellites including Alouette 1 [McEwen and Barrington, 1967], OGO 6 [Laaspere et al., 1971], Ariel 3 [Hughes and Kaiser, 1971], and ISIS 1 and 2 [Yoshino et al., 1981; Ondoh, 1990]. At low altitudes, below a few thousand km, auroral hiss is usually propagating downward, although upward propagating emissions called saucers are sometimes observed. High altitude observations of auroral hiss have also been made by several

satellites. At high altitudes, above about ten thousand km, auroral hiss is always propagating upward. Hawkeye 1 observed upward propagating auroral hiss in the dayside polar cusp at distances up to $10 R_E$ [Gurnett and Frank, 1978]. Auroral hiss was also observed by DE 1 at altitudes up to $4.65 R_E$ [Gurnett et al., 1983; Lin et al., 1984; Gurnett and Inan, 1988; Morgan, 1992; Morgan et al., 1994]. Auroral hiss has been observed most recently at high altitudes by the Polar spacecraft, which has an apogee of $9 R_E$ over the north polar region.

Poynting flux measurements of low altitude auroral hiss made by Injun 5 have been used to show at low altitudes that hiss is generally propagating downward, toward the Earth [Mosier and Gurnett, 1969, 1971]. These measurements indicated that the hiss was generated at altitudes above the Injun 5 apogee of 2,500 km. The source of auroral hiss was shown to be located, at altitudes between 5,000 and 10,000 km in the polar ionosphere by Gurnett and Frank [1972]. Lin et al. [1984] showed that the low energy (100 eV - 10 keV) electrons that generate auroral hiss are accelerated in a region between $1.7 R_E$ and $1.9 R_E$.

The correlation of auroral hiss with electron fluxes of energies less than 10 keV was first observed by Gurnett [1966]. This paper also described the characteristic funnel shape of the auroral hiss on frequency-time spectrograms. The correlation between auroral hiss and low energy electron fluxes has also been observed by other satellites including OGO 4 [Hoffman and Laaspere, 1972; Laaspere and Hoffman, 1976], Injun 5 [Mosier and Gurnett, 1972; Gurnett and Frank, 1972], OGO 6 [Laaspere and Johnson, 1973], and ISIS 1 [James, 1973].

Smith [1969] first suggested that whistler-mode waves propagating with wave normal angles close to the resonance cone angle could produce the characteristic funnel shape of the hiss. This behavior was confirmed by ray tracing that reproduced the funnel shape of the hiss spectrum [Mosier and Gurnett, 1969; Gurnett et al., 1983]. Other similar studies have been performed by James [1976] and Lin et al. [1984]. Some representative ray paths are shown qualitatively in Figure 22 [Gurnett et al., 1983]. The bottom right drawing shows the ray paths for a point source on a vertical magnetic field line and the top right drawing shows the shape of the auroral hiss as observed on a frequency-time spectrogram. The index of refraction curves shown in the bottom left of Figure 22 are similar to the one shown in Figure 5. Ray tracing studies show that at low frequency ($f \ll f_c$, $f \ll f_p$) auroral hiss propagates with ray paths that remain close to the magnetic field line. As the frequency of the hiss increases, the ray paths become more oblique with respect to the magnetic field, and diverge more quickly from the magnetic field as they propagate. A satellite passing horizontally through the auroral hiss (shown in the bottom right drawing) will observe higher frequencies first, followed by emissions with gradually decreasing lower cutoff frequencies. The lowest frequency is observed when the spacecraft is closest to the source. The lower cutoff frequency then increases as the spacecraft flies away from the source.

Incoherent Cerenkov radiation from a beam of precipitating electrons was initially believed to be the generation mechanism for auroral hiss [Ellis, 1957; Jorgensen, 1968; Taylor and Shawhan, 1974; Sazhin et al., 1993, and references

therein]. Taylor [1973] showed that the mechanism proposed by Ellis produced power levels two orders of magnitude smaller than observed power spectral densities. A convective beam instability was suggested by Maggs [1976] and further developed by Maggs [1978] and others [Sazhin et al., 1993], but this mechanism is limited by its strong dependence on the geometry of the precipitating electron beam. Beam instabilities occur when there is a peak in the electron velocity distribution near the resonant velocity, $\partial F_0 / \partial v_{\parallel} > 0$. The electron distribution function is F_0 and v_{\parallel} is the velocity parallel to the magnetic field. Resonance occurs when $v_{\parallel} = \omega / k_{\parallel}$, a condition that is called the Landau resonance. In the mechanism proposed by Maggs [1976], incoherent radiation generated by auroral electrons interacts with the beam electrons, thereby stimulating coherent radiation by the Landau resonance. Studies of hiss produced by an artificial electron beam during the Spacelab 2 mission [Farrell et al., 1988, 1989] show that sufficient power levels were produced by coherent bunching in the beam. Farrell et al. [1989] indicate that a beam driven instability is the most likely mechanism for auroral hiss generation.

A spectrogram of auroral hiss produced by the Polar SFR from 09:25 UT to 10:10 UT on February 28, 1997 is shown in Figure 23. This is upward-propagating auroral hiss. A band of chorus can also be seen from 10:10 UT to 10:40 UT. The top panel contains the power spectrum of the electric field as measured by the E_u antenna, and the bottom panel contains the power spectrum of the magnetic field as measured by the loop antenna. The characteristic funnel shape of the auroral hiss is clearly evident in the electric field spectrum. The lower frequency cutoff of the hiss

is approximately 1 kHz at 09:25 UT and gradually descends to 0.2 kHz at 09:45 UT when the spacecraft is nearest to the source region. The low-frequency cutoff then increases to 2 kHz at 10:10 UT. The upper frequency cutoff is approximately 3.3 kHz for the entire funnel. The upper frequency cutoff is somewhat higher, approximately 3.9 kHz, during the electromagnetic bursts at 09:33 UT and 10:00 UT. The upper frequency cutoff occurs at the lower of the plasma frequency or the electron cyclotron frequency [Gurnett et al., 1983]. The plasma frequency cutoff of auroral hiss has been used to measure auroral electron densities by Persoon et al. [1983]. The electron cyclotron frequency is shown by the white line on the spectrogram and ranges from about 10 kHz to 12 kHz during the auroral hiss funnel. The upper frequency cutoff of the auroral hiss is well below the electron cyclotron frequency. Therefore, the upper frequency cutoff is assumed to be at the electron plasma frequency. Much of the auroral hiss is electrostatic, but some short bursts have measurable magnetic components. Some of these bursts pass the coherence and plane wave tests, and can be analyzed with the current method. The wave normal direction of a segment of auroral hiss from 09:33:26 UT to 09:34:13 UT is shown in Figure 24. The wave normal angle varies from approximately 120° at $f \approx 1.1$ kHz to nearly 180° at $f \approx 3.2$ kHz. Figure 25 shows the Poynting flux orientation for the same period. The angle between \vec{B}_0 and the Poynting vector varies from nearly 180° at $f \approx 1.1$ kHz to approximately 140° at $f \approx 3.2$ kHz.

As can be seen from Figure 5 for wave normal angles near the resonance cone, the Poynting vector is nearly perpendicular to the resonance cone. Figure 22

shows the index of refraction curves at two frequencies for the whistler mode.

Index of refraction curves that contain a resonance cone are valid when

$f_{\text{LHR}} < f < \text{Min}(f_c, f_p)$, where $f_{\text{LHR}} = \sqrt{f_{\text{ci}} f_c}$ is the lower hybrid frequency, f_c is the electron cyclotron frequency, and f_{ci} is the ion cyclotron frequency. The index of refraction is plotted as a polar plot with respect to the magnetic field. This curve is defined by the trace of the index of refraction vector as a function of wave normal angle. Note that the wave vector and the index of refraction vector are essentially the same, $\vec{n} = \vec{k}c/\omega$. The index of refraction goes to infinity as the wave normal angle θ approaches the resonance cone angle θ_{Res} . At the resonance cone angle, the wave normal vector is parallel to the index of refraction curve. The expression for the resonance cone angle is given by Stix [1993], and can be written

$$\tan^2 \theta_{\text{Res}} = -\frac{P}{S} = -\frac{1 - f_p^2 / f^2}{1 - f_p^2 / (f^2 - f_c^2)} \quad (58)$$

The electron plasma frequency is given by $f_p = 9\sqrt{n_e}$ kHz, where n_e is the electron number density in cm^{-3} and f_c is the electron cyclotron frequency. The cold plasma parameters, S and P are described in section 3.1 and in Stix [1993]. As shown in Figure 22, at a low frequency, f_1 ($f_1 \ll f_c$, $f_1 \ll f_p$) the resonance cone angle is nearly $\pi/2$. As the frequency increases the resonance cone angle decreases. At frequencies near the upper cutoff frequency of the hiss (i.e., $f \simeq f_p$, the resonance cone angle approaches zero and the wave normal vector is nearly parallel to \vec{B} .

It is well known that the Poynting vector (i.e., the ray path) is perpendicular to the index of refraction surface [Stix, 1993]. For a wave propagating with a wave normal angle very near the resonance cone angle, the Poynting vector is very nearly perpendicular to the resonance cone (and the wave normal vector). This situation is quite unusual since the direction of propagation (\vec{k}) is nearly perpendicular to the direction of energy flow. The corresponding geometry is shown in Figure 22. The ray paths are shown as the arrows drawn perpendicular to the index of refraction curves. For wave normal angles near the resonance cone, the limiting angle ψ_{res} between the Poynting vector and the magnetic field is given by

$$\tan^2 \psi_{\text{res}} = -\frac{S}{P} = -\frac{1 - (f_p^2/f^2 - f_c^2)}{1 - (f_p^2/f^2)} \quad (59)$$

Ion effects are assumed to be negligible [Gurnett et al., 1983]. Referring to Figure 22, at low frequencies, $f_1 \ll f_p$ and $f_1 \ll f_c$, the Poynting vector is nearly parallel to the magnetic field ($\psi_{\text{res}} \rightarrow 0$). At a higher frequency, f_2 , the Poynting vector angle is larger. The Poynting vector angle increases as frequency increases, becoming perpendicular ($\psi_{\text{res}} \rightarrow \pi/2$) when f reaches the lower of f_p or f_c . The funnel shape of the auroral hiss is produced by the behavior of ψ_{res} , since this gives the orientation of the ray path with respect to the geomagnetic field. Experimental evidence is now provided to support these trends in the wave normal and Poynting vector angles.

Figure 26 shows the wave normal angle as a function of frequency observed from 09:33:34.2 UT to 09:33:34.65 UT in Figure 24. The wave normal angles are

the time averages of the angles observed at each frequency for which auroral hiss is observed during the second snapshot. Since the auroral hiss is observed in the northern hemisphere, the magnetic field is directed toward the Earth while the auroral hiss propagates upward, away from the Earth. The wave normal angles and the polar angles of the Poynting vector are therefore greater than 90° . Since it is conventional to represent the wave normal angle and polar angle of the Poynting vector between 0° and 90° , the measured wave normal angles and polar angles of the Poynting vector have been subtracted from 180° . For the rest of this study θ will represent the measured value of the wave normal angle subtracted from 180° , and θ_s will represent the polar angle of the Poynting vector subtracted from 180° . The wave normal angles are approximately 60° at the low-frequency limit of the auroral hiss (1.1 kHz) and become more parallel to the magnetic field as the frequency increases. The wave normal is nearly parallel to the magnetic field at the maximum frequency of 3.2 kHz. Figure 27 shows the frequency dependence of the Poynting vector angle observed from 09:33:34.2 UT to 09:33:34.65 UT in Figure 25. At 1.1 kHz the Poynting vector is nearly parallel to the magnetic field. As the frequency increases, the Poynting vector angle relative to the magnetic field increases. At 3.2 kHz, $\theta_s \approx 35^\circ$. As shown in equation (59) at low frequencies, the angle between the Poynting vector and the geomagnetic field should be small. As the frequency increases, ψ_{res} also increases. It is useful to compare the behavior of ψ_{res} with calculated values of θ_s . At 1.1 kHz, $\theta_s = 8.78^\circ$. The angle θ_s gradually increases as the frequency increases, with $\theta_s = 34.73^\circ$ at 3.4 kHz. This

variation provides qualitative support for the theoretical behavior of the wave normal and Poynting vector angles of auroral hiss. Because the wave normal and Poynting vectors are perpendicular, the azimuth angles should have a difference of 180° . The azimuth angles compared here are the measured azimuth angles. At 1.1 kHz, $\phi \cong 55^\circ$ and $\phi_s \cong 265^\circ$ so that $|\phi - \phi_s| \cong 210^\circ$. At 3.2 kHz $\phi \cong 93^\circ$, $\phi_s \cong 287^\circ$ and $|\phi - \phi_s| \cong 194^\circ$. Therefore the measured azimuth angles are consistent with the expectations of cold plasma theory. Interference from an electrostatic wave from another source can affect the Poynting vector orientation, and can probably account for the small deviations from 180° . The solid curve in Figure 26 is the resonance cone angle θ_{Res} computed from equation (58) using $f_c = 11.11$ kHz (read from the wave normal vector plot in Figure 24) and $f_p = 3.9$ kHz. The plasma frequency was estimated from the frequency of the sharp decrease in Poynting vector magnitude that occurs at this frequency. As can be seen, the measured wave normal angles have values that are 10° to 20° less than the resonance cone angle at corresponding frequencies. This indicates that the measured wave normal vectors are near but inside the resonance cone. Similarly, the theoretical angle of the limiting Poynting vector direction at the resonance cone, ψ_{Res} , is calculated from equation (59) and plotted with the measured Poynting vector direction polar angles in Figure 27. The measured Poynting vector angles are between 6° and 22° closer to the magnetic field direction than are the theoretical values of ψ_{Res} . These trends are consistent with wave propagation at wave normal angles slightly smaller than the resonance cone angle. The sketch of the wave normal surface shown in Figure 5

can be used to illustrate these propagation characteristics. An index of refraction vector that has a wave normal angle θ slightly less than the resonance cone angle, is shown. This situation is qualitatively similar to the measured wave normal angles in Figure 26. The corresponding ray path (and hence Poynting vector) is indicated by the arrow labeled \vec{S} . The angle θ_s between the Poynting vector and \vec{B} must be less than ψ_{Res} (i.e., the Poynting vector is less oblique than the Poynting vector on the resonance cone). This is in agreement with the wave normal and Poynting vector angles, θ and θ_s , calculated for the observed auroral hiss.

The fact that the measured wave normal angles are less than the resonance cone angles indicates that the auroral hiss is not completely electrostatic. The ratio $c|B|/|E|$, where $|B|$ and $|E|$ are the total magnetic and electric field strengths and c is the speed of light, provides a measure of how closely the auroral hiss approaches the electrostatic limit. For electrostatic waves, $c|B|/|E| = 0$. The ratio $c|B|/|E|$ can be calculated from the measured wave normal angles. This value can then be compared to $c|B|/|E|$ calculated directly from the electric and magnetic field intensities. A close match of the two sets of $c|B|/|E|$ ratios then verifies that the auroral hiss is propagating with wave normal angles near the resonance cone, not at the electrostatic limit, and not at the fully electromagnetic limit (i.e., $\theta = 0^\circ$). This comparison will also show that the measured wave normal angles accurately describe the direction of propagation of the auroral hiss.

The average total magnetic and electric field strengths are calculated directly from the electric and magnetic field signals, at the same frequency resolution as the

spectral analysis used to compute the wave normal angles. The $c|B|/|E|$ ratio can be calculated from the wave normal angle by solving equation (15), the homogeneous equation for the electric field. The electron cyclotron frequency, the plasma frequency, the wave frequency, and the wave normal angle are all known input parameters to the equation. The electron cyclotron and plasma frequencies are found by examining the data as described previously. The wave frequencies and corresponding wave normal angles are the values obtained from the wave normal analysis, shown in Figure 26. Two electric field components can be solved in terms of the third. Solving for E_y and E_z in terms of E_x gives

$$E_z = \left(\frac{n^2 \sin \theta \cos \theta}{n^2 \sin^2 \theta - P} \right) E_x \quad (60a)$$

$$E_y = i \left[\frac{-D}{(S - n^2)} \right] E_x \quad (60b)$$

As usual, the index of refraction vector is assumed to be in the x-z plane [see Stix, 1993]. The wave normal angle θ is the angle between the index of refraction vector and the z-axis. To calculate the electric field strength, we assume that E_x has the form $E_x = E_0 e^{-i\omega t} = E_0 (\cos \omega t - i \sin \omega t)$. Solving for the averaged magnitude squared, $|E|^2$, then gives

$$|E|^2 = \frac{1}{2} E_0^2 \left[1 + \left(\frac{D}{S - n^2} \right)^2 + \left(\frac{n^2 \sin \theta \cos \theta}{n^2 \sin^2 \theta - P} \right)^2 \right] \quad (61)$$

where the average value of $\sin^2(\omega t)$ and $\cos^2(\omega t)$ is $1/2$, and the brackets denote the time average.

Using Faraday's law, $\vec{\nabla} \times \vec{E} = -\partial \vec{B} / \partial t$, it is easy to show that the magnetic field components are given by

$$c B_x = -n \cos \theta E_y \quad (62a)$$

$$c B_y = n \cos \theta E_x - n \sin \theta E_z \quad (62b)$$

$$c B_z = n \sin \theta E_y \quad (62c)$$

where c is the speed of light. Solving for $|cB|^2$ gives

$$|cB|^2 = \frac{1}{2} E_0^2 \left[\left(\frac{nD}{S - n^2} \right)^2 + \left(\frac{n P \cos \theta}{n^2 \sin^2 \theta - P} \right)^2 \right] \quad (63)$$

Equations (61) and (63) can then be used to calculate $c|B|/|E|$ as a function of wave normal angle. The results of these calculations are shown in Figure 28. The $c|B|/|E|$ values calculated from the measured auroral hiss wave normal angles are plotted as filled circles. The error bars on the $c|B|/|E|$ values have been calculated

from the error limits on the wave normal angle measurements (see Figure 26). These data are plotted at the frequencies determined by the spectral analysis. The $c|B|/|E|$ values calculated from the measured electric and magnetic fields are plotted as open circles, shifted slightly from the analysis frequency to avoid overlap of the error bars. The error bars are determined by the confidence factor of the spectral analysis, as described in Chapter 5. The confidence limits are here interpreted as providing an estimate of the error in the calculation of $c|B|/|E|$.

As can be seen, the $c|B|/|E|$ ratios calculated by the two methods show good agreement. The values computed from the measured fields have values between 0.9 and 0.5, while the values computed using the measured wave normal vectors are generally just above 1. The two sets of data agree to within the error limits. Values of $c|B|/|E|$ of approximately 1 are generally indicative of waves propagating in a quasi-electrostatic mode but with measurable magnetic field intensities [Hayakawa et al., 1984]. Because of the reasonable agreement between the two methods of calculating $c|B|/|E|$, it is concluded that the analyzed auroral hiss propagates in an electromagnetic mode that is close to, but not at, the electrostatic limit.

Further study of these waves and comparison with electron distributions could determine why the auroral hiss exhibits electromagnetic enhancements while otherwise remaining electrostatic.

CHAPTER VIII. CONCLUSIONS

Three-axis electric and magnetic field waveforms measured by the Polar Plasma Wave Instrument are used to study whistler-mode chorus and auroral hiss. The Poynting vector orientation has been used to locate the source region of whistler-mode chorus. Poynting vector direction was calculated using the survey mode for a large number of chorus events. The chorus was observed almost without exception to propagate northward when observed in the northern magnetic hemisphere, and southward when observed in the southern magnetic hemisphere, showing that chorus propagates away from the magnetic equator. Additionally, there is no evidence of chorus reflected from the ionosphere or high-latitude magnetosphere. This implies that chorus is absorbed, possibly by Landau damping, before the reflected wave can return to the magnetic equator.

The observed generation region appears quite small, as there is a very abrupt transition from southward to northward propagation at the magnetic equator. The waves do not grow to significant amplitudes until they have crossed the magnetic equator, but they reach saturation amplitude within a few degrees of the magnetic equator, implying a fast growth rate. The absence of reflected chorus indicates that generation mechanisms requiring reflection and multiple passes through the magnetic equatorial region, such as the mechanism of Kennel and Petschek [1966], are not

adequate to explain chorus generation. Future comparison of wave normal measurements with electron pitch angle and energy distribution should further the understanding of the generation of chorus.

Auroral hiss is believed to propagate in a quasi-electrostatic mode. In this mode, the wave normal angle is very near the resonance cone angle and the Poynting vector is perpendicular to the wave normal vector. At low frequencies, $f \ll f_c$ and $f \ll f_p$, the wave normal angle is predicted to be nearly perpendicular to the geomagnetic field. The wave normal angle decreases with increasing frequency until it is nearly parallel at the hiss cutoff frequency. The Poynting vector should be nearly parallel to the geomagnetic field at low frequencies and approach perpendicular near the cutoff frequency.

There are occasional electromagnetic bursts of auroral hiss when wave normal and Poynting vectors can be computed. During one such event, the wave normal and Poynting angles were observed to follow the trends described above. This provides direct evidence for the quasi-electrostatic theory of auroral hiss propagation. However, the emission must be electromagnetic to be analyzed. The $c|B|/|E|$ ratio is calculated using the measured electric and magnetic fields. The same ratio is also derived as a function of wave normal angle from the whistler mode homogeneous equation, then computed using the observed wave normal angles of the auroral hiss. A comparison of $c|B|/|E|$ calculated in these two ways shows that the analyzed auroral hiss propagates in a quasi-electrostatic whistler mode, but with a measurable magnetic component. The auroral hiss wave normal angles are

within 20° of the resonance cone. These wave normal angles are consistent with propagation in the described quasi-electrostatic mode. The mechanism that causes the electrostatic emissions to become electromagnetic has not been determined.

The wave normal direction and Poynting vector direction can be used in several ways. Most fundamentally, the wave normal and Poynting vectors indicate the direction of the phase and group velocities of an electromagnetic wave, and therefore indicate the direction of propagation of that wave and its energy. This information can in turn be used to locate and study source regions as well as to verify theoretical predictions of the propagation characteristics of some waves. The wave normal angle, the parallel component of the wave normal vector, and the angle between the wave normal and Poynting vectors can be used as parameters for use in dispersion relations and ray tracing simulations. The wave normal calculation method cannot be used to study wave growth regions, however. The Fourier transform gives an adequate frequency-space representation of a time series only if the time series data is stationary. For a stationary data set, the power spectrum does not change with time. During wave growth, the data will be nonstationary and the spectral analysis cannot be applied.

Future studies are planned that will generalize the present analysis for use on other modes of HFWR operation, for use on the PWI Low Frequency Waveform Receiver (LFWR) or for use with data produced by similar instruments on other spacecraft such as the Cassini mission to Saturn.

Figure 1. The major regions of Earth's magnetosphere with a representative Polar orbit.

A-698-113

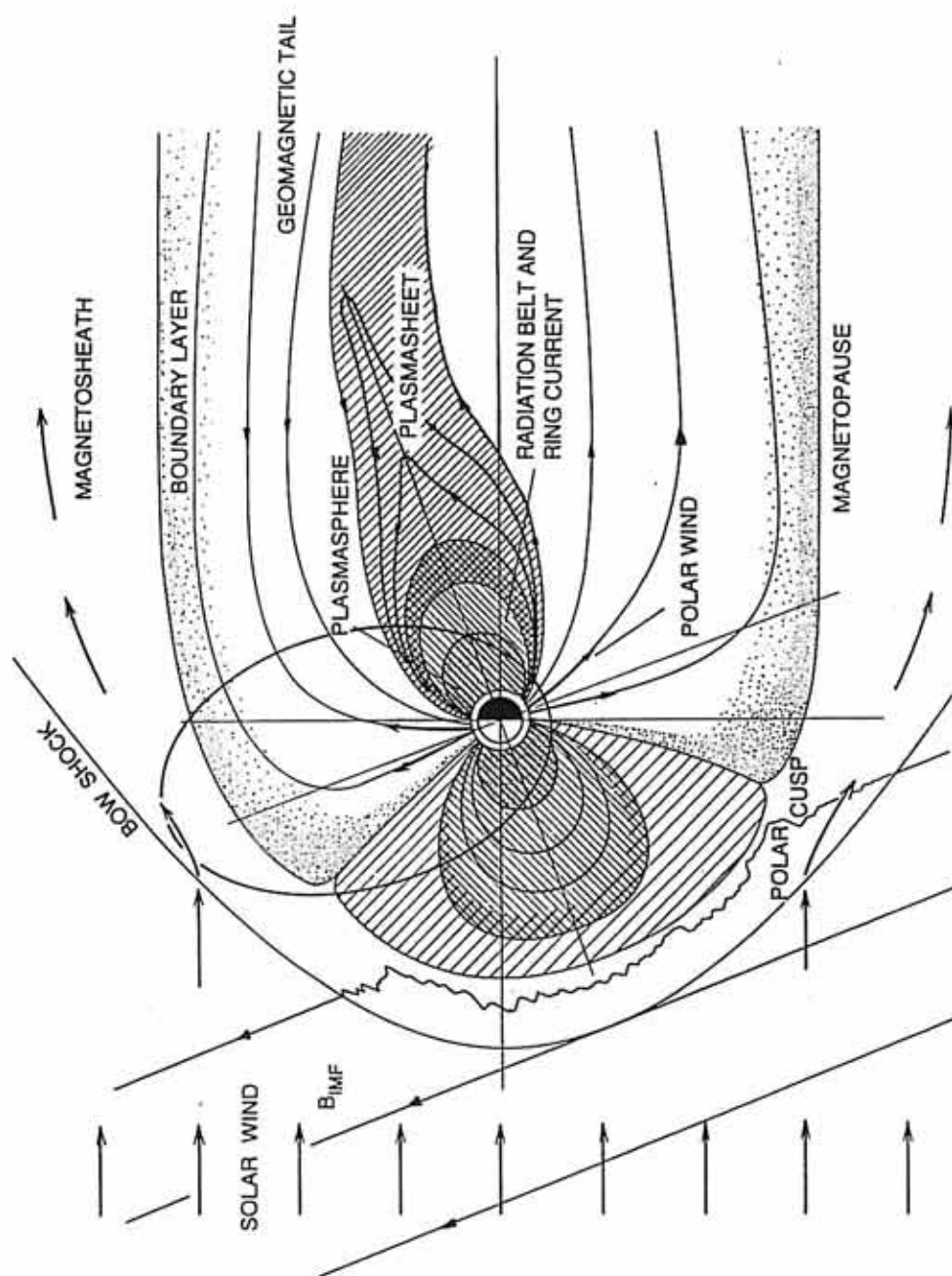


Figure 2. A sketch of the Polar spacecraft showing PWI sensor locations and orientations.

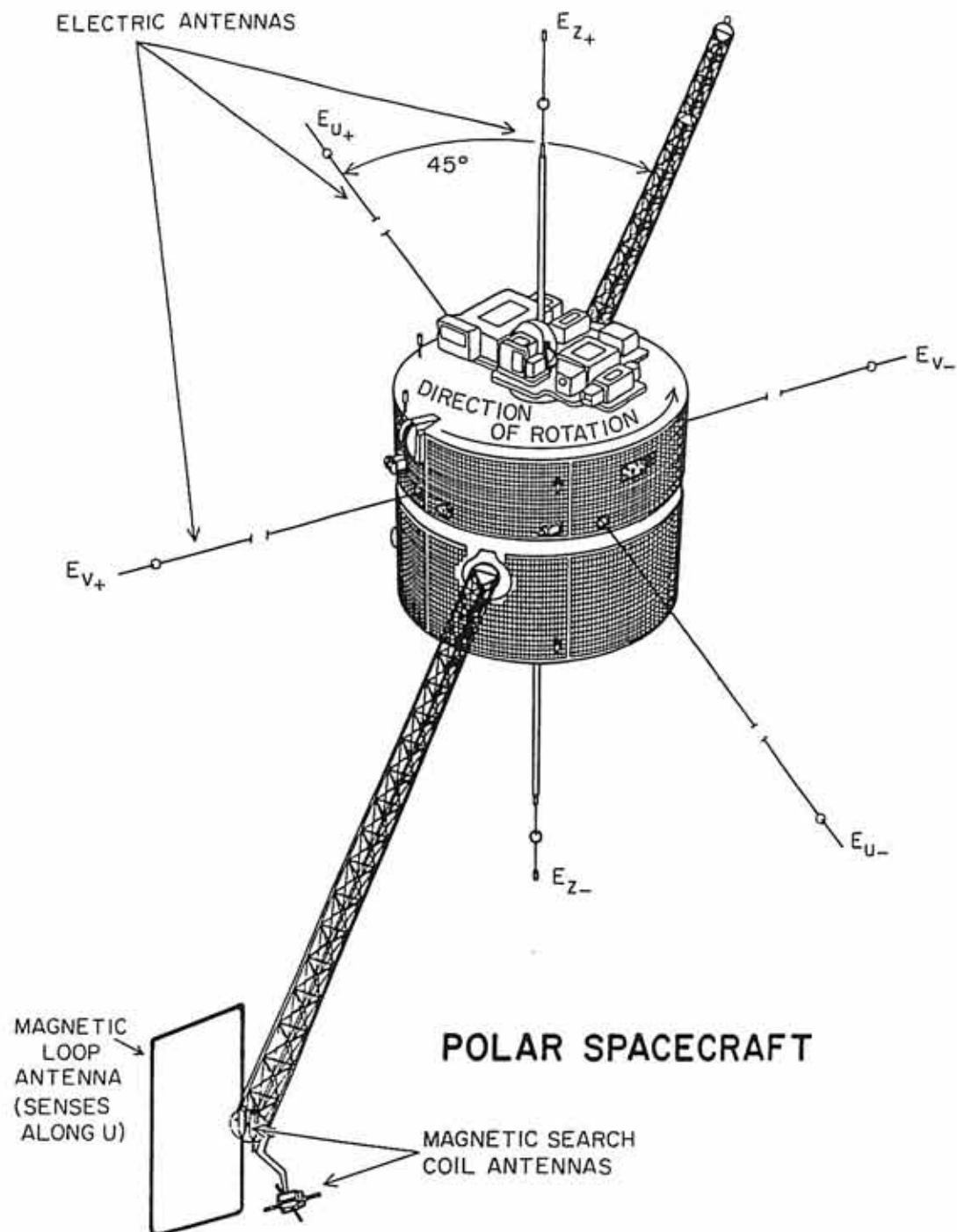
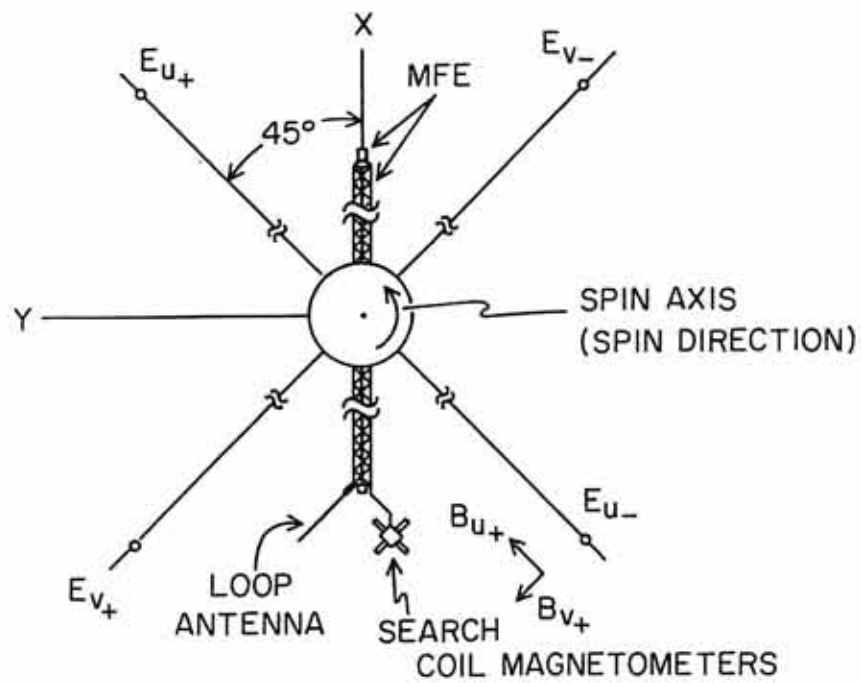


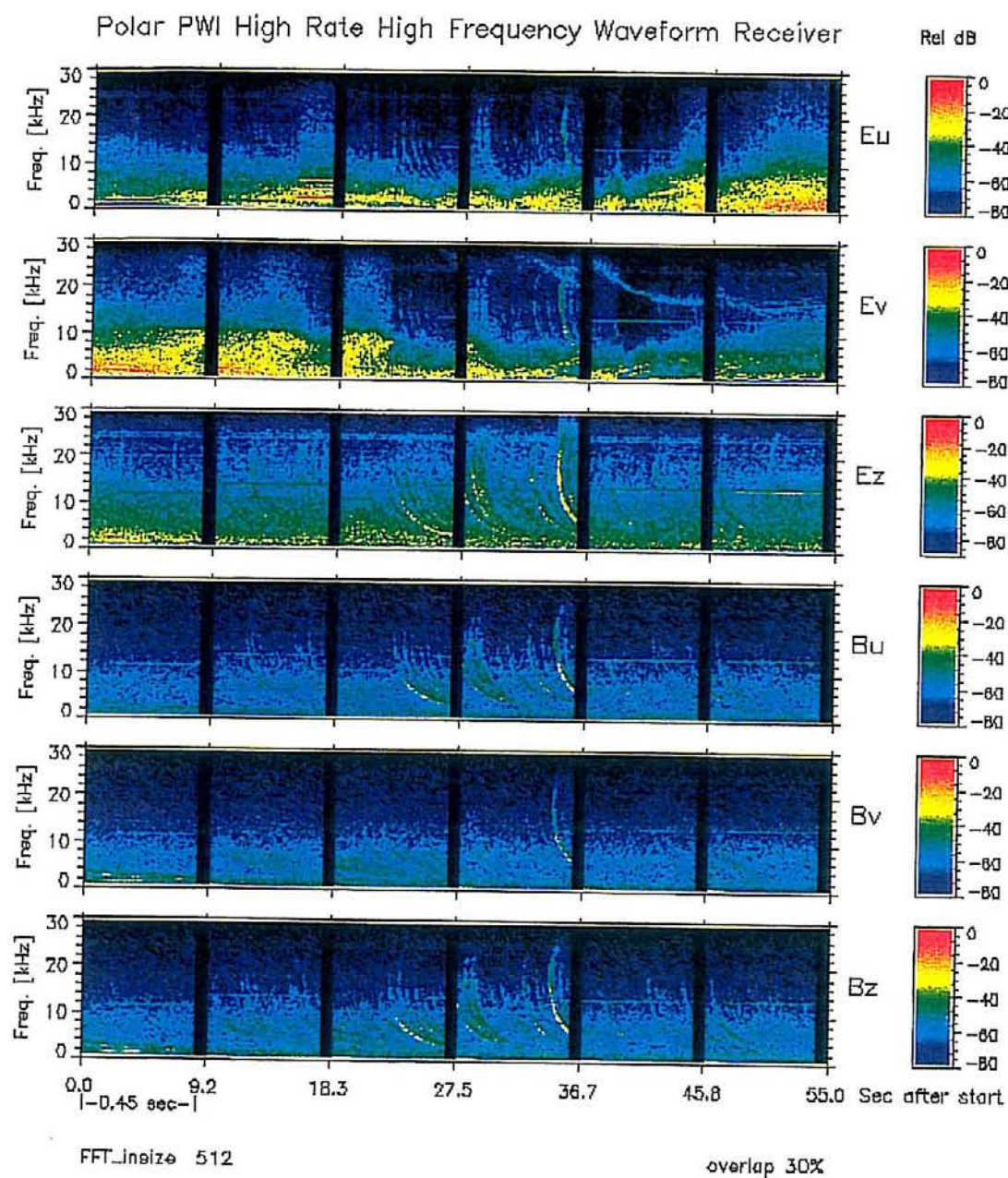
Figure 3. Top view of the Polar spacecraft showing PWI sensor orientations.

A-G97-96-1



POLAR SPACECRAFT - TOP VIEW

Figure 4. A spectrogram of PWI/HFWR 6-channel mode data on September 11, 1996, from 09:11:56 UT to 09:12:42 UT. The spacecraft is at $L = 2.6$, $R = 2.6 R_E$, $MLT = 02.42$, $\lambda_m = 2.1^\circ$.



SCET: 96-09-11T09:11:56.492 to 96-09-11T09:12:42.942

Figure 5. Whistler-mode index of refraction curve for frequencies greater than the lower hybrid frequency and less than the electron cyclotron frequency. The index of refraction vector is parallel to the wave vector. The wave normal angle is θ . The angle between the Poynting vector \vec{S} and \vec{B}_0 is θ_s .

A-G98-118

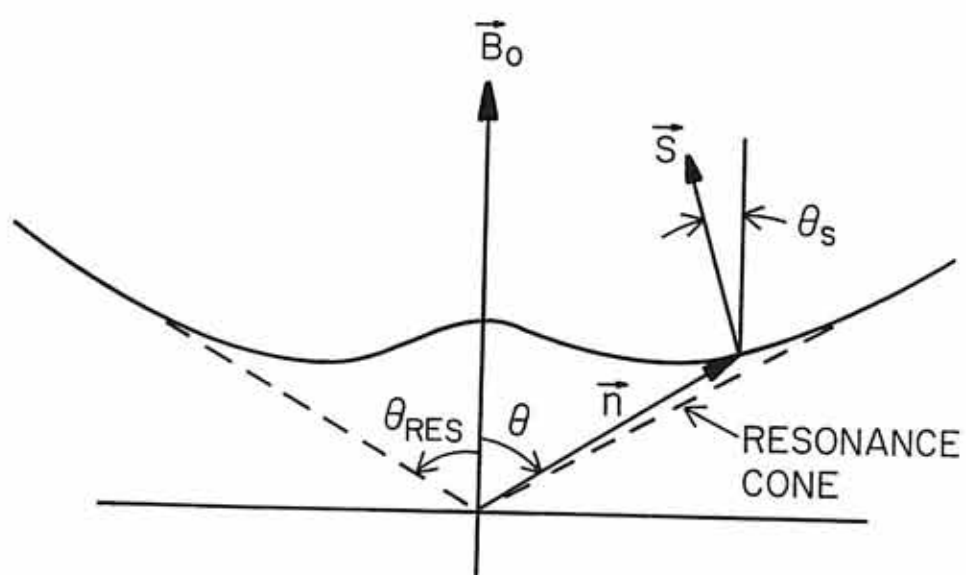
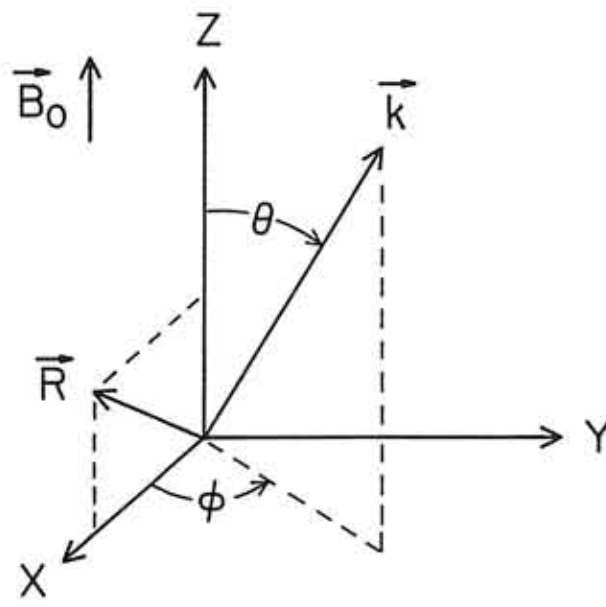
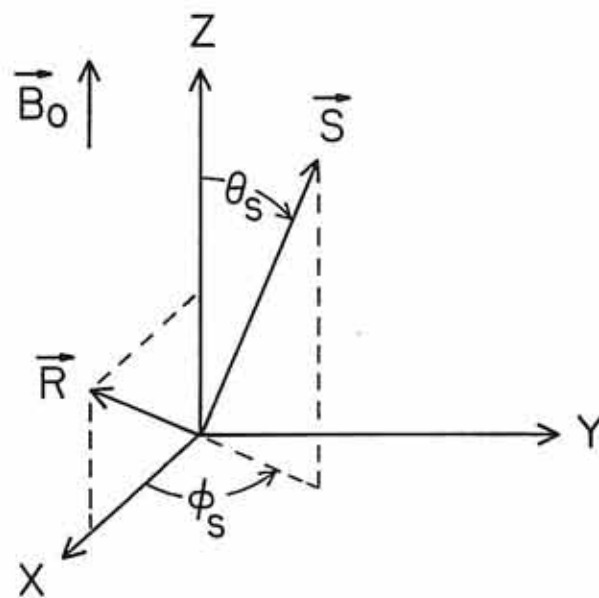


Figure 6. Diagram showing the local geomagnetic field-aligned coordinate system. (a) The orientation of the wave normal vector in the local geomagnetic field-aligned coordinate system. (b) The orientation of the Poynting vector in the same coordinate system



(a)



(b)

Figure 7. Electric power spectrum, magnetic power spectrum, wave normal angle, azimuthal angle of the wave normal vector, coherence, and polarization of emissions from 09:11:56 UT to 09:12:42 UT on September 11, 1996.

Polar PWI HR HFWR Wave Normal Direction
 SCET: 96-09-11T09:11:56.492 to 96-09-11T09:12:42.942

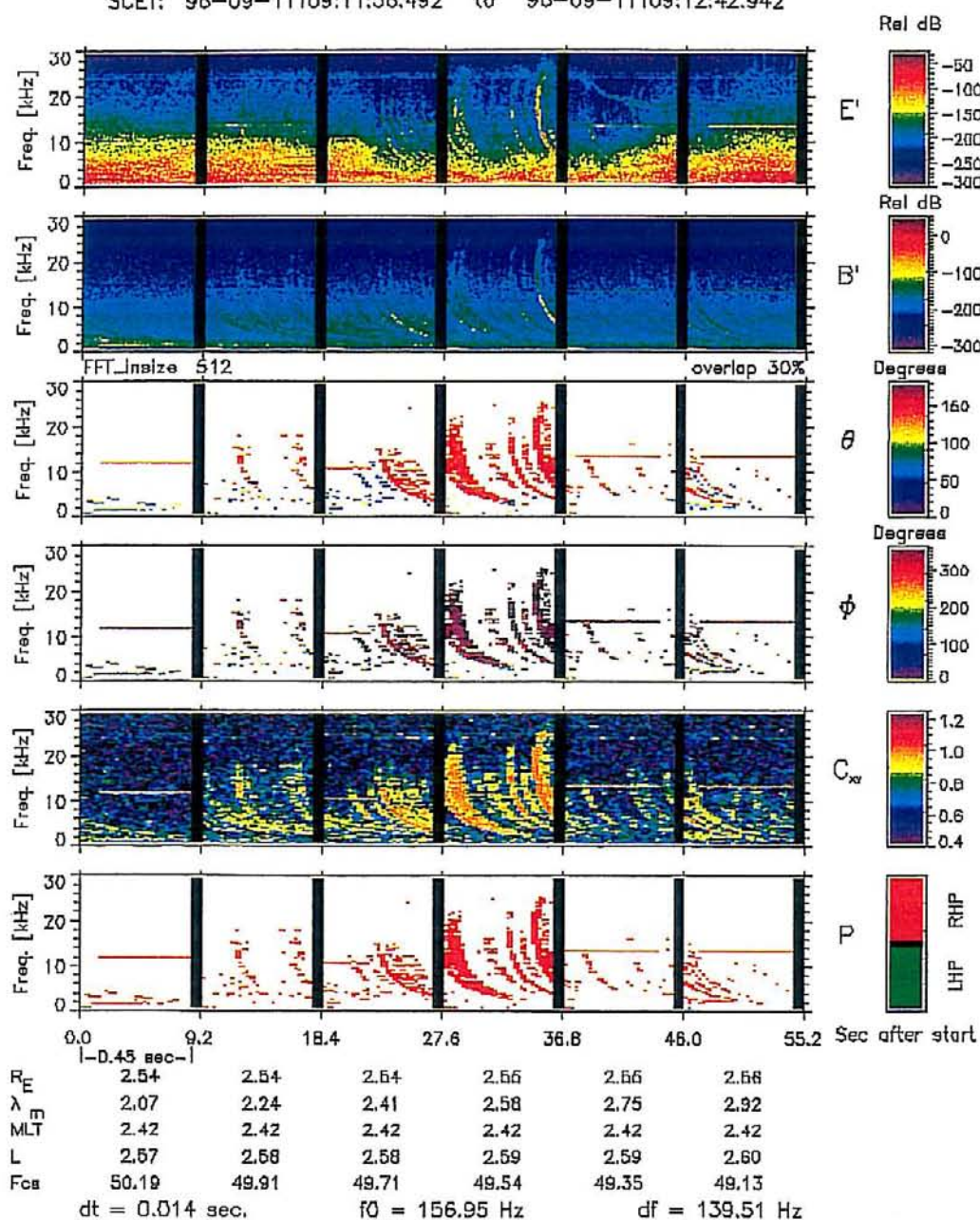


Figure 8. Poynting flux, polar angle of Poynting vector, azimuthal angle of Poynting vector, eigenvalue ratio of spectral matrix, coherence, and direction of S_z for emissions from 09:11:56 UT to 09:12:42 UT on September 11, 1996.

Polar PWI HR HFWR Poynting Flux Direction
 SCET: 96-09-11T09:11:56.492 to 96-09-11T09:12:42.942

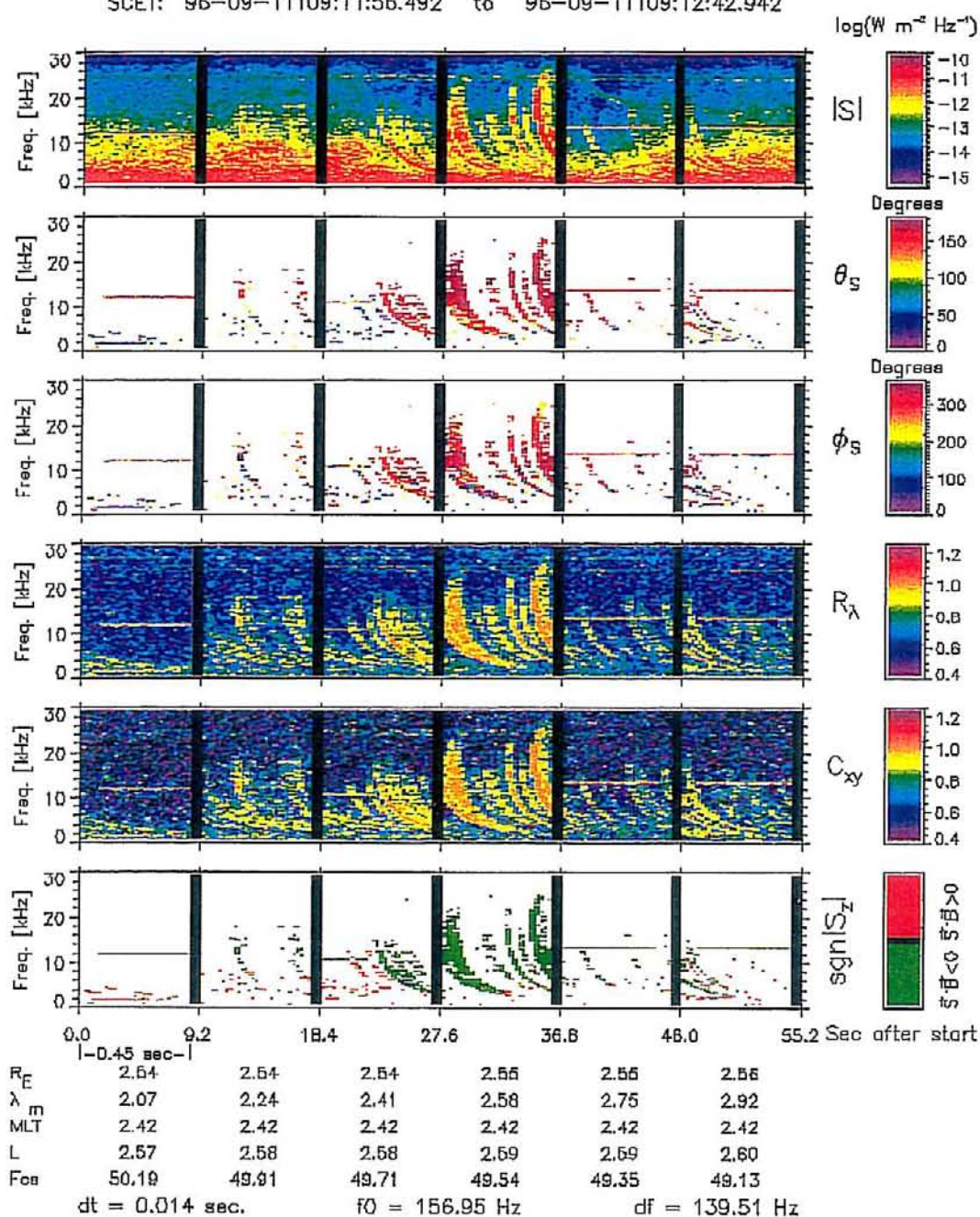
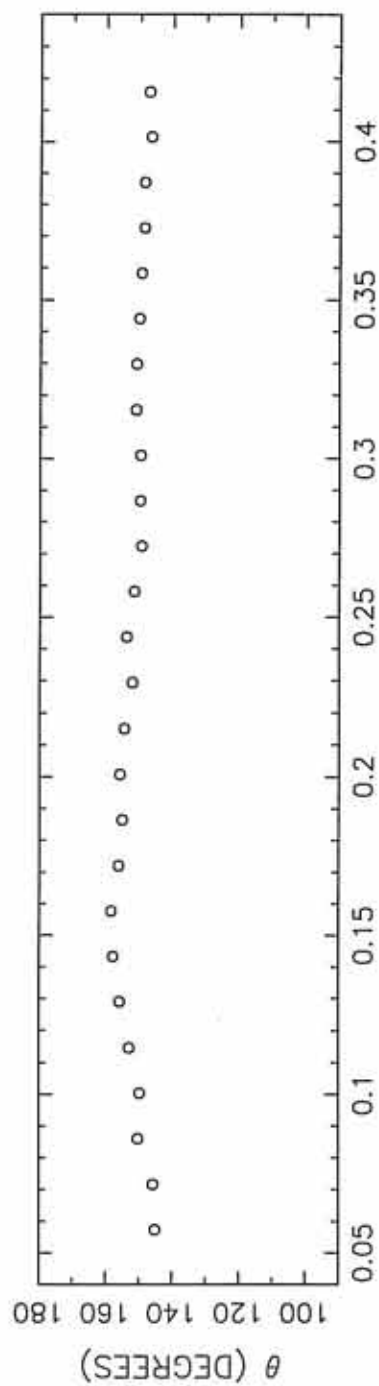
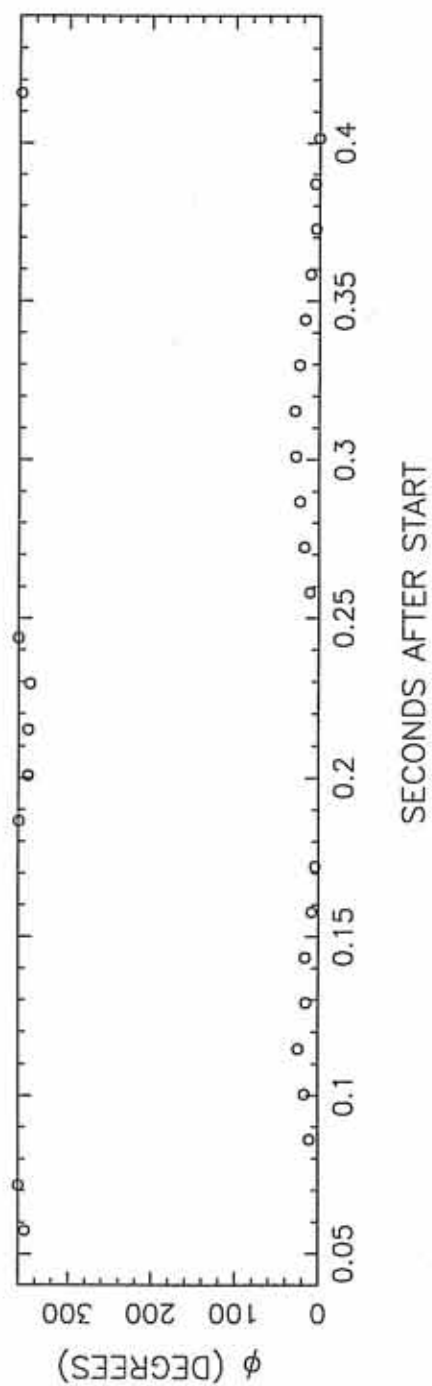


Figure 9. Wave normal vector orientation angles for the 13.1 kHz Omega signal at 09:12:42.492 UT to 09:12:42.942 UT. The top panel contains wave normal angle. The bottom panel contains azimuth angle of the wave normal vector.

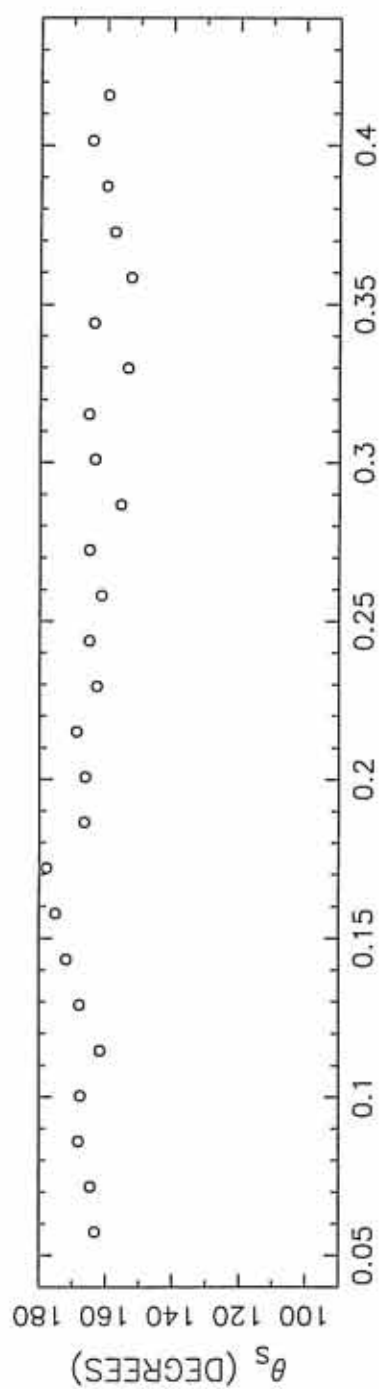


SECONDS AFTER START

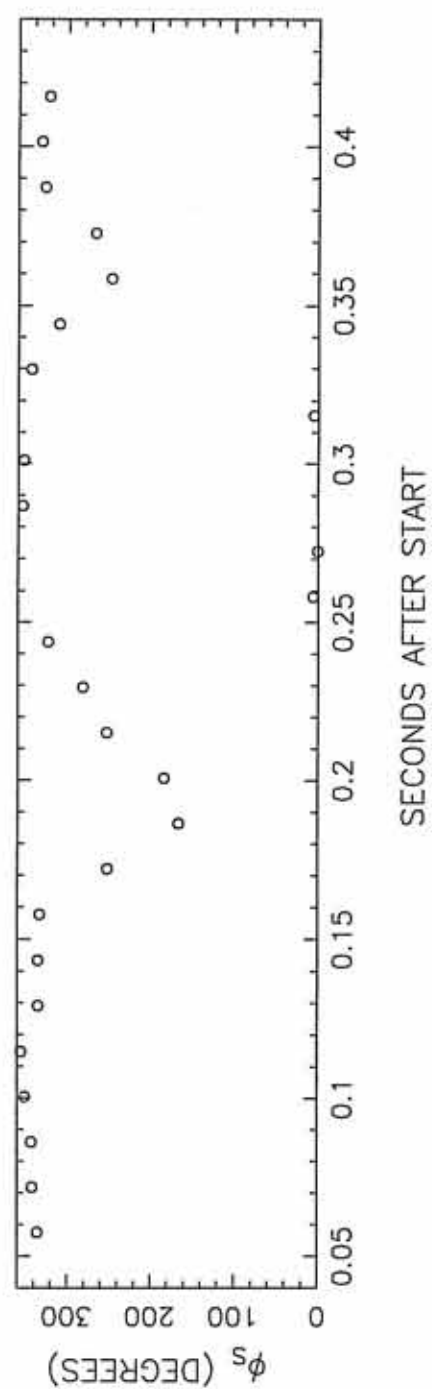


SECONDS AFTER START

Figure 10. Poynting vector orientation angles for the 13.1 kHz Omega signal at 09:12:42.492 UT to 09:12:42.942 UT. The top panel contains the polar angle of the Poynting vector. The bottom panel contains the azimuth angle of the Poynting vector.



SECONDS AFTER START



SECONDS AFTER START

Figure 11. Cross-power spectral density at 09:12:42.224 UT on September 11, 1996

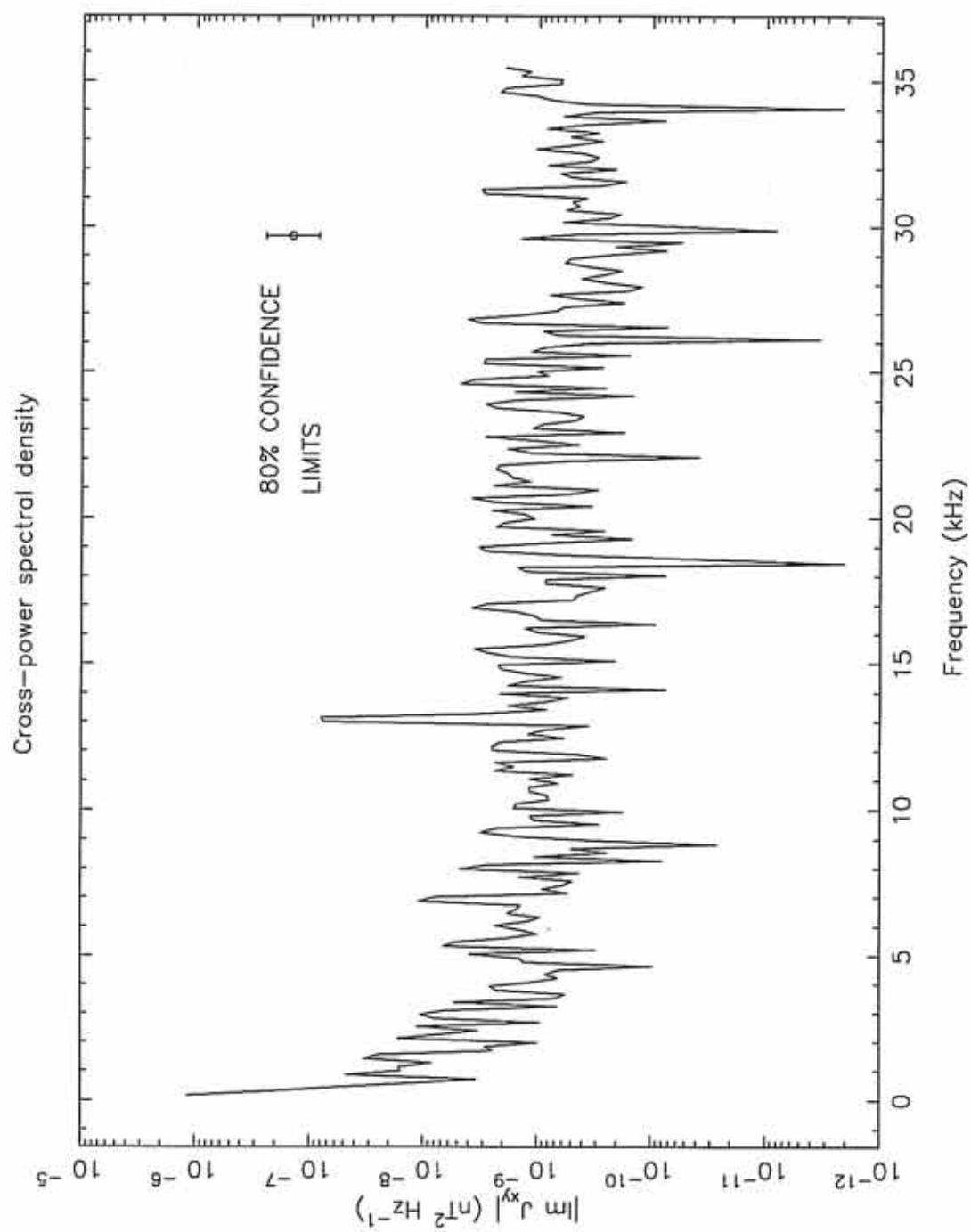
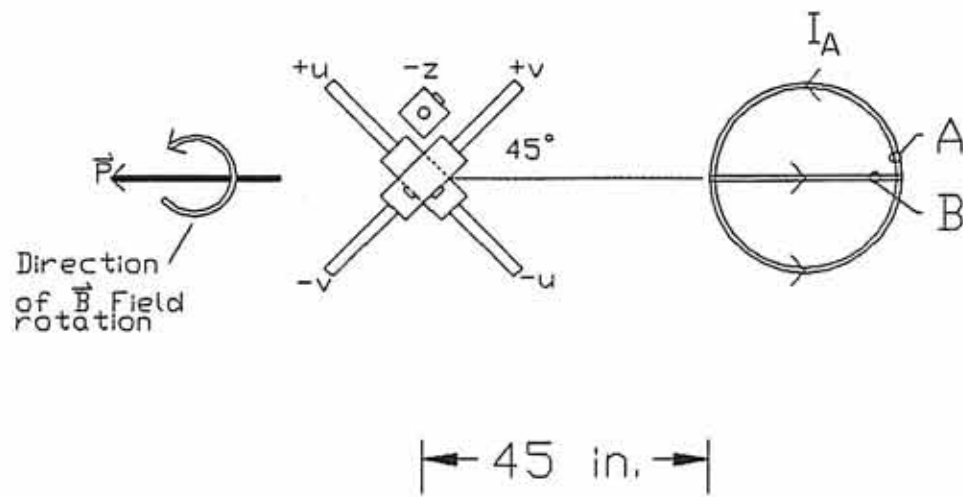
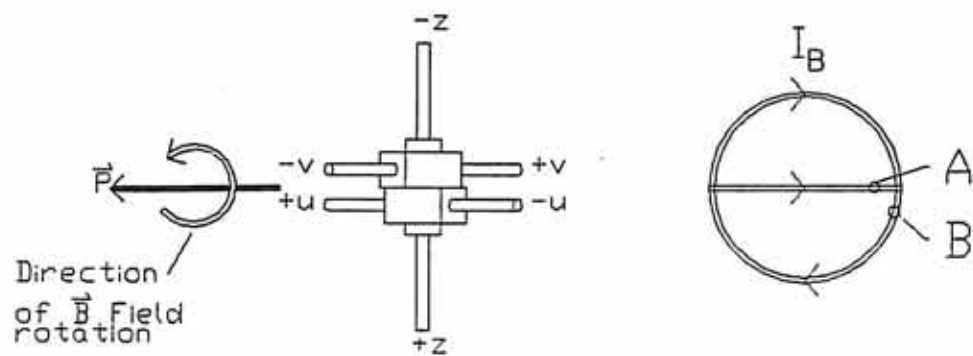


Figure 12. Sketch of GSFC Magnetic Field Test Facility PWI search coil tests for waves propagating in the search coil U-V plane. (a) Top view. (b) Side view.

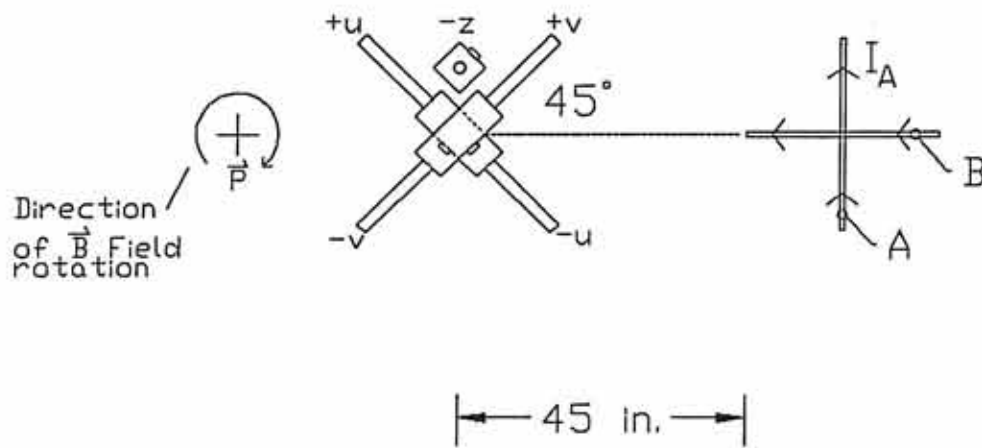


(a)

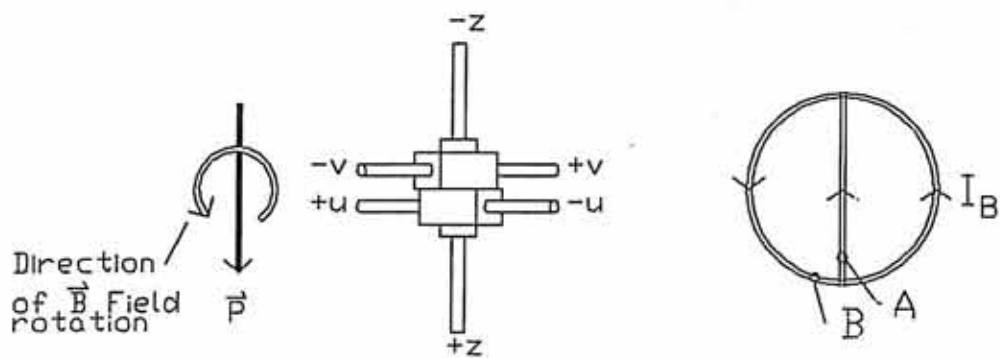


(b)

Figure 13. Sketch of GSFC Magnetic Field Test Facility PWI search coil tests for waves with wave normal parallel to Z search coil. (a) Top view.
(b) Side view.



(a)



(b)

Figure 14. Path of the endpoint of the geomagnetic field that intersects the Polar orbit from 09:00 UT to 09:15 UT on September 11, 1996.

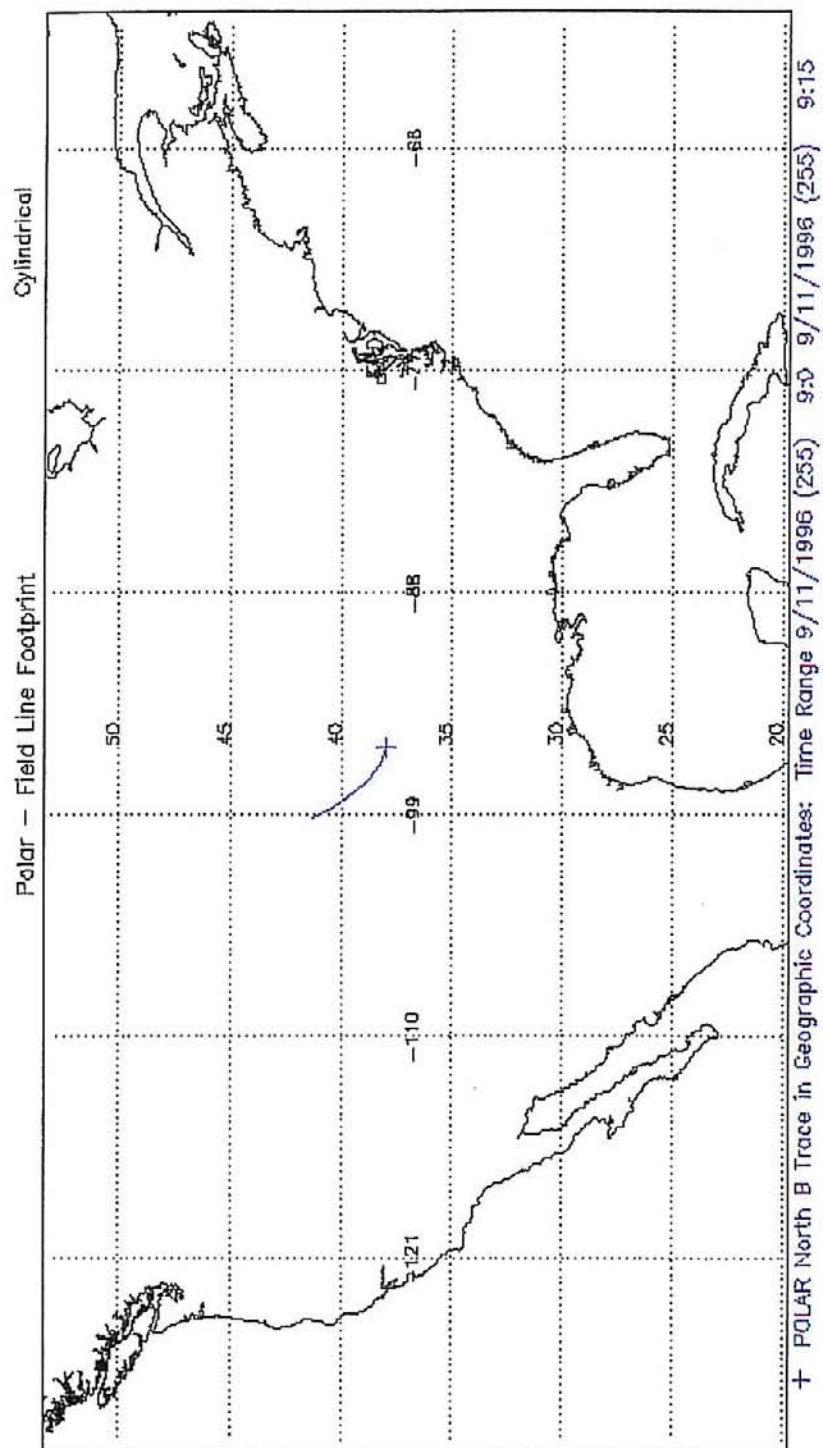


Figure 15. Location of cloud-to-ground lightning flashes observed in the United States by the U.S. National Lightning Detection Network from 09:00 UT to 09:15 UT on September 11, 1996.

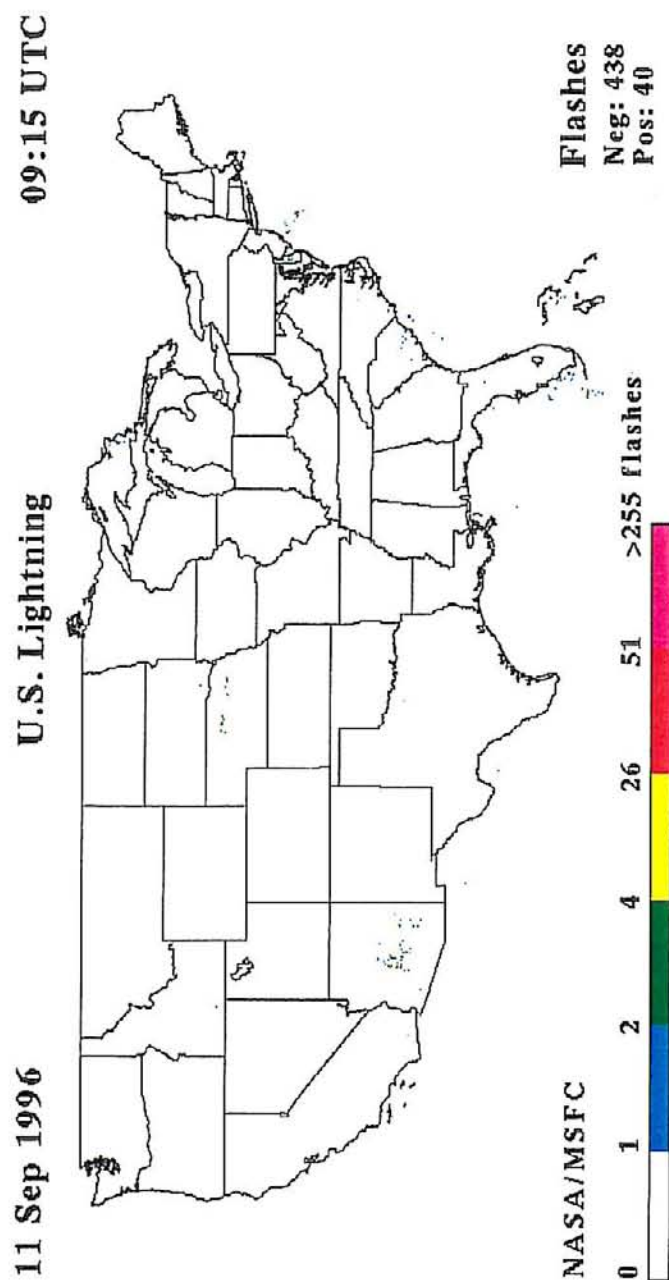


Figure 16. Ray path of a 15.5-kHz signal launched from 45° magnetic latitude. The wave normal angle increases as the wave propagates. Dipole magnetic field lines are shown as dashed lines.

A-G98-105

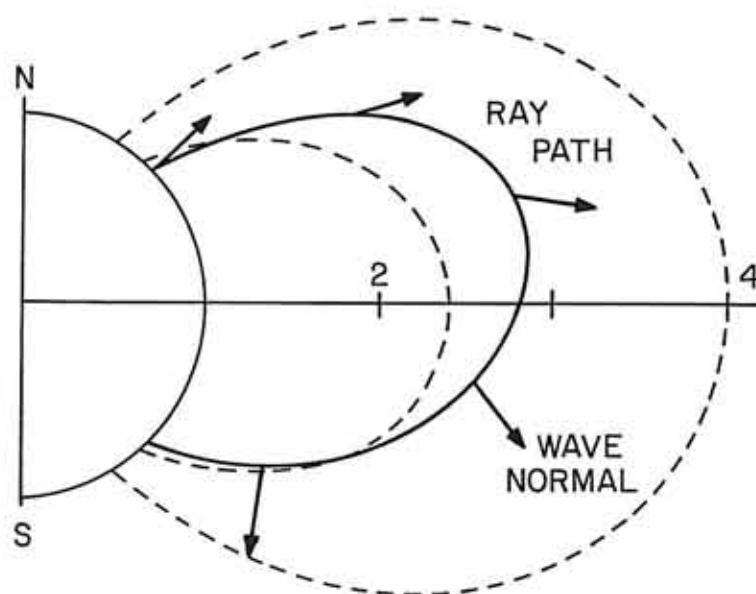


Figure 17. Diagram of the suggested chorus generation region at the magnetic equator.

A-G98-119

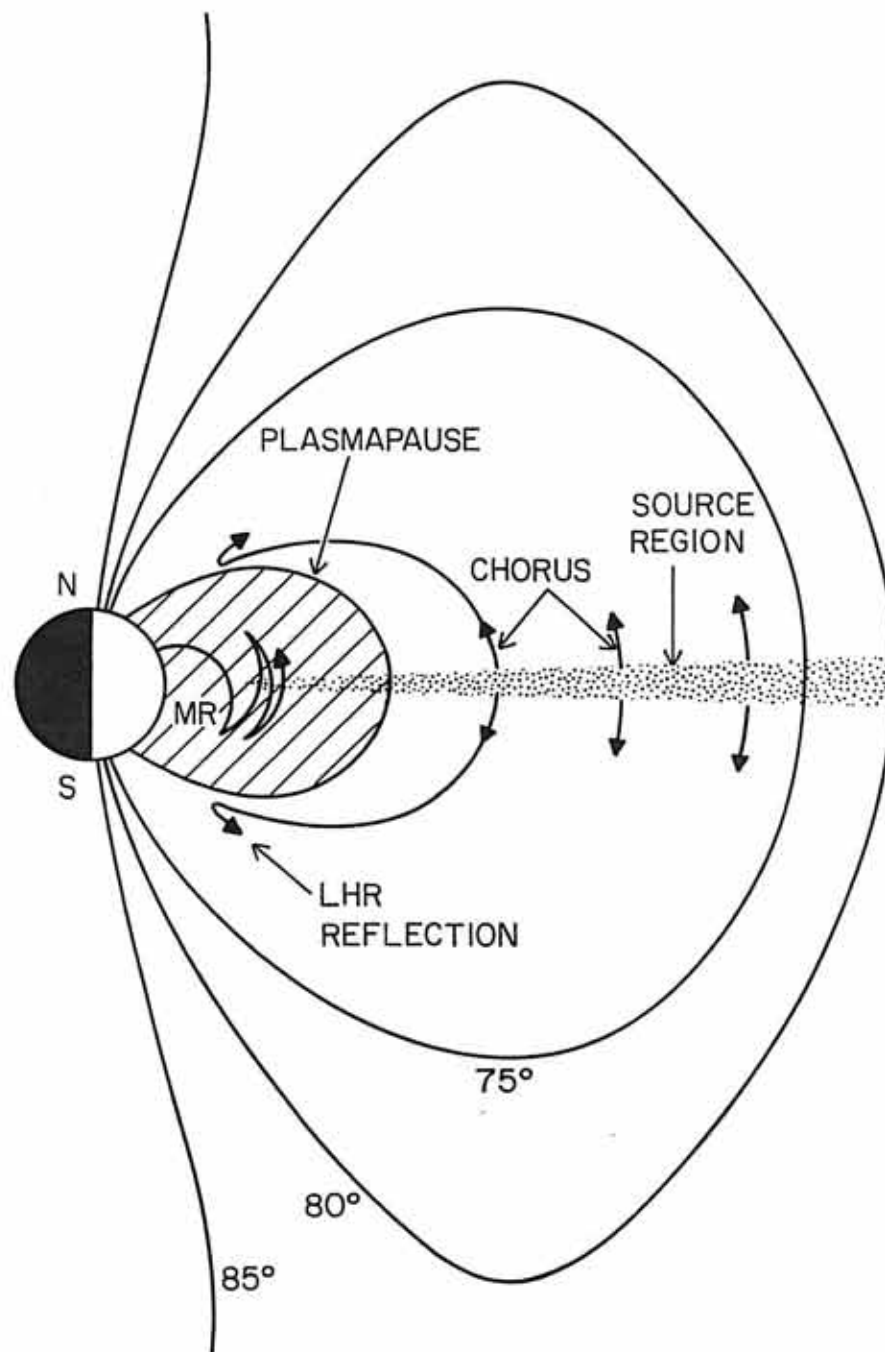


Figure 18. Electric power spectrum, magnetic power spectrum, wave normal angle, azimuthal angle of the wave normal vector, coherence, and polarization of chorus from 00:23:07 UT to 00:23:53 UT on November 25, 1996.

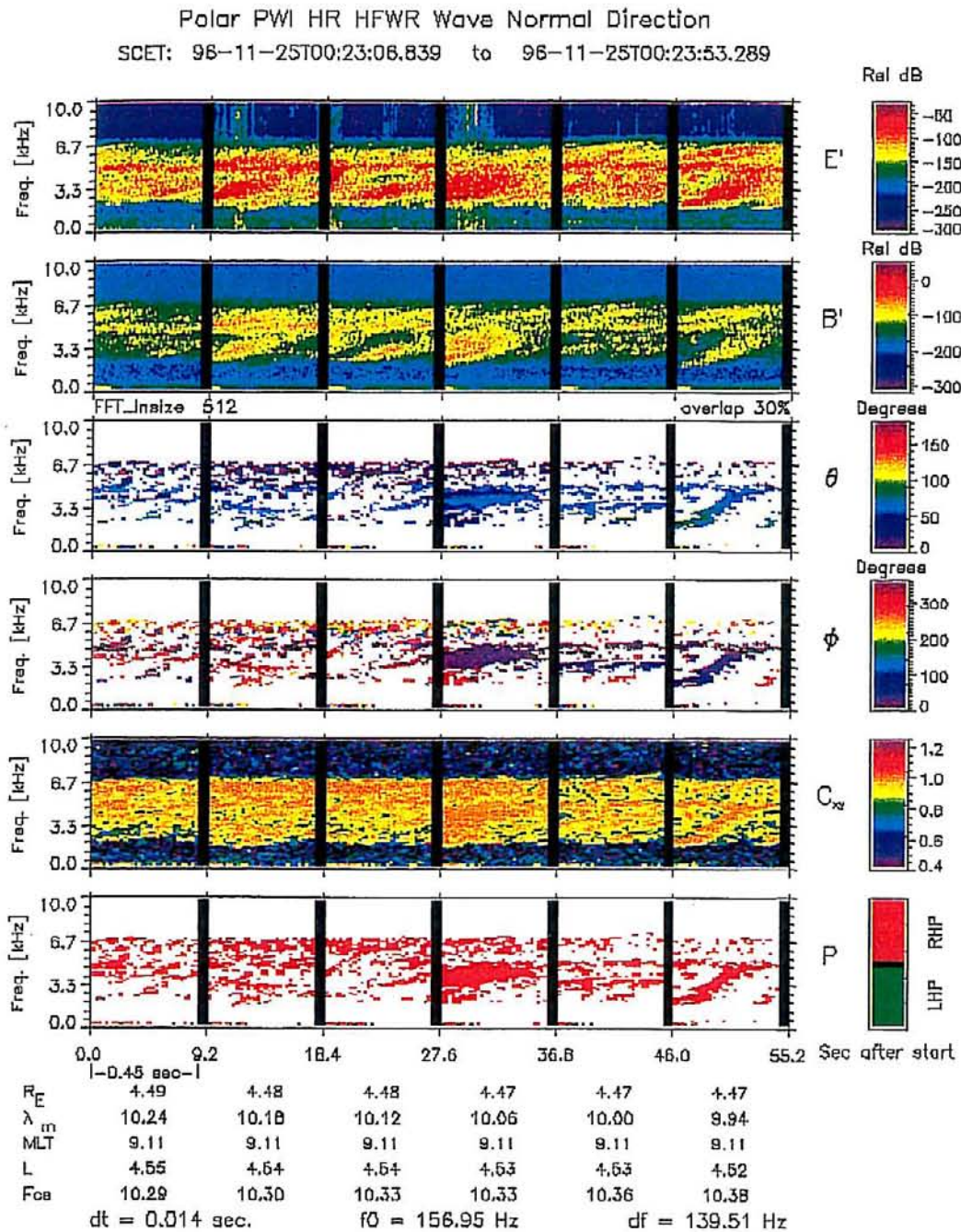


Figure 19. Poynting flux, polar angle of Poynting vector, azimuthal angle of Poynting vector, eigenvalue ratio of spectral matrix, coherence, and direction of S_z for chorus from 00:23:07 UT to 00:23:53 UT on November 25, 1996

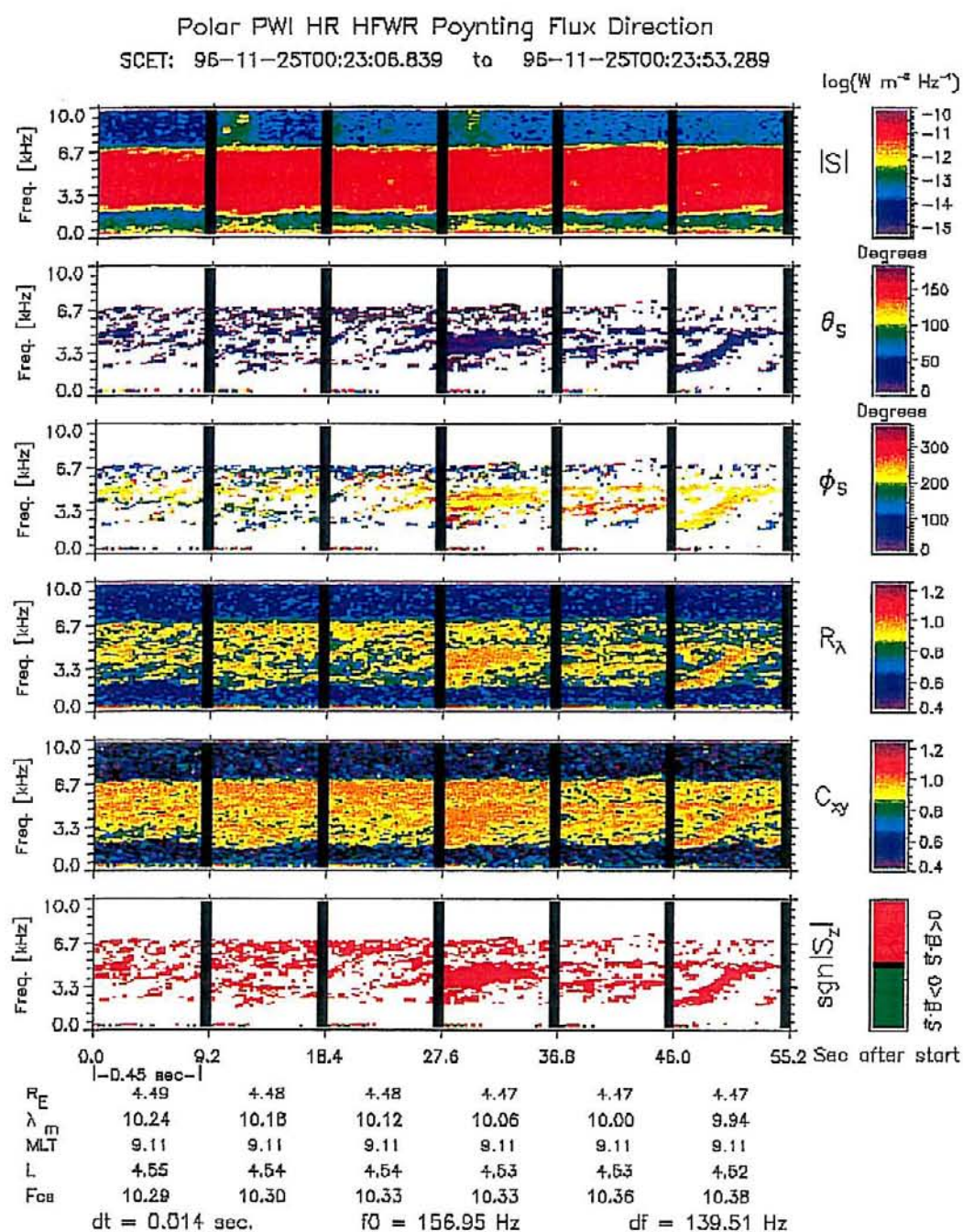
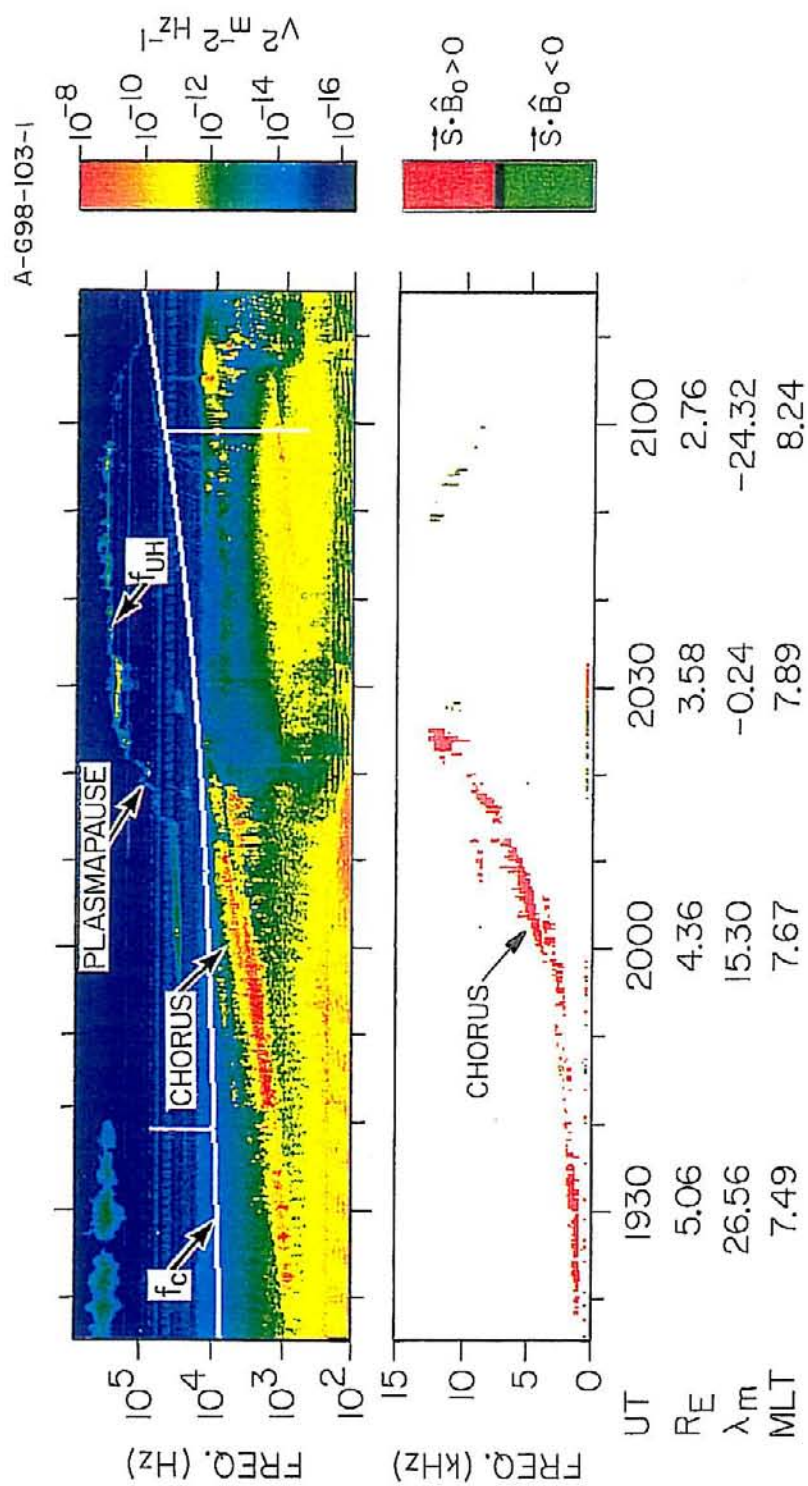


Figure 20. Spectrograms of chorus observed both north and south of the geomagnetic equator on December 14, 1996. The top panel is from the Sweep Frequency Receiver (SFR). Note the logarithmic frequency scale. The bottom panel is from the High Frequency Waveform Receiver (HFWR), and shows the sign of $S_z = \vec{S} \cdot \hat{B}_0$.



POLAR, DAY 349, DEC. 14, 1996

Figure 21. A magnetic meridian plane plot showing the direction of propagation of chorus with respect to the magnetic field. Events with $\vec{S} \cdot \hat{B}_0 \geq 0$ (red) are propagating northward, and events with $\vec{S} \cdot \hat{B}_0 \leq 0$ (green) are propagating southward. As can be seen, chorus essentially always propagating away from the magnetic equator, which means that the source is located very close to the magnetic equator.

A-G98-116

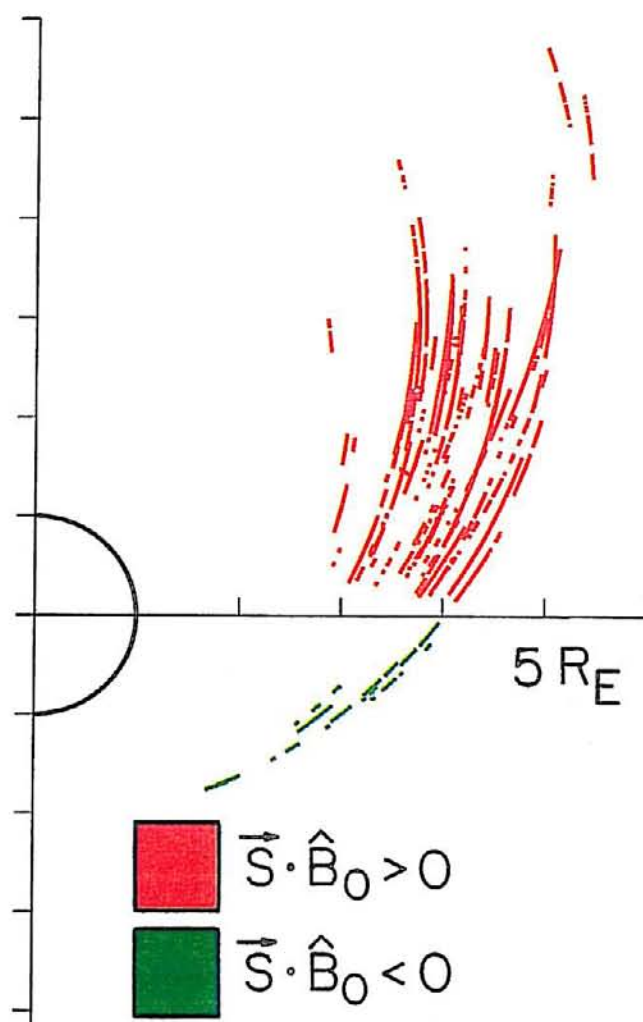


Figure 22. Index of refraction surfaces and geometric representation of ray paths that are characteristic of quasi-electrostatic auroral hiss. Observations of the radiation along the satellite path produces a funnel-shaped spectrum on a frequency-time spectrogram.

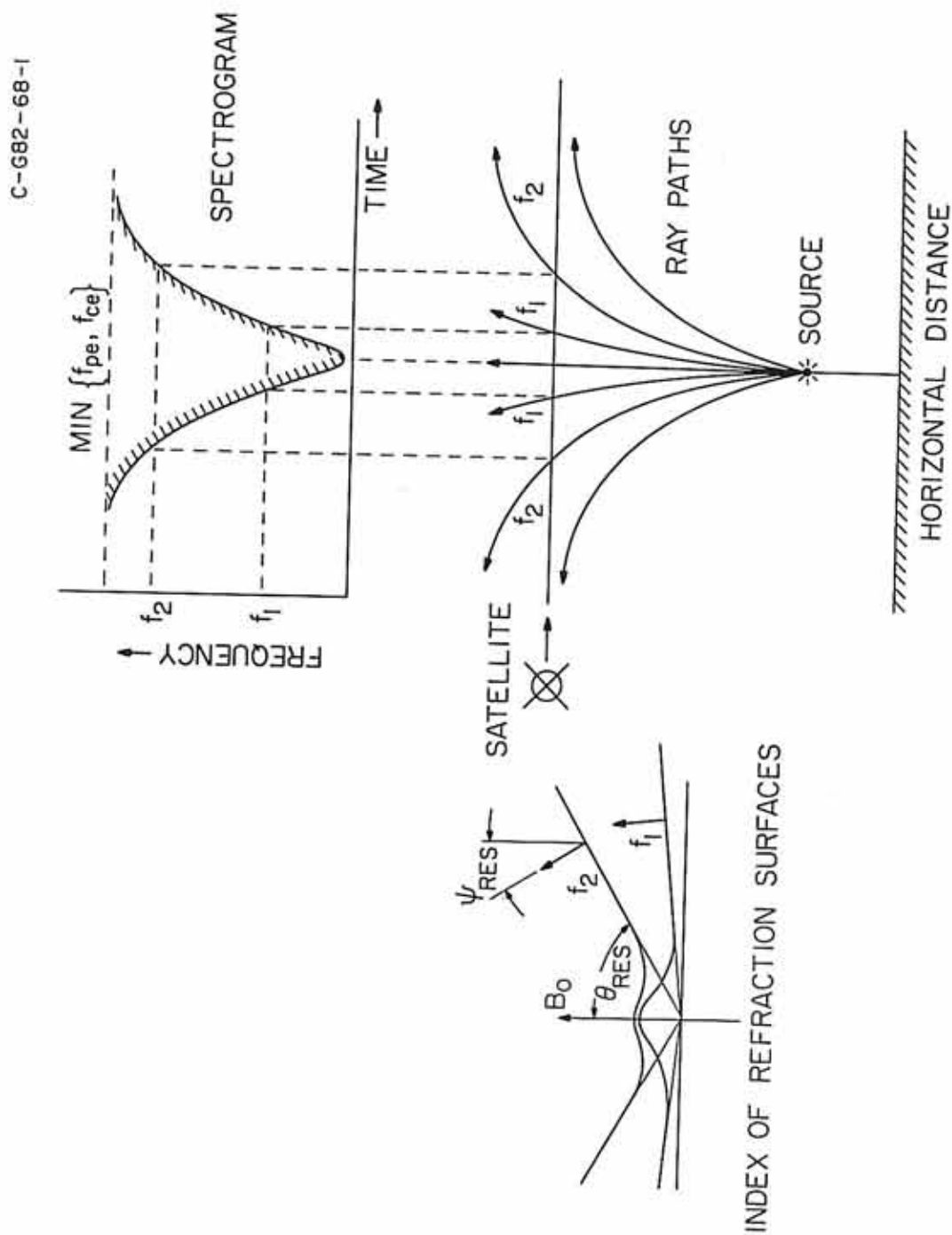
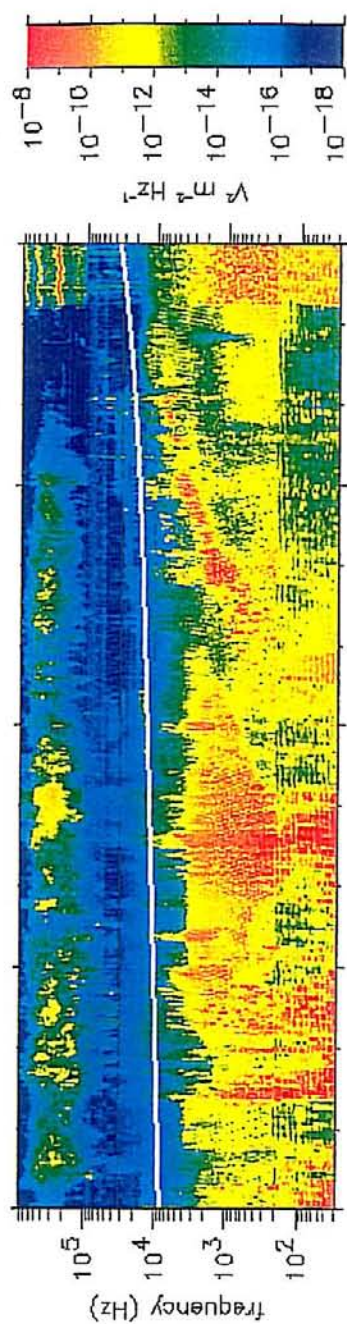


Figure 23. Spectrogram of auroral hiss funnel from the Polar SFR on February 28, 1997 from 09:00 UT to 11:00 UT. The top panel is the electric power spectral density and the bottom panel is the magnetic power spectral density. An auroral hiss funnel is seen in the top panel from 09:25 UT to 10:10 UT. Electromagnetic bursts are seen in the bottom panel at 09:33 UT and 09:59 UT.

1997/02/28 09:00 Polar PWI SFR-A Eu 1997/02/28 11:00



Polar PWI SFR-B L

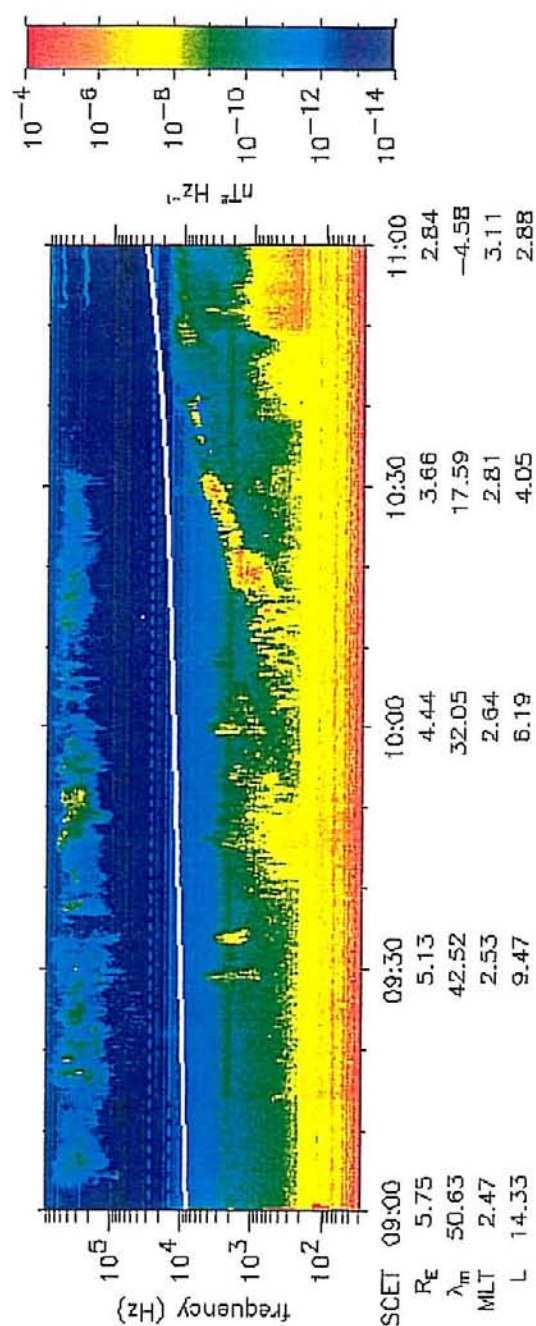


Figure 24. Electric power spectrum, magnetic power spectrum, wave normal angle, azimuthal angle of the wave normal vector, coherence, and polarization of auroral hiss electromagnetic burst from 09:33:25 UT to 09:34:12 UT on February 28, 1997.

Polar PWI HR HFWR Wave Normal Direction
 SCET: 97-02-28T09:33:25.804 to 97-02-28T09:34:12.254

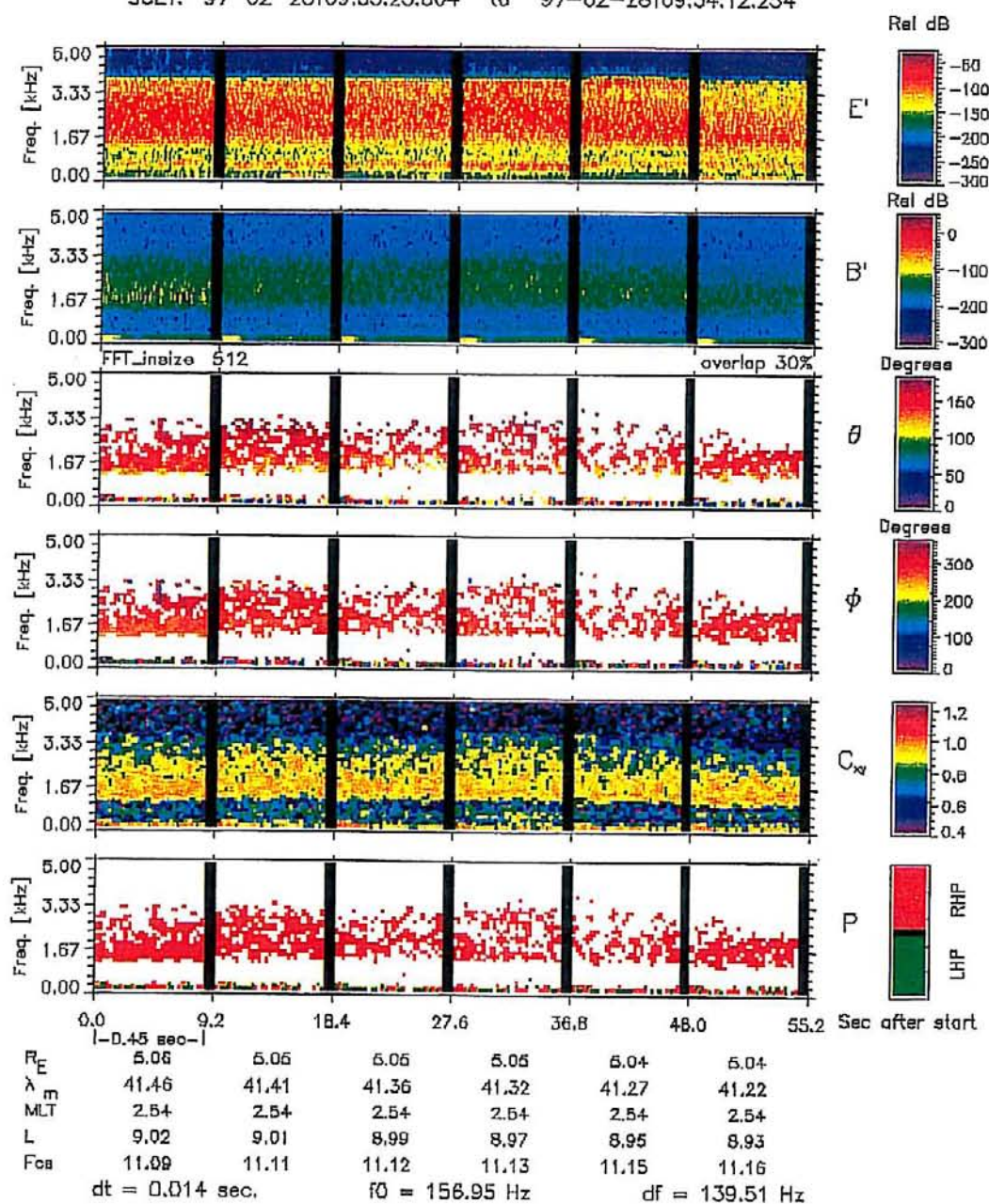
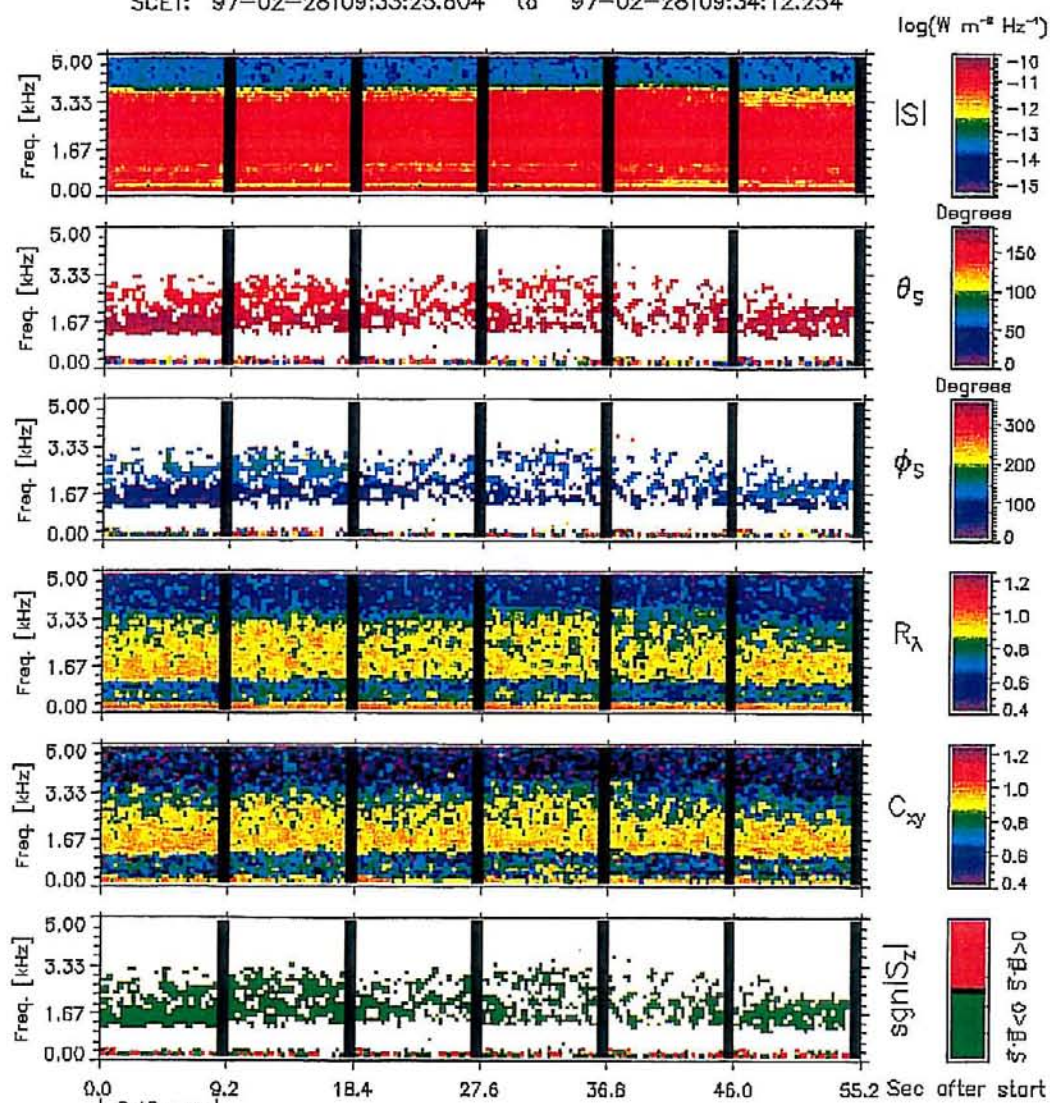


Figure 25. Poynting flux, polar angle of Poynting vector, azimuthal angle of Poynting vector, eigenvalue ratio of spectral matrix, coherence, and direction of S_z for auroral hiss electromagnetic burst from 09:33:25 UT to 09:34:12 UT on February 28, 1997.

Polar PWI HR HFWR Poynting Flux Direction

SCET: 97-02-28T09:33:25.804 to 97-02-28T09:34:12.254



	0.0	9.2	18.4	27.6	36.8	46.0	55.2
R_E	-0.48	5.06	5.06	5.06	5.04	5.04	
λ	41.46	41.41	41.36	41.32	41.27	41.22	
MLT	2.54	2.54	2.54	2.54	2.54	2.54	
L	9.02	9.01	8.99	8.97	8.95	8.93	
F_{obs}	11.09	11.11	11.12	11.13	11.15	11.16	
$dt = 0.014 \text{ sec.}$		$f_0 = 156.95 \text{ Hz}$		$df = 139.51 \text{ Hz}$			

Figure 26. Wave normal angle as a function of frequency for the auroral hiss observed from 09:33:34.2 UT to 09:33:34.65 UT on February 28, 1997.

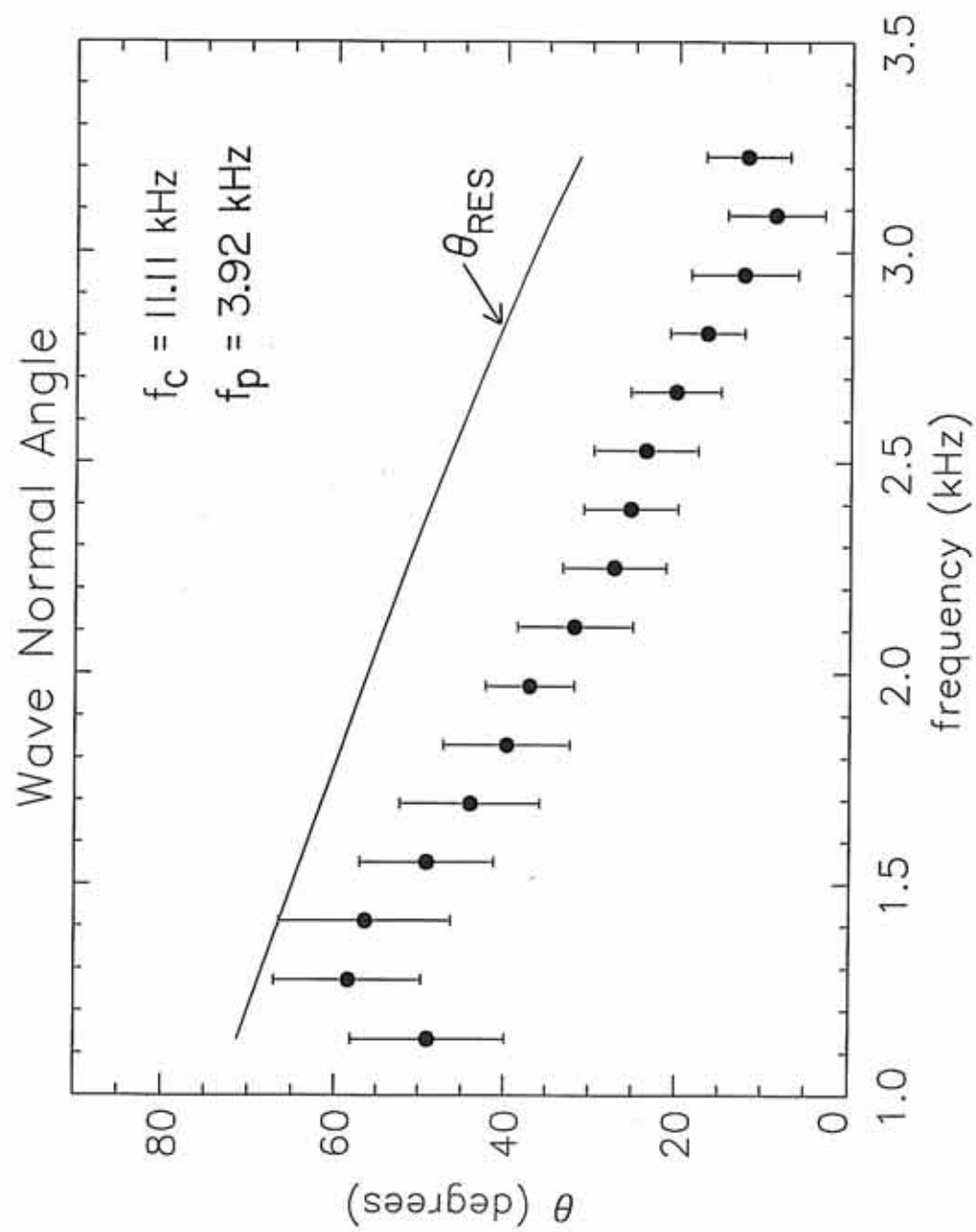


Figure 27. Poynting vector angle as a function of frequency for the auroral hiss observed from 09:33:34.2 UT to 09:33:34.65 UT on February 28, 1997.

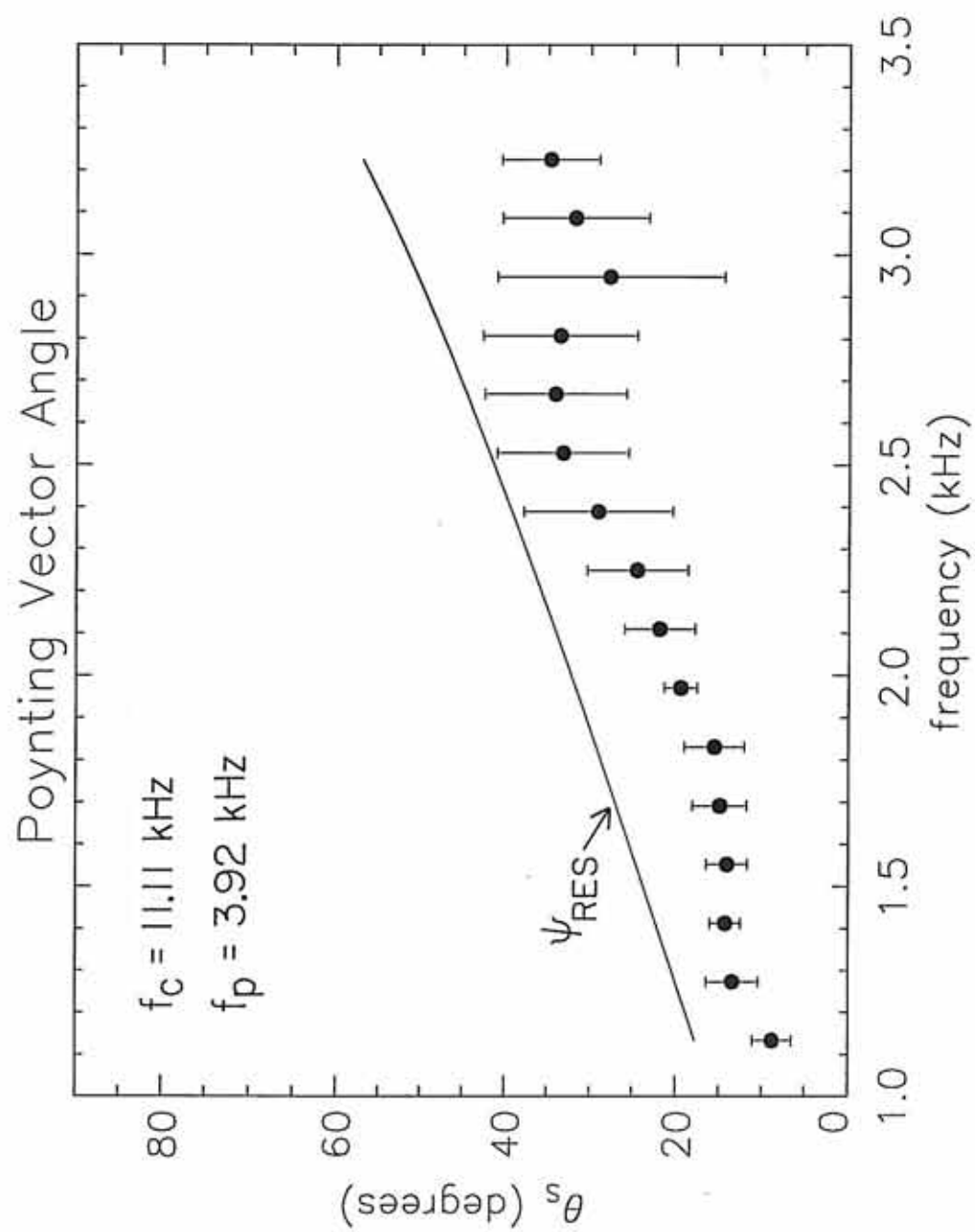
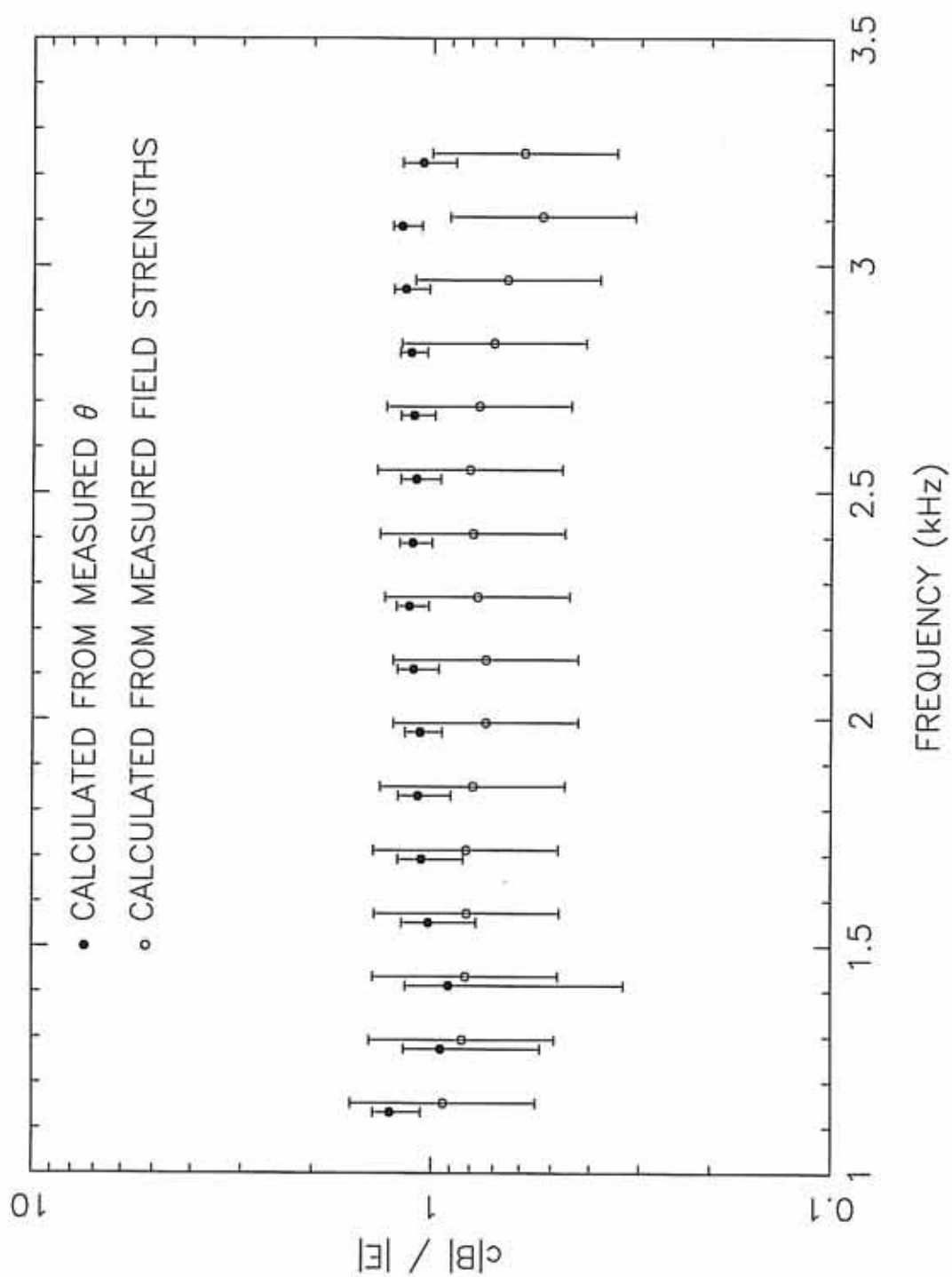


Figure 28. Ratio of magnetic field intensity to electric field intensity as a function of frequency for auroral hiss observed from 09:33:34.2 UT to 09:33:34.65 UT on February 28, 1997. $c|B|/|E|$ calculated using observed wave normal angles are plotted as filled circles. $c|B|/|E|$ calculated from measured electric and magnetic fields are plotted as open circles. The second set is plotted to slightly shifted frequencies from clarity



APPENDIX A: COORDINATE SYSTEMS

This appendix provides a brief description of the coordinate systems used throughout this paper. More detailed descriptions of the coordinate systems and methods for coordinate transformation can be found in Russell [1971], Hapgood [1992], and Mish [1994]. All the coordinate systems described here are right-handed, orthogonal coordinate systems.

Rotating-Payload (RP) Coordinates

The rotating-payload coordinate system is a spacecraft-centered system. The positive z-axis is parallel to the spacecraft spin axis. The positive x-axis is perpendicular to the z-axis and is aligned with the magnetometer boom (see Figure 3). The positive y-axis is perpendicular to the x- and z-axes and completes the right-handed system. This system rotates with the spacecraft since the axes are fixed with respect to the magnetometer boom.

UVZ Coordinates

The z-axis of the UVZ coordinate system is parallel to the spin axis of the spacecraft. The positive u-axis is perpendicular to the z-axis and is aligned along the E_u + electric antenna. The u-axis is oriented 45° counterclockwise from the positive x-axis of the RP coordinate system (see Figure 3). The positive v-axis is perpendicular to the u- and z-axes, and is aligned along the E_v + electric antenna. This coordinate system also rotates with the spacecraft.

Fixed-Payload (FP) Coordinates

The fixed-payload coordinate system is also a spacecraft-centered system. The positive z-axis is parallel to the spin axis of the spacecraft. The x-axis is perpendicular to the z-axis and is in the meridian plane containing the radial vector from the spacecraft to the Sun. The y-axis completes the right-handed system.

Geocentric Solar Ecliptic (GSE) Coordinates

The geocentric solar ecliptic coordinate system is centered on the Earth. The positive x-axis points from the Earth to the Sun. The positive y-axis is in the ecliptic plane, pointing toward dusk (opposing the Earth's orbital motion). The z-axis is parallel to the ecliptic pole.

Local Magnetic Field-Aligned (FAC) Coordinates

The local magnetic field-aligned coordinate system is a spacecraft-centered coordinate system. The positive z-axis is parallel to the local geomagnetic field, B_0 . The positive x-axis points outward and lies in the plane defined by the z-axis and the radial vector pointing from the Earth to the spacecraft. The positive y-axis completes the right-handed system. This coordinate system is illustrated in Figure 6.

APPENDIX B: CALIBRATION TABLES

Table 1. Search Coil Phase Shifts

Frequency (Hz)	ϕ_u (deg)	ϕ_v (deg)	ϕ_z (deg)	$\phi_u - \phi_v$ (deg)
10	-85	-85	-85	0
20	-91	-91	-91	0
30	-95	-95	-95	0
40	-98	-98	-98	0
50	-100	-100	-100	0
60	-102	-102	-102	0
70	-103	-103	-103	0
80	-105	-105	-105	0
90	-107	-106	-106	-1
100	-108	-108	-108	0
150	-117	-116	-116	-1
200	-124	-123	-123	-1
300	-134	-134	-134	0
311	-135	-135	-135	0
400	-141	-141	-141	0
500	-146	-146	-146	0
562	-148	-149	-148	1
600	-150	-150	-150	0
700	-152	-152	-151	0
800	-153	-154	-153	1
900	-155	-156	-155	1
1000	-156	-157	-156	1
1780	-159	-161	-159	2
2000	-158	-160	-158	2
3000	-160	-161	-158	1
3110	-160	-162	-158	2
4000	-166	-168	-164	2
5000	179	177	-177	2
5620	170	170	170	0
6000	161	161	161	0
7000	127	132	134	-5
8000	107	114	113	-7
9000	95	101	99	-6
10000	87	92	90	-5
11000	82	86	84	-4
12000	77	81	79	-4
13000	75	78	76	-3
14000	72	74	73	-2
15000	69	71	70	-2
17800	63	64	63	-1
20000	59	60	59	-1
25000	51	50	50	-1
30000	45	44	44	1
31100	44	43	43	1

Table 2. Electric Sensor Gains

Frequency (kHz)	A_u (dB)	G_u (V_{true}/V_{meas})	A_v (dB)	G_v (V_{true}/V_{meas})	A_z (dB)	G_z (V_{true}/V_{meas})
0.01	0.0	1.0000	0.0	1.0000	0.0	1.0000
0.1	0.1	0.9886	0.1	0.9886	0.1	0.9886
0.3	0.2	0.9772	0.2	0.9772	0.2	0.9772
1.0	-1.2	1.1482	-1.4	1.1749	-1.4	1.1749
2.2	-2.5	1.3335	-2.7	1.3646	-2.5	1.3335
4.8	-4.5	1.6788	-4.6	1.6982	-3.9	1.5668
10.0	-5.4	1.8621	-5.5	1.8836	-4.7	1.7179
15.0	-5.1	1.7989	-5.2	1.8197	-4.6	1.6982
22.0	-4.7	1.7179	-4.8	1.7378	-4.2	1.6218
33.0	-4.2	1.6218	-4.3	1.6406	-3.9	1.5668

Table 3. Electric Sensor Phase Shifts

Frequency (kHz)	ϕ_u (deg)	ϕ_v (deg)	ϕ_z (deg)	$\phi_u - \phi_v$ (deg)
0.01	0.0	0.2	0.1	-0.2
0.1	-0.1	-0.2	0.1	0.1
0.3	-5.4	-5.7	-4.9	0.3
1.0	-12.7	-13.6	-10.7	0.9
2.2	-16.6	-16.6	-11.7	0.0
4.8	-15.2	-15.2	-10.6	0.0
10.0	-6.2	-6.0	-3.4	-0.2
15.0	-2.3	-2.7	-0.5	0.4
22.0	-2.4	-2.5	-0.1	0.1
33.0	-5.4	-5.4	-0.5	0.0

APPENDIX C: VECTOR DIRECTION VERIFICATION AND
ERROR ANALYSIS TABLES

Table 4. Comparison of Wave Normal Angles Using GSFC Magsite Test Data

Drive Freq. (Hz)	Fourier Freq. (Hz)	θ (deg)	$\Delta\theta$ (deg)
200	209.263	-43.04°	-1.96
200	209.263	-47.85°	1.17
5000	4987.444	-46.93°	1.93
10000	10009.766	-43.17°	-1.83

Table 5. Geographic Position of Polar Magnetic Field Endpoint

Year	Time		Latitude (deg)	Longitude (deg)
	Day	hh:mm:ss		
1996	255	09:00:00	37.97	-95.72
1996	255	09:03:00	38.19	-96.51
1996	255	09:06:00	38.69	-97.24
1996	255	09:09:00	39.42	-97.93
1996	255	09:12:00	40.31	-98.59
1996	255	09:15:00	41.32	-99.21

Table 6. Cloud-to-Ground Lightning Observed by National Lightning Detection Network

Date	Time (UTC)	Lat	Long	Signal Strength	Mult
mm/dd/yy	hh:mm:ss	(deg)	(deg)	(kA)	
09/11/96	09:12:20	25.298	-81.540	60.8	1
09/11/96	09:12:20	24.392	-82.354	-16.0	2
09/11/96	09:12:24	31.966	-106.827	-34.2	4
09/11/96	09:12:27	24.439	-82.548	-23.9	1
09/11/96	09:12:27	24.465	-82.542	-31.9	3

Table 7. Analysis Results Using Computer-Generated Data With Random Noise

snr	θ (deg)	θ_s (deg)	R_λ	C_{xy}
∞	0.000	0.000	1.000	1.000
2000	0.681	0.394	0.999	0.999
100.03	3.15	1.53	0.981	0.982
51.16	4.616	2.881	0.967	0.969
20.16	7.863	5.311	0.919	0.929

Table 8. Test Results Using Computer-Generated Signals With Gain and Phase Adjustments

δE_{uo} (% of E_{uo})	δB_{uo} (% of B_{uo})	$\delta \phi_{EU}$ (deg)	$\delta \phi_{BU}$ (deg)	θ (deg)	ϕ (deg)	θ_s (deg)	ϕ_s (deg)
1.0	1.0	0.0	0.0	45.000	0.000	45.000	0.000
1.0	1.0	0.0	1.0	44.998	359.293	44.998	359.646
1.0	1.0	0.0	5.0	44.945	356.460	44.959	358.232
1.0	1.0	1.0	0.0	45.000	0.000	44.998	359.646
1.0	1.0	5.0	0.0	45.000	0.000	44.959	358.232
1.1	1.0	0.0	0.0	45.000	0.000	46.397	0.000
1.0	1.1	0.0	0.0	47.726	0.000	36.397	0.000

Table 9. Simulation of Calibration Effects at 1 kHz and 8 kHz

Frequency (kHz)	δE_{vo} (% of E_{vo})	$\delta \phi_{EV}$ (deg)	$\delta \phi_{Bu}$ (deg)	θ (deg)	ϕ (deg)	θ_s (deg)	ϕ_s (deg)
1.0	0.9773	0.9	-1.0	44.998	0.707	45.328	0.657
8.0	0.9885	-0.12	7.0	44.893	355.038	45.085	357.509

REFERENCES

- Acuña, M. H., K. W. Ogilvie, D. N. Baker, S. A. Curtis, D. H. Fairfield, and W. H. Mish, The Global Geospace Science Program and its investigations, *Space Sci. Rev.*, 71, 5, 1995.
- Allcock, G. McK., A study of audio-frequency radio phenomena known as "dawn chorus," *Australian J. Phys.*, 10, 286, 1957.
- Bendat, J. S., and A. G. Piersol, *Random Data: Analysis and Measurement Procedures*, 2nd Edition, John Wiley & Sons, New York, 1986.
- Born, M., and E. Wolf, *Principles of Optics: Electromagnetic Theory of Propagation, Interference and Diffraction of Light*, 4th Edition, Pergamon Press, Oxford, 1970.
- Brigham, E. O., *The Fast Fourier Transform and its Applications*, Prentice Hall, Englewood Cliffs, New Jersey, 1988.
- Buchalet, L. J., and F. Lefeuvre, One and two direction models for VLF electromagnetic waves observed on-board GEOS 1, *J. Geophys. Res.*, 86, 2377, 1981.
- Burgess, W. C., Lightning-induced coupling of the radiation belts to geomagnetically conjugate ionospheric regions, Ph.D. thesis, Stanford University, Stanford, CA, 1993.
- Burtis, W. J., and R. A. Helliwell, Banded chorus: A new type of VLF radiation observed in the magnetosphere by OGO-1 and OGO-3, *J. Geophys. Res.*, 74, 3002-3010, 1969.
- Burton, R. K., Critical electron pitch angle anisotropy necessary for chorus generation, *J. Geophys. Res.*, 81, 4779, 1976.
- Burton, R. K., and R. E. Holzer, The origin and propagation of chorus in the outer magnetosphere, *J. Geophys. Res.*, 79, 1014, 1974.

- Carpenter, D. L., and R. E. Orville, The excitation of active whistler mode signal paths in the magnetosphere by lightning: Two case studies, *J. Geophys. Res.*, **94**, 8886, 1989.
- Chan, K.-W., R. K. Burton, R. E. Holzer, and E. J. Smith, Measurement of the wave-normal vector of proton whistlers on Ogo 6, *J. Geophys. Res.*, **77**, 635, 1972.
- Chen, J., T. A. Fritz, R. B. Sheldon, H. E. Spence, W. N. Spjeldvik, J. F. Fennell, S. Livi, C. T. Russell, J. S. Pickett, and D. A. Gurnett, Cusp energetic particle events: Implications for a major acceleration region of the magnetosphere, *J. Geophys. Res.*, **103**, 69, 1998.
- Cornilleau-Wehrin, N., R. Gendrin, F. Lefeuvre, M. Parrot, R. Grard, D. Jones, A. Bahnsen, E. Ungstrup, and W. Gibbons, VLF electromagnetic waves observed onboard GEOS-1, *Space Sci. Rev.*, **22**, 371-382, 1978.
- Dunkel, N., and R. Helliwell, Whistler mode emissions in the OGO 1 satellite, *J. Geophys. Res.*, **74**, 6371-6385, 1969.
- Ellis, G. R., Low frequency radio emissions from aurorae, *J. Atmos. Terr. Phys.*, **10**, 302, 1957.
- Fainberg, J., L. G. Evans, and R. G. Stone, Radio tracking of solar energetic particles through interplanetary space, *Science*, **178**, 743, 1972.
- Farrell, W. M., D. A. Gurnett, P. M. Banks, R. I. Bush, and W. J. Raitt, An analysis of whistler-mode radiation from the Spacelab-2 electron beam, *J. Geophys. Res.*, **93**, 153, 1988.
- Farrell, W. M., D. A. Gurnett, and C. K. Goertz, Coherent Cerenkov radiation from the Spacelab-2 electron beam, *J. Geophys. Res.*, **94**, 443, 1989.
- Fowler, R. A., B. J. Kotick, and R. D. Elliott, Polarization analysis of natural and artificially induced geomagnetic micropulsations, *J. Geophys. Res.*, **72**, 2871, 1967.
- Golde, R. H., ed. *Lightning, Vol. 1, The Physics of Lightning*, Academic Press, London, 1977.
- Goldstein, B. E., and B. T. Tsurutani, Wave normal directions of chorus near the equatorial source region, *J. Geophys. Res.*, **89**, 2789, 1984.

- Goldstein, H. *Classical Mechanics*, 2nd Edition, Addison-Wesley Publishing Company, Reading, Massachusetts, 1980.
- Griffiths, D. J., *Introduction to Electrodynamics*, 2nd Edition, Prentice Hall, Englewood Cliffs, New Jersey, 1989.
- Gurnett, D. A., A satellite study of VLF hiss, *J. Geophys. Res.*, 71, 5599, 1966.
- Gurnett, D. A., The Earth as a radio source: Terrestrial kilometric radiation, *J. Geophys. Res.*, 79, 4227, 1974.
- Gurnett, D. A., and M. M. Baumbach, *Description and calibration of the IMP-J E. M. Fields Experiment*, The University of Iowa, Iowa City, Iowa, 1973.
- Gurnett, D. A., and L. A. Frank, VLF hiss and related plasma observations in the polar magnetosphere, *J. Geophys. Res.*, 77, 172, 1972.
- Gurnett, D. A., and L. A. Frank, Plasma waves in the polar cusp: Observations from Hawkeye 1, *J. Geophys. Res.*, 83, 1447, 1978.
- Gurnett, D. A., and U. S. Inan, Plasma wave observations with the Dynamics Explorer 1 spacecraft, *Rev. Geophys.*, 26, 285, 1988.
- Gurnett, D. A., S. R. Mosier, and R. R. Anderson, Color spectrograms of very-low-frequency Poynting flux data, *J. Geophys. Res.*, 76, 3022, 1971.
- Gurnett, D. A., and B. J. O'Brien, High-latitude geophysical studies with satellite Injun 3. Part 5, Very-low-frequency electromagnetic radiation, *J. Geophys. Res.*, 69, 65, 1964.
- Gurnett, D. A., A. M. Persoon, R. F. Randall, D. L. Odem, S. L. Remington, T. F. Averkamp, M. M. Debowe, G. B. Hospodarsky, R. L. Huff, D. L. Kirchner, M. A. Mitchell, B. T. Pham, J. R. Phillips, W. J. Schintler, P. Sheyko, and D. R. Tomash, The Polar Plasma Wave Instrument, *Space Sci. Rev.*, 71, 597, 1995.
- Gurnett, D. A., G. W. Pfeiffer, R. R. Anderson, S. R. Mosier, and D. P. Cauffman, Initial observations of VLF electric and magnetic fields with the Injun 5 Satellite, *J. Geophys. Res.*, 74, 4631, 1969.
- Gurnett, D. A., S. D. Shawhan, and R. R. Shaw, Auroral hiss, Z mode radiation, and auroral kilometric radiation in the polar magnetosphere: DE 1 observations, *J. Geophys. Res.*, 88, 329, 1983.

- Hapgood, M. A., Space physics coordinate transformations: a user guide, *Planet. Space Sci.*, 40, 711-717, 1992.
- Harvey, P., F. S. Mozer, D. Pankow, J. Wygant, N. C. Maynard, H. Singer, W. Sullivan, P. B. Anderson, R. Pfaff, T. Aggson, A. Pedersen, C.-G. Fälthammar, and P. Tanskannen, The Electric Field Instrument on the Polar Satellite, *Space Sci. Rev.*, 71, 583, 1995.
- Hayakawa, M., K. Hattori, S. Shimakura, M. Parrot, and F. Lefeuvre, Direction finding of chorus emissions in the outer magnetosphere and their generation and propagation, *Planet. Space Sci.*, 38, 135-143, 1990.
- Hayakawa, M., Y. Yamanaka, M. Parrot, and F. Lefeuvre, The wave normals of magnetospheric chorus emissions observed on board GEOS 2, *J. Geophys. Res.*, 89, 2811, 1984.
- Helliwell, R. A., *Whistlers and Related Ionospheric Phenomena*, Stanford University Press, Stanford, CA, 1965.
- Helliwell, R. A., Low-frequency waves in the magnetosphere, *Rev. Geophys.*, 7, 281, 1969.
- Hoffman, R. A., and T. Laaspere, Comparison of very-low-frequency auroral hiss with precipitating low-energy electrons by the use of simultaneous data from two OGO-4 experiments, *J. Geophys. Res.*, 77, 640, 1972.
- Hughes, A. R. W., and T. R. Kaiser, VLF radio emissions and the aurora, *The Radiating Atmosphere*, ed. by B. M. McCormac, Reidel, Dordrecht, 1971.
- Isenberg, P. A., H. C. Koons and J. F. Fennell, Simultaneous observations of energetic electrons and dawnside chorus in geosynchronous orbit, *J. Geophys. Res.*, 87, 1495, 1982.
- James, H. G., Whistler-mode hiss at low and medium frequencies in the dayside-cusp ionosphere, *J. Geophys. Res.*, 78, 4578, 1973.
- James, H. G., VLF saucers, *J. Geophys. Res.*, 81, 501, 1976.
- Jorgensen, T. S., Interpretation of auroral hiss measured on OGO 2 and at Byrd Station in terms of incoherent Cerenkov radiation, *J. Geophys. Res.*, 73, 1055, 1968.

- Kasahara, Y., Study on the ELF/VLF emissions in a multicomponent plasma observed by the Akebono satellite, Ph.D. Thesis, Faculty of Engineering, Kyoto University, 1995.
- Kasahara, Y., H. Kenmochi, and I. Kimura, Propagation characteristics of the ELF emissions observed by the satellite Akebono in the magnetic equatorial region, *Radio Sci.*, 29, 751, 1994.
- Kasahara, Y., A. Sawada, M. Yamamoto, I. Kimura, S. Kokubun, and K. Hayashi, Ion cyclotron emissions observed by the satellite Akebono in the vicinity of the magnetic equator, *Radio Sci.*, 27, 347, 1992.
- Kelley, M. C., D. J. Knudsen, and J. F. Vickrey, Poynting flux measurements on a satellite: A diagnostic tool for space research, *J. Geophys. Res.*, 96, 201, 1991.
- Kennel, C. F., and H. E. Petschek, Limit on stably trapped particle fluxes, *J. Geophys. Res.*, 71, 1, 1966.
- Kletzing, C. A., G. Berg, M. C. Kelley, F. Primdahl, and R. B. Torbert, The electrical and precipitation characteristics of morning sector Sun-aligned auroral arcs, *J. Geophys. Res.*, 101, 17,175, 1996.
- Kurth, W. S., M. M. Baumbach, and D. A. Gurnett, Direction-finding measurements of auroral kilometric radiation, *J. Geophys. Res.*, 80, 2764, 1975.
- Laaspere, T., and R. A. Hoffman, New results on the correlation between low-energy electrons and auroral hiss, *J. Geophys. Res.*, 81, 524, 1976.
- Laaspere, T., and W. C. Johnson, Additional results from an OGO-6 experiment concerning ionospheric electric and electromagnetic fields in the range 20 Hz to 540 kHz, *J. Geophys. Res.*, 78, 2926, 1973.
- Laaspere, T., W. C. Johnson, and L. C. Sembrebon, Observation of auroral hiss, LHR noise, and other phenomena in the frequency range 20 Hz - 540 kHz, *J. Geophys. Res.*, 76, 4477, 1971.
- Lauben, D. S., U. S. Inan, T. F. Bell, D. L. Kirchner, G. B. Hospodarsky, and J. S. Pickett, VLF chorus emissions observed by Polar during the January 10, 1997 magnetic cloud, *Geophys. Res. Lett.*, submitted, 1998.

- Lefeuvre, F., and C. Delannoy, Analysis of a random electromagnetic wave field by a maximum entropy method, *Ann. Telecomm.*, 34, 204, 1979.
- Lefeuvre, F., M. Parrot, and C. Delannoy, Wave distribution functions estimation of VLF electromagnetic waves observed on board GEOS 1, *J. Geophys. Res.*, 86, 2359, 1981.
- Lin, C. S., J. L. Burch, S. D. Shawhan, and D. A. Gurnett, Correlation of auroral hiss and upward electron beams near the polar cusp, *J. Geophys. Res.*, 89, 925, 1984.
- Maggs, J. E., Coherent generation of VLF hiss, *J. Geophys. Res.*, 81, 1707, 1976.
- Maggs, J. E., Electrostatic noise generated by the auroral electron beam, *J. Geophys. Res.*, 83, 3173, 1978.
- McEwen, D. J., and R. E. Barrington, Some characteristics of the lower hybrid resonance noise bands observed by Alouette 1 satellite, *Can. J. Phys.*, 45, 13, 1967.
- McPherron, R. L., C. T. Russell, and P. J. Coleman, Jr., Fluctuating magnetic fields in the magnetosphere, *Space Sci. Rev.*, 13, 411, 1972.
- Means, J. D., Use of the three-dimensional covariance matrix in analyzing the polarization properties of plane waves, *J. Geophys. Res.*, 77, 5551, 1972.
- Mish, W. H., and C. Raymond, ISTP Coordinate Systems, Appendix H, *ISTP Key Parameter Generation Software Standards and Conventions Document*, NASA/Goddard Space Flight Center, March 1994.
- Morgan, D. D., Landau damping of auroral hiss, Ph.D. Thesis, Department of Physics and Astronomy, The University of Iowa, Iowa City, Iowa, December 1992.
- Morgan, D. D., D. A. Gurnett, J. D. Menietti, J. D. Winningham, and J. L. Burch, Landau damping of auroral hiss, *J. Geophys. Res.*, 99, 2471, 1994.
- Mosier, S. R., and D. A. Gurnett, VLF measurements of the Poynting flux along the geomagnetic field with the Injun 5 satellite, *J. Geophys. Res.*, 74, 5675, 1969.
- Mosier, S. R., and D. A. Gurnett, Theory of the Injun 5 very-low-frequency Poynting flux measurements, *J. Geophys. Res.*, 76, 872, 1971.

- Mosier, S. R., and D. A. Gurnett, Observed correlation between auroral and VLF emissions, *J. Geophys. Res.*, 77, 1137, 1972.
- Muto, H., and M. Hayakawa, Ray tracing study of the propagation in the magnetosphere of whistler-mode VLF emissions with frequency above one half the gyrofrequency, *Planet. Space Sci.*, 35, 1397-1404, 1987.
- Muto, H., M. Hayakawa, M. Parrot, and F. Lefeuvre, Direction finding of half-gyrofrequency VLF emissions in the off-equatorial region of the magnetosphere and their generation and propagation, *J. Geophys. Res.*, 92, 7538, 1987.
- Nagano, I., S. Yagitani, H. Kojima, and H. Matsumoto, Analysis of wave normal and Poynting vectors of the chorus emissions observed by Geotail, *J. Geomag. Geoelectr.*, 48, 299-307, 1996.
- Ondoh, T., Broad-band auroral VLF hiss and inverted-V electron precipitation in the polar magnetosphere, *J. Atmos. Terr. Phys.*, 52, 387, 1990.
- Parks, G. K., *Physics of Space Plasmas: An Introduction*, Addison-Wesley Publishing Co., Redwood City, California, 1991.
- Persoon, A. M., D. A. Gurnett, W. K. Peterson, J. H. Waite, Jr., J. L. Burch, and J. L. Green, Electron density depletions in the nightside auroral zone, *J. Geophys. Res.*, 93, 1871, 1988.
- Persoon, A. M., D. A. Gurnett, and S. D. Shawhan, Polar cap electron densities from DE 1 plasma wave observations, *J. Geophys. Res.*, 88, 10,123, 1983.
- Priestley, M. B., *Spectral Analysis and Time Series*, Academic Press, Harcourt Brace Jovanovich, Publishers, London, 1981.
- Rankin, D., and R. Kurtz, Statistical study of micropulsation polarizations, *J. Geophys. Res.*, 75, 5444, 1970.
- Russell, Christopher T., Geophysical Coordinate Transformations, *Cosmic Electrodynamics*, 2, D. Reidel Publishing Co., Dordrecht, Holland, 184, 1971.
- Russell, C. T., R. C. Snare, J. D. Means, D. Pierce, D. Dearborn, M. Larson, G. Barr, and C. Le, The GGS/Polar Magnetic Field Investigation, *Space Sci. Rev.*, 71, 563-582, 1995.

- Sakamoto, K., Y. Kasahara, and I. Kimura, K-vector determination of whistler mode signals by using amplitude data obtained by a spacecraft borne instrument, *IEEE Trans. Geosci. and Remote Sensing*, 33, 528, 1995.
- Samson, J. C., Matrix and Stokes vector representations of detectors for polarized waveforms: Theory, with some applications to teleseismic waves, *Geophys. J. R. Astr. Soc.*, 51, 583, 1977.
- Samson, J. C., and J. V. Olson, Some comments on the descriptions of the polarization states of waves, *Geophys. J. R. Astr. Soc.*, 61, 115, 1980.
- Sazhin, S. S., K. Bullough, and M. Hayakawa, Auroral hiss: A review, *Planet. Space Sci.*, 41, 153, 1993.
- Sentman, D. D., A search for periodic structure in solar 2 cm microwave radiation, Master's thesis, Department of Physics and Astronomy, The University of Iowa, 1973.
- Sentman, D. D., Basic elements of power spectral analysis, University of Iowa Research Report 74-5, 1974.
- Smith, E. J., and B. T. Tsurutani, Magnetosheath lion roars, *J. Geophys. Res.*, 81, 2261, 1976.
- Smith, R. L., VLF observations of auroral beams as sources of a class of emission, *Nature*, 224, 351, 1969.
- Smith, R. L., and J. J. Angerami, Magnetospheric properties deduced from OGO 1 observations of ducted and nonducted whistlers, *J. Geophys. Res.*, 73, 1, 1968.
- Sonnerup, B. U. Ö., and L. J. Cahill, Jr., Magnetopause structure and attitude from Explorer 12 observations, *J. Geophys. Res.*, 72, 171, 1967.
- Sonwalker, V. S., T. F. Bell, R. A. Helliwell, and U. S. Inan, Direct multiple path magnetospheric propagation: A fundamental property of nonducted VLF waves, *J. Geophys. Res.*, 89, 2823, 1984.
- Sonwalker, V. S., and U. S. Inan, Measurements of Siple transmitter signals on the DE 1 satellite: Wave normal direction and antenna effective length, *J. Geophys. Res.*, 91, 154, 1986.

- Sonwalker, V. S., and U. S. Inan, Wave normal direction and spectral properties of whistler-mode hiss observed by the DE 1 satellite, *J. Geophys. Res.*, 93, 7493, 1988.
- Stix, T. H., *The Theory of Plasma Waves*, McGraw-Hill, New York, 1962.
- Stix, T. H., *Waves in Plasmas*, American Institute of Physics, New York, 1993.
- Storey, L. R. O., An investigation of whistling atmospherics, *Phil. Trans. Roy. Soc. London, Ser. A*, 246, 113, 1953.
- Storey, L. R. O., Electric field experiments: Alternating fields, in The ESRO Geostationary Magnetospheric Satellite, 267, European Space Research Organization, Neuilly-sur-Seine, Report No. SP-60, 1971.
- Storey, L. R. O., and F. Lefeuvre, Theory for the interpretation of measurements of the six components of a random electromagnetic wave field in space, *Space Research, XIV*, 381, eds. M. J. Rycroft, & R. D. Reasenberg, Akademie-Verlag, Berlin, 1974.
- Storey, L. R. O., and F. Lefeuvre, The analysis of 6-component measurements of a random electromagnetic wave field in a magnetoplasma - I. The direct problem, *Geophys. J. R. Astr. Soc.*, 56, 255, 1979.
- Storey, L. R. O., and F. Lefeuvre, The analysis of 6-component measurements of a random electromagnetic wave field in a magnetoplasma - II. The integration kernels, *Geophys. J. R. Astr. Soc.*, 62, 173, 1980.
- Storey, L. R. O., F. Lefeuvre, M. Parrot, L. Cairo, and R. R. Anderson, Initial survey of the wave distribution functions for plasmaspheric hiss observed by ISEE 1, *J. Geophys. Res.*, 96, 19,469, 1991.
- Swanson, E. R., Omega, *Proc. IEEE*, 71, 1140, 1983.
- Taylor, W. W. L., Generation and propagation of electromagnetic waves in the magnetosphere, Ph.D. Thesis, Department of Physics and Astronomy, The University of Iowa, Iowa City, Iowa, 1973.
- Taylor, W. W. L., and S. D. Shawhan, A test of incoherent Cerenkov radiation for VLF hiss and other magnetospheric emissions, *J. Geophys. Res.*, 79, 105, 1974.

- Thorne, R. M., E. J. Smith, R. K. Burton, and R. E. Holzer, Plasmaspheric hiss, *J. Geophys. Res.*, 78, 1581, 1973.
- Tsurutani, B. T., G. S. Lakhina, C. M. Ho, J. K. Arballo, C. Calvan, J. S. Pickett, D. A. Gurnett, W. K. Peterson, and R. M. Thorne, Broadband plasma waves observed in the polar cap boundary layer (PCBL): POLAR, *J. Geophys. Res.*, in press, 1998.
- Tsurutani, B. T., and E. J. Smith, Two types of magnetospheric ELF chorus and their substorm dependences, *J. Geophys. Res.*, 82, 5112-5128, 1977.
- Yamaguchi, M., K. Hattori, N. Iwama, and M. Hayakawa, A new direction finding method of magnetospheric VLF/ELF radio waves using regularization and generalized cross validation, in *Proceedings of the 1992 International Symposium on Antennas and Propagation (ISAP)*, vol. 4, 1165, IEICE, Japan, 1992.
- Yoshino, T., T. Ozaki, and H. eFukinishi, Occurrence distribution of VLF hiss and saucer emissions over the southern polar region, *J. Geophys. Res.*, 86, 864, 1981.